Hybrids of biomacromolecules and modern two-dimensional materials

Delač Marion, Ida

Doctoral thesis / Disertacija

2017

Permanent link / Trajna poveznica: https://urn.nsk.hr/urn:nbn:hr:217:638968

Download date / Datum preuzimanja: **2024-11-08**

Repository / Repozitorij:

Repository of the Faculty of Science - University of Zagreb

University of Zagreb

FACULTY OF SCIENCE
DEPARTMENT OF PHYSICS

Ida Delač Marion

Hybrids of biomacromolecules and modern two-dimensional materials

DOCTORAL THESIS

Zagreb, 2017.

University of Zagreb

FACULTY OF SCIENCE
DEPARTMENT OF PHYSICS

Ida Delač Marion

Hybrids of biomacromolecules and modern two-dimensional materials

DOCTORAL THESIS

Supervisors:
dr. sc. Marko Kralj
dr. sc. Tomislav Vuletić

Zagreb, 2017.

Sveučilište u Zagrebu

PRIRODOSLOVNO - MATEMATIČKI FAKULTET
FIZIČKI ODSJEK

Ida Delač Marion

Hibridi biomakromolekula i modernih dvodimenzionalnih materijala

DOKTORSKI RAD

Mentori:
dr. sc. Marko Kralj
dr. sc. Tomislav Vuletić

Zagreb, 2017.

Acknowledgements

First and foremost, I want to thank my mentors Marko Kralj & Tomislav Vuletić, who helped me walk the line between surface physics and biophysics, and tried to teach me how to focus on what's important.

I am also grateful to all of my coworkers from Institute of Physics that helped me in one way or another, especially everyone involved in nano&bio research, and mostly Iva, Marin, Davor and Nataša.

Furthermore, I want to thank all of my scientific collaborators outside of Institute of Physics, and especially Maja Buljan, Predrag Lazić and Blanca Biel.

Big thank you goes to all of my friends and all climbing companions, especially Damir, Darko and Tomislav who always listen and encourage me to keep going.

Finally, I am grateful to my whole family for all the encouragement and support through the years. And special thanks goes to Sanjin, for being the husband that I need, but not always deserve.

Summary

Keywords: 2D materials, graphene, MoS_2 monolayer, nanocluster array, atomic defects, DNA-based constructs, nano-bio hybrid materials, bio-optoelectronics

Compared to bulk material, interfaces exhibit additional rich physical phenomena. Functionalized surfaces represent interfaces which are of great importance not only in fundamental surface and materials science but also for applications, which is additionally emphasized by the fact that most of the microelectronic devices used today are based on planar designs. One implementation of functionalized surfaces are hybrid materials. These bridge the gap between living matter and technology and may consist of a solid state substrate and a layer of biomacromolecules. This work is focused on two-dimensional (2D) materials studied as substrates for the growth of a biomacromolecular layer, leading to hybrid structures. In the studied hybrid systems both components have similar symmetry or distribution on a lateral scale, leading to a possible template effect of the substrate: hexagonal symmetry of the nanotemplated 2D material in combination with the DNA origami tetrahedral structure. Two different 2D material templates were investigated: either functionalized graphene or molybdenum disulphide, both on Ir(111) crystalline support. Graphene was grown directly on Ir(111) and subsequently functionalized with AuIr nanoclusters self-assembled on a graphene moiré pattern into a hexagonal array. MoS_2 was grown on SiO_2 substrate and then transferred to Ir(111). Both 2D substrates were extensively characterized down to the nanoscale, and their stability under ambient and in liquid conditions was confirmed. Taking into account the chemical specificity of the template materials (e.g. gold nanoclusters on graphene or sulphur vacancies in MoS_2), tetrahedron shaped DNA origami constructs with thiol groups in three of the vertexes were chosen as biomacromolecules of interest. Tetrahedra adsorption was calibrated on flat gold surfaces, and then applied to both 2D supports, thus producing two different hybrid systems, which were subsequently characterized. Such hybrid systems and their measured properties give promise for future applications in bio-optoelectronics as building blocks in e.g. sensor chips or DNA microarrays.

Contents

List of commonly used acronyms

2D - two dimensional

AFM - atomic force microscope

bp - base pairs (of a DNA strand)

CB - conduction band

CVD - chemical vapor deposition

DFT - density functional theory

DNA - deoxyribonucleic acid

LDOS - local density of states

LEED - low energy electron diffraction

MD - molecular dynamics

ML - monolayer

nt - nucleotide (of a DNA strand)

PDMS - polydimethylsiloxane

PL - photoluminescence

QCM-D - quartz crystal microbalance with dissipation monitoring

QY - quantum yield

RT - room temperature

SEM - scanning electron microscope

SPM - scanning probe microscopies (AFM&STM)

STM - scanning tunneling microscope

STS - scanning tunneling spectroscopy

TMD - transition metal dichalcogenide

TPG - temperature-programed growth

TSG - template stripped gold

UHV - ultra-high vacuum

VB - valence band

CHAPTER 1

Introduction

Since the beginning of microelectronics and integrated circuits, surfaces and interfaces played an essential role in a design and development of new devices. Back in 1959 in his visionary lecture *There's plenty of room at the bottom* [1] R. P. Feynman drew attention to yet unexplored area of miniaturization, and thus started revolution in the field. He spoke of fabrication of nanomachines, reduction of the size of computer components, storage of large amounts of data on a small surface (*Encyclopaedia Britannica* on the head of a pin), manipulation of single atoms and synthesis of new materials. He foretold emergence of a new direction in the scientific research, and thus gained the unofficial title of the "Father of Nanotechnology".

Reading his lecture today, one can see that many of the concepts predicted came to pass (like miniaturization of computers, storage of huge amount of data in a small space, manipulation of single atoms [2] and synthesis of new materials), yet some are still not within our reach. As the technology is advancing, more and more elements are squeezed on the same area, in accordance with the Moore's Law (that is, number of transistors per integrated circuit is doubled every two years [3]).

Yet today's silicon based technology is reaching its possible physical limits and the search for the replacement is a hot topic [4, 5]. In addition to materials themselves, approach also needs to change: former *top-down* approach is more and more often replaced with approach which is closer to the scientific way of thinking, that is, *bottom-up* approach. It starts by considering the structure and properties of the material on an atomic level in order to get to desired macroscopic properties. Although there are some propositions about data storage and processing in three dimensions, all of the currently developed technology is still two dimensional. Furthermore, even though different types of semiconductor devices with individual 1D structures already exist, their practical application is hindered by the fact that they come with different dimensions (diameters and lengths) and consequently different electronic properties

caused by the manufacturing processes. These problems can be resolved by use of 2D materials, as their geometry is already compatible with existing device designs and processing approaches from semiconductor industry and they are easily reproducibly produced with same electronic and optical properties.

In 2004 [6] graphene entered the scene and one of the first reasons of the graphene's popularity was its very existence. Namely, 80 years ago Landau and Peierls proved using standard harmonic approximation that the thermal fluctuations in 2D are so strong that they destroy any long-range order on the non-zero temperature [7, 8]. Mermin and Wagner expanded this by proving that long-range magnetic order cannot exist in 1 and 2D, later expanding their proof to crystalline order in 2D [9, 10]. These theories are supported by numerous experiments which observed rapid increase in instability with reduction of thickness in thin films. Films with the thickness less then few tenths of atomic layers usually become unstable and segregate in islands. Although this theory proves that existence of perfect crystals in 2D is impossible, it does not forbid existence of almost perfect 2D crystals in 3D space. Detailed analysis of a problem of 2D crystal beyond harmonic approximation revealed existence of two opposed kinds of phonons that can stabilize monolayer membranes by folding in a third dimension. Such intrinsic microscopic roughening with surface normal variation of several degrees and out of plane deformations up to 1 nm have indeed been observed experimentally in a freestanding graphene sheets [11].

Although graphene was the first, and by far most researched two dimensional material, it is not the only one. Starting with graphene, many more 2D materials emerged, of which most prominent examples include molybdenum disulphide, tungsten disulphide (as representatives of transition-metal dihalcogenides -TMDs) or hexagonal boron nitride (hBN) [12]. These 2D crystalline materials are considered as promising building blocks for next-generation wearable, flexible, stretchable, and transparent electronics due to their superior electrical, optical, and mechanical properties. Despite many marvelous properties, there are still some issues that have yet to be addressed in order to have these materials implemented in commercial electronic devices. A major one is relatively hard control of the charge carrier concentration, i.e. the level of doping. Besides active electric field control, reliable doping methods like ion implantation can cause fatal crystal damage in 2D materials, so there is active research and development of a safer methods underway, that will allow the successful integration of 2D materials in new generation of electronic and optoelectronic devices [13].
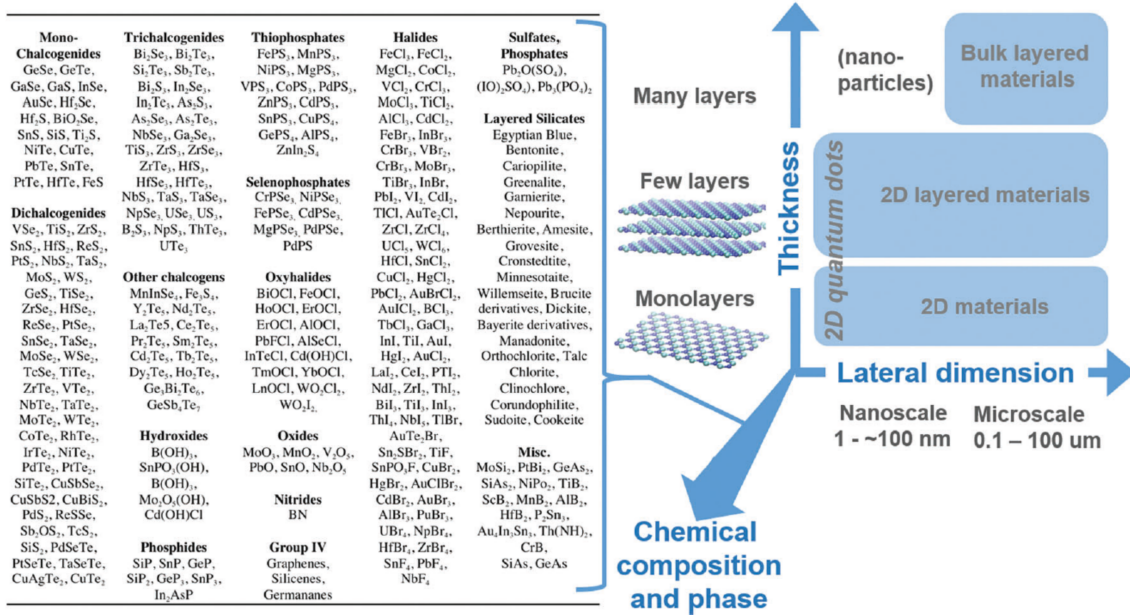
1.1 2D materials

Figure 1.1: Overview of the layered materials with the potential for production of 2D material. Adopted from [14].

Generally, all of the stable 2D materials known today also exist as a layered bulk material with strong binding in the layers and relatively weak interlayer van der Waals (vdW) interactions which allow exfoliation of individual, atomically thin layers. Simple overview of the layered materials is shown in figure 1.1, but it should be noted that only some of those can exist as stable 2D material [14]. For those that do, it is interesting to note that they usually exhibit many interesting layer-dependent properties, which can differ greatly from their properties in the bulk. Examples of those are TMDs, transition metal oxides including titania- and perovskite-based oxides and graphene analogues such as hexagonal boron nitride (hBN). Although first applied, exfoliation from the bulk is just one of the many methods for obtaining 2D materials. Method of interest for us was epitaxial growth (via chemical vapour deposition - CVD), which can produce relatively large monolayers on a variety of substrates which can further influence properties of a grown 2D material [15].

After the initial isolation of the graphene and extensive research of its fascinating properties (like extraordinary high intrinsic mobility, high mechanical strength, remarkable light transmittance, linear dispersion near the K point in the electronic band structure, high thermal conductivity and surprising molecular barrier properties) that gave promise for the broad possible applications (like transparent conductive electrodes, energy storage and supercapacitor materials), limits for its use became

apparent. Namely, because pristine graphene doesn't have a band gap, field effect transistors (FETs) made from graphene can't be effectively switched off and have low on/off switching ratios. Although band gaps can be engineered in graphene using different techniques like nanostructuring or chemical functionalization these methods reduce mobility and significantly complicate production [16]. During further research of the possible 2D materials, TMDs emerged as a great candidates to supplement graphene. They exhibit a broad range of electronic, optical, mechanical, chemical and thermal properties that are both complementary and yet often very different from graphene. In particular, several of them have band gaps around 1–2 eV, and have already proven themselves as very good building blocks for new FET and optoelectronic devices [17, 18].

Research of 2D materials was established on the foundations of the previous research of bulk materials which they constitute. Namely, graphite has been known as a mineral for over 500 years, and already used in the middle ages in a similar way as in pencils today. Later on, it was used as a dry lubricant, along with the compounds like hexagonal boron nitride and molybdenum disulphide. Accompanying industrial uses, extensive research of TMDs was conducted [19, 20] and gathered insights helped to fuel recent research as well.

1.1.1 Graphene

Graphene, a single layer of carbon atoms arranged in a honeycomb lattice, in addition to being basic building unit of a graphite is also a building block of carbon nanotubes (1D systems) and fullerenes (0D systems), which were all well known even before the graphene itself was introduced. When it was discovered, it was unique in a sense that it was completely 2D system, which was deemed impossible before that. Crystal lattice of the graphene is honeycomb lattice, which is not Bravais lattice, but it can be described as hexagonal lattice with two atoms in a base. Lattice is formed by sp^2 hybridization of s, p_x and p_y atomic orbitals on each carbon atom which results in formation of strong covalent sp^2 bonds (resulting in σ band), with distance between atoms being around 1.42 Å, and hexagonal lattice constant of 2.45 Å [21], as shown in figure 1.2a, with the corresponding first Brillouin zone shown in 1.2b. The remaining p_z orbital on each carbon overlaps with its three neighbours and they form valence (π) and conduction (π^*) bands. Schematic representation of the electronic band structure calculated in tight binding approximation with taking into account only nearest neighbours (1NN TBA) is shown in figure 1.3. Even such simplification already provides valuable insight into graphene's electronic

structure. Namely, graphene exhibits specific electron dispersion that is (for a free-standing undoped graphene) linear in the vicinity of Fermi energy, with the π and π^* bands touching only in a six K and K' points of the Brillouin zone, thus making graphene a semi-metal or a zero gap semiconductor. Consequently, electron transport in graphene can be described by Dirac's (relativistic) equation with the resulting quasiparticles that behave as relativistic particles with zero rest mass and have an effective 'speed of light' i.e. Fermi velocity of $\approx 10^6$ m/s [22]. Thus, K and K' points are often called Dirac points, while the electronic states around Fermi-level are accordingly called Dirac cones.
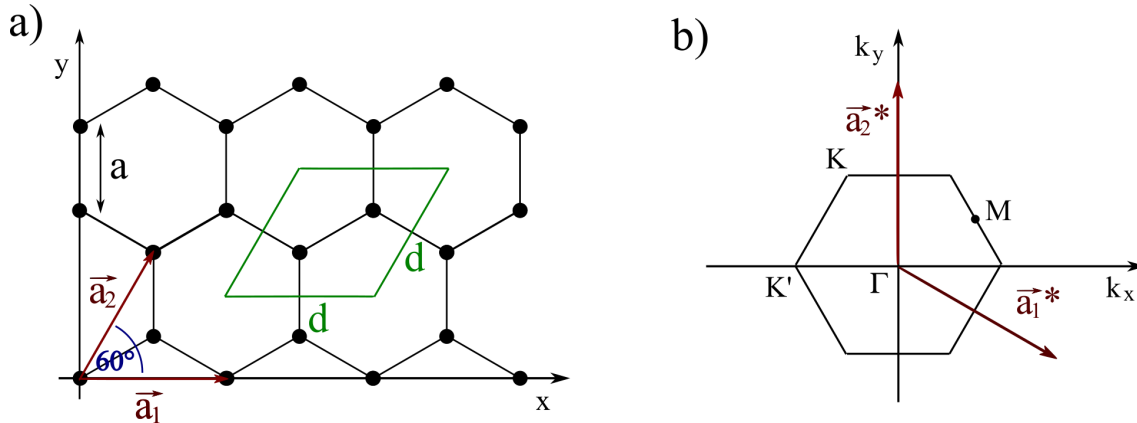

Figure 1.2: a) Schematic representation of graphene's crystal lattice, with a = 1.42 Å and d = 2.45 Å. b) First Brillouin zone of graphene with denoted high symmetry points.

Without out-of-plane chemical bonding in graphene, out-of-plane interactions are extremely weak resulting in out-of-plane electrical and thermal conductivities that are more than 10^3 times lower than those of their in-plane analogues [23]. Meanwhile, in-plane structure also results in many fascinating electronic and mechanical properties. Charge carriers in graphene exhibit zero effective mass and are being able to travel distances of microns at room temperature without being scattered [21], resulting in a ballistic charge transport on the micrometer-scale at room temperature. This is consequence of a high quality 2D crystal lattice with unusually low density of defects which leads to mobility of 170 000 cm^2/Vs at 5 K, and around 120 000 cm^2/Vs at 240 K [24]. In addition to such high mobility values, they are also very weakly dependent of temperature. Other interesting electronic properties include quantum Hall effect at room temperature and ambipolarity [6].

Moreover, graphene exhibits extreme strength, withstanding ≈ 40 N/m before breaking [25]. Its Young modulus is ≈ 1.0 TPa and it can be elastically stretched up to 20%, what is more than any other known crystal [25]. Its measured strength
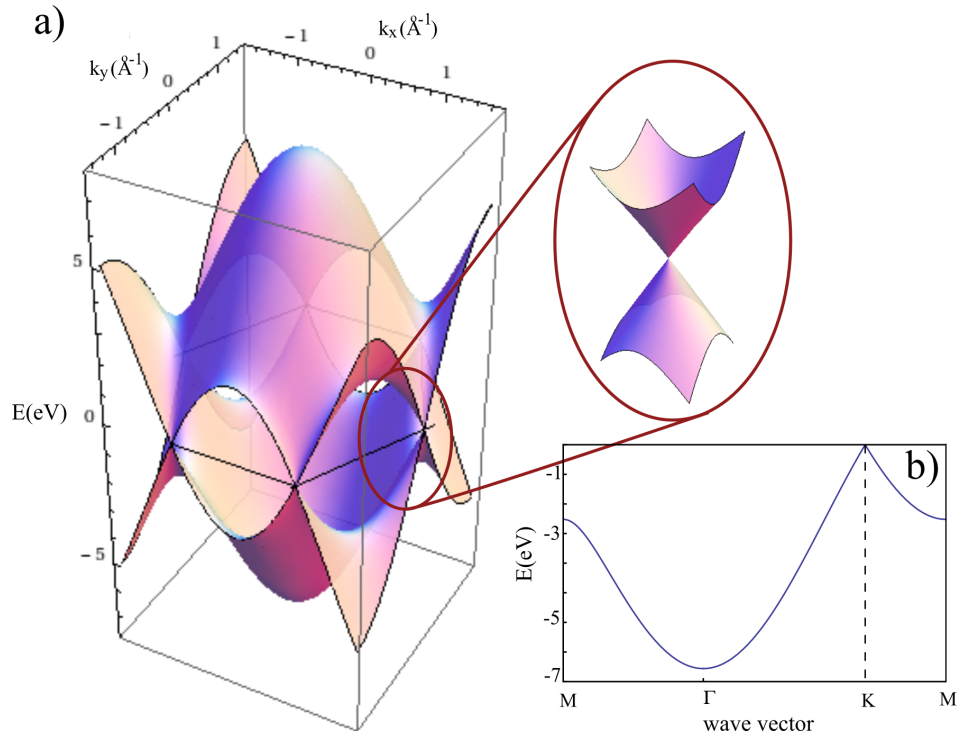
Figure 1.3: a) Schematic representation of electronic band structure of graphene in 1NN TBA. Highlighted is a region around K point. b) Cross-section of a conduction band in M-Γ-K-M direction.

is of the order of E/8, where E is the Young's modulus, which is close to the theoretically-predicted value of the strength of a defect-free material [26]. However, its behaviour at high-strains depends slightly upon the crystallographic direction in which it is deformed [27]. It also holds record in thermal conductance of ≈ 5000 $Wm^{-1}K^{-1}$ and is impermeable to many gases, but readily accepts various adsorbates, additionally exhibiting excellent electron transfer promoting ability for some enzymes and excellent catalytic behavior toward small biomolecules such as H_2O_2 or NADH, which makes it rather attractive for enzyme-based biosensors [28]. The single molecule sensitivity toward molecules like NO_2 and NH_3 also opens possibility for chemical sensing, however, the current problem is a lack of selectivity, which makes use of pristine graphene in chemical sensors rather impractical. Even though, it opens the possibility of chemical modification in a form of analyte-specific lock-and-key type binding sites, which could provide selective sensitivity to a large variety of chemical species and possibly enable detection of biological agents as well. Other potential applications relying on graphene's extraordinary properties include high-speed and radio frequency logic devices, transparent electrodes for displays and solar cells, energy storage (in supercapacitors, batteries or fuel cells and thermally and electrically conductive reinforced nanocomposites [28]).

In order for the practical application viable and reproducible production methods with large throughput should be established. First graphene samples were prepared with the so called scotch-tape technique [25] that consists of repeated peeling with adhesive tape (i.e. mechanical exfoliation) of highly oriented pyrolytic graphite which produces a mix of monolayer, bilayer and few-layered graphene flakes with varying lateral dimensions of up to the few tens of micrometers. Success of this method is largely due to the fact that monolayer graphene becomes visible under optical microscope on a SiO_2/Si surface if SiO_2 layer is precisely 300 nm thick. This method provided high-quality samples suitable for scientific research and proof-of-concept devices but is completely unusable for any kind of applications and there is also high possibility of contamination with glue. Alternative ways that were developed with consideration of potential applications can be divided in three categories: chemical route with exfoliation and stabilization individual sheets in solution which is another *top-down* approach, and *bottom-up* methods that include growth of graphene directly from organic precursors, and attempts to catalyze growth *in situ* on a substrate [16]. Catalyzed growth on a different substrates include chemical vapour deposition (CVD) and temperature programmed growth (TPG) on different metallic substrates (like cobalt, copper, iridium, tungsten, nickel, palladium, platinum, ruthenium [29, 30, 31, 32, 33, 34, 35]) or epitaxial growth on silicon carbide by heating it up to 1300°C in Ar atmosphere which results in sublimation of carbon atoms and reorganization of carbon rich surface into graphene [36]. Techniques used in this work are CVD and TPG [37], with protocols described in subsection 2.1.2. which result in a monolayer coverage of a whole substrate which consist of multiple domains on which boundary defects can occur. Lastly, another method commonly utilized for a mass-production of graphene used in electrochemistry is either chemical or thermal reduction of graphite oxide [38, 39]. Thus obtained graphene sheets have numerous structural defects which can be useful in electrochemical applications.

During graphene growth on a well defined crystal substrate carbon atoms will tend to assemble in a way that minimizes total energy of the system. For a single carbon ring, the most favorable position would be to encircle one substrate atom, but for a whole domain this is possible only if the size of the ring coincides with the atom radius. Of all the metallic substrates that were used for a graphene growth this holds only for Ni(111), while for others there is a small discrepancy. This leads to appearance of a additional superperiodicity in the system, which is known as moiré lattice [41]. For example, Ir(111) has lattice constant of 0.27 nm, while graphene has 0.245 nm, resulting in a hexagonal moiré pattern with a lattice constant of 2.5 nm , as is shown in figure 1.4.

a)

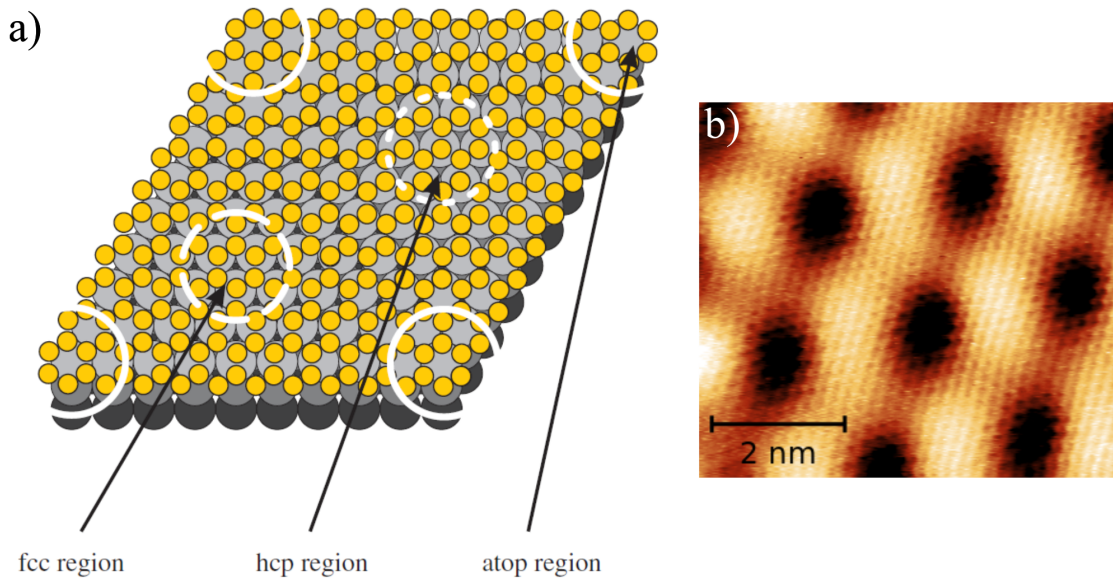fcc region   hcp region   atop region

Figure 1.4: a) Schematic illustration of the moiré unit cell with atop-type region denoted with full circle, hcp-type region with short-dashed circle segments and fcc-type region with dashed circle. Adopted from [40]. b) STM image of graphene on Ir(111) in atomic resolution.

This moiré pattern is very suitable for metallic cluster formation as metals evaporated on such surfaces will often form lattice of metallic clusters which follows a moire pattern beneath it [40, 42] as shown in figure 1.5. These nano-size clusters present a 0D systems that are interesting themselves, as often their structure, electronic, magnetic and optical properties can change with size while new properties can emerge from quantum effects [42]. For the majority of potential applications, clusters are needed on a solid support, ideally forming an ordered macroscopically extending array while being monodisperse and stable to ambient/liquid conditions. Interaction with the substrate should be in the range that allows stability without their decomposition or merging. Such cluster arrays have promising applications e.g. in catalysis or optics.

System of metallic clusters on graphene moiré was extensively studied for a case of Ir clusters on graphene on Ir(111) [40], and later expanded for other metals [42]. Upon deposition of submonolayer quantities of iridium to graphene on Ir(111), array of monodisperse clusters is formed, bound preferentially to hcp region of the moiré [40, 43]. Through the course of cluster formation graphene locally rehybridizes from sp^2 to sp^3 carbon bonds at a hcp site of the moiré unit cell and form new strong carbon-metal bonds. So, while the graphene on Ir(111) is only weakly bound, upon the additional Ir deposition and cluster formation rehybridized carbon atoms at hcp
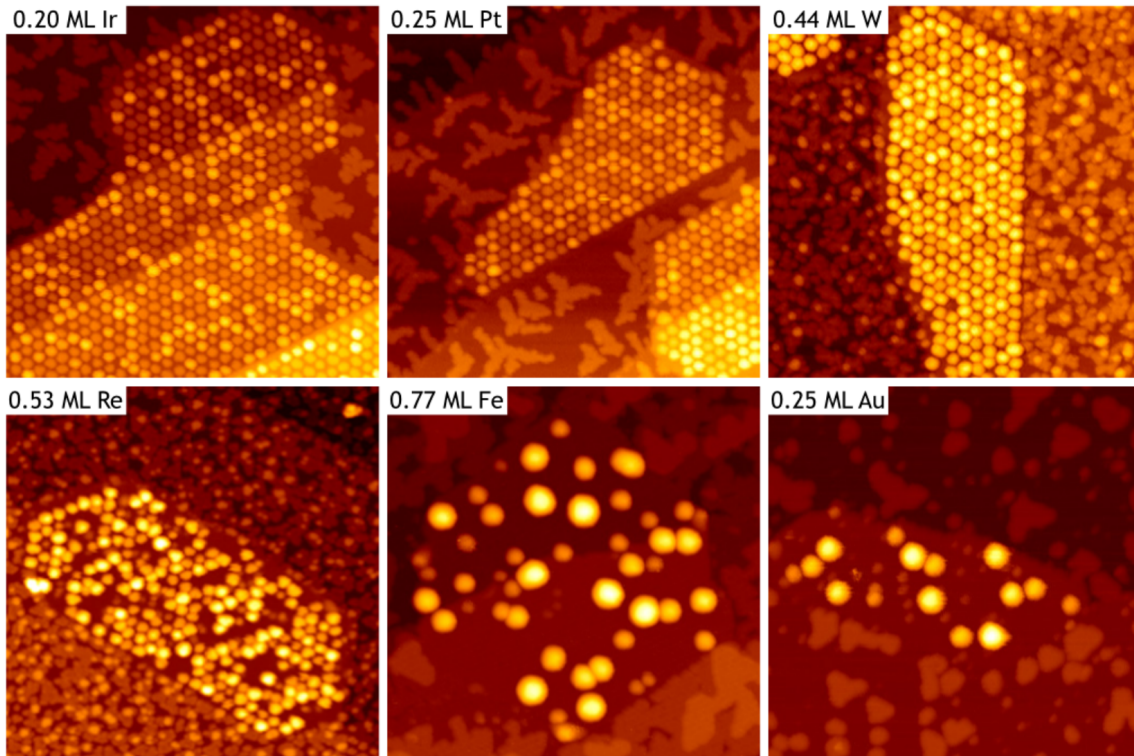
Figure 1.5: STM images of Ir(111) with graphene flakes after deposition of various metals at 300 K. Adopted from [42].

sites have tetrahedral bond angles which can therefore be considered as diamond-like.

1.1.2 MoS_2 monolayer

Of all the possible monolayer TMDs, monolayer MoS_2 is one of the most studied today. Even though TMDs have been widely studied for decades, their role as near-atomically thin materials is relatively new. Renewed interest stem from the recent advances in sample preparation, optical detection, transfer and manipulation and physical understanding of 2D materials learned from graphene. In general, TMDs are a class of materials with the formula MX_2 , where M is a transition metal element from group IV (like Ti, Zr or Hf), group V (for example V, Nb or Ta) or group VI (Mo, W and so on), and X is a chalcogen (S, Se or Te) [18]. They build layered structures of the form X–M–X, with the chalcogen atoms in two hexagonal lattices which are separated by a lattice of metal atoms. Neighboring layers are weakly held by vdW interactions and can thus form the bulk crystal in a variety of polytypes, which differ in stacking orders and metal atom coordination. The overall symmetry of TMDs is hexagonal or rhombohedral, and the metal atoms have octahedral or trigonal prismatic coordination [18]. Despite their similar crystalographic structure TMDs exhibit a plethora of electronic properties ranging from metallic to semiconducting

and also some exotic behaviours like superconductivity and charge density waves [44, 45].

As in the case of graphene, transport and scattering of the charge carriers is confined in the 2D and the mobility of the carriers is affected by several mechanisms including scattering on the acoustic and optical phonons, Coulomb scattering at charged impurities, surface interface phonon scattering and roughness scattering [46, 47]. Effect of the scattering mechanisms on the carrier mobility is additionally influenced by carrier density, temperature, effective carrier mass, electronic band structure and phonon band structure. Moreover, electronic properties of a material can be drastically altered in monolayer limit as compared to bulk. Since the ability of a material to absorb and emit light is directly influenced by its electronic properties, its tunability also effects optical properties of a given material. This can in many TMDs be achieved relatively easy and in many different ways, and will be discussed bellow for the case of MoS_2. Tunable band-gap and impressive mechanical properties (e.g. strength and flexibility) in addition to other properties described above make 2D TMDs promising candidates as building blocks in future applications.
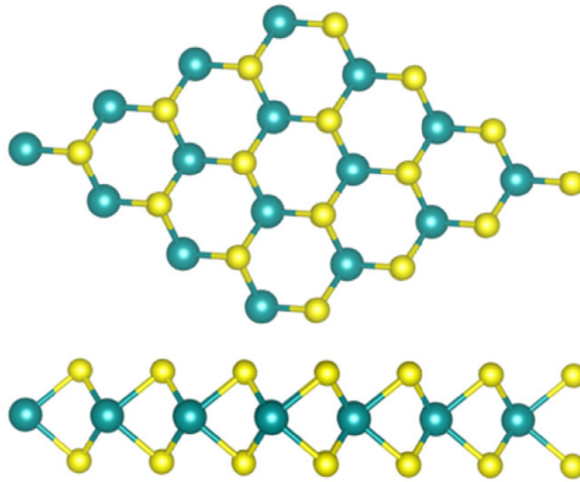
Figure 1.6: Schematic representation of atomic structure of MoS_2 monolayer with Mo atoms in green, and S atoms in yellow. Adopted from [48].

MoS_2 monolayer in particular is extremely stable direct band gap semiconductor with many possible applications as a part of high-performance electronics, phototransistors, photodetectors, sensors, light emitters, various other optoelectronic devices and flexible electronics [17]. It consists of hexagonal layer of molybdenum atoms sandwiched between two layers of sulfur atoms, as shown in figure 1.6, with lattice constant of 3.16 Å and layer thickness of 3.01 Å [49, 50].

While bulk MoS_2 is a semiconductor with indirect gap of 1.3eV, as its number
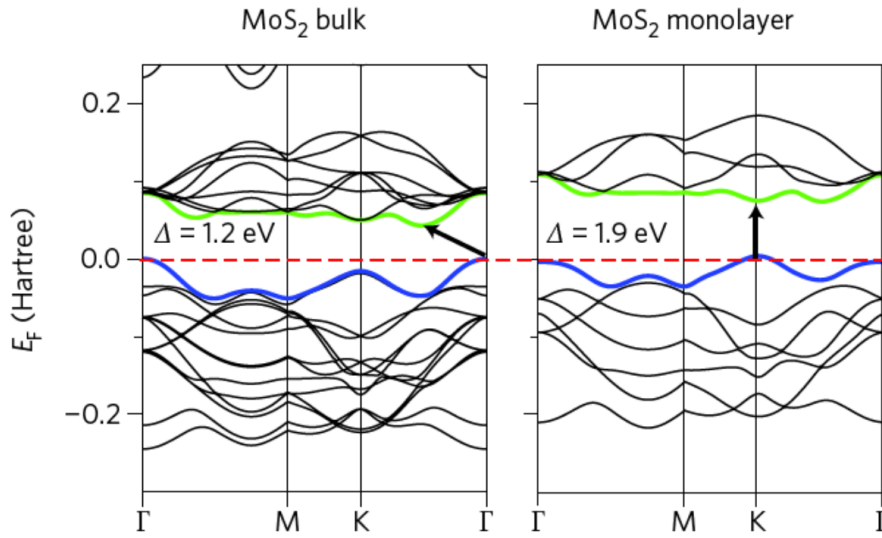
Figure 1.7: Comparison of the band structures for bulk and monolayer MoS$_2$. Adopted from [18].

of layers is reduced its band gap increases and finally converts to a direct band gap (of around 2 eV) in a monolayer limit, due to perpendicular quantum confinement effect [51], as shown in figure 1.7. while the indirect band gap in the case of bulk is strongly influenced by the interlayer coupling (as it is from the top valence band (VB) at the Γ point to the bottom conduction band (CB) halfway between Γ and K points in the Brillouin zone and the energy states near Γ point and the point of indirect band gap originate from a linear combination of d orbitals on Mo atoms and antibonding p$_z$ orbitals on S atoms [52], the direct gap at the K point originates from within a monolayer (as the CB states at the K point are mainly composed of strongly localized d orbital on Mo atoms, which locate in the middle of the S–Mo–S unit cell). Therefore, the direct band gap at K point will increase slightly while indirect will increase monotonically with decreasing the thickness, resulting with a direct band gap at the K point in the monolayer limit.

Strong Coulomb interactions (attributed generally to the reduced dielectric screening in the monolayer samples) induce enhanced many-body electronic effects and consequently formation of many quasiparticles with large binding energy like excitons and trions [53]. An exciton, bound quasi-particle state of one electron and one hole are in monolayer MoS$_2$ formed by strong Coulomb interactions between electrons and holes excited across the direct band gap at the K-point of the Brillouin zone between the maxima of split VB and the minimum of CB. Once formed, the excitons can be trapped on a defect (thus producing a defect-bound neutral exciton, or a defect state or surface state) and the light emission from such states is lower

than the corresponding optical transition of free exciton, rendering a new emission peak in $\approx$0.15 to 0.25 eV below the free-exciton PL peak. Meanwhile, a trion is a quasiparticle containing two electrons and one hole (i.e. a negatively charged exciton) which is a consequence of an free electron binding to a photogenerated exciton [54]. Tightly bound trions can often arise from substrate effects that include heavy electron doping [55]. The transition energy of trion is slightly lower than the corresponding exciton.

Consequently, the photoluminescence (PL) quantum yield (QY) in monolayer MoS_2 is increased by a factor of 10^4 compared to bulk [51]. PL response can be further modulated by various means like different chemical treatments [56], additional defect introduction [57], doping, and strain and temperature induced lattice variations [58]. From the various investigated chemical treatments, most notable is chemical doping with organic superacid of bis(trifluoromethane) sulfonimide (TFSI), which resulted in near-unity PL QY (more then two orders of magnitude increase compared to untreated monolayers) [56].

As defects themselves are source of photoactivity even in the pristine MoS_2, their additional introduction naturally leads to its increase. Additional defects can be introduced in various ways like thermal annealing, plasma treatments, particle or laser irradiation, chemical treatments or physisorption [17]. Even in the naturally occurring 'pristine' MoS_2 a plethora of atomic defects can be found, like S vacancies and divacancies, Mo vacancies, substitution atoms, adatoms and adsorbates [50]. Due to the more complex structure than graphene, defect population is also correspondingly more diverse. PL enhancement resulting from defects introduction has been attributed to the suppression of nonradiative recombination of excitons at defect sites, and also the conversion from trions to excitons (due to the p-doping). It is assumed that the electrons can be effectively localized around Mo-O bond related-defects with relatively high binding energy, which results in efficient radiative recombination of excitons. However, defect introduction is a nonreversible process and in excessive amounts leads to PL saturation and then quenching induced by resulting direct-to-indirect band gap transition in monolayer MoS_2.

Related to the defects is the modulation of charge carriers density, as a very effective method of control of electronic and optical properties of monolayer TMDs, and MoS_2 in particular (as conversions between quasiparticles produce pathway for tailoring of its optical properties). Modifying charge carrier density is conveniently done by doping, which can in turn be done in various ways like solution-based chemical doping, gas physisorption, electrical doping by FET devices, intercalation between the MoS_2 monolayer and substrate (also called substrate effect), building of

vdW heterostructure and previously mentioned introduction of defects. Adsorption of gases and chemical doping are rather similar in a manner that in a both cases charge transfer between 2D material and physisorbed gaseous molecules occurs. PL enhancement of over 100 times has been observed upon physisorption of O_2 and H_2O on monolayer MoS_2, while inert gases like N_2 produced no such effect. [59]. This opens possibility for applications in gas sensing, with already demonstrated prototype of a highly sensitive and selective gas sensor based on the CVD-synthesized MoS_2 [17, 60].

On the side of mechanical properties, MoS_2 exhibits strength 30 times that of steel and average breaking strength of $\approx$23 GPa, that is, it's Young modulus is $\approx$300 GPa and it can be deformed up to 11% before breaking [55, 61]. This makes monolayer MoS_2 rather suitable for applications like reinforcement element in composites or part of flexible electronic devices. Additionally, strain application also influences band gap, due to the fact that crystal lattice constants are altered when force is applied along certain axes. That is, by applying the tensile strain on MoS_2 monolayer decreases the distance between S layers and increases the Mo-S bonds lengths which results in decrease of the orbital hybridization and d-bandwidth which consequently reduces optical gap, while exciton energy remains practically unchanged [62] . Gap is reduced by crossover from a direct to indirect transition, already under strain of $\approx$1% as indirect band gap at Γ point becomes smaller than direct gap in K point and the exciton resonance will red shift.

Another way of modulating optoelectronic properties is by applying external fields, for example, MoS_2 FETs have been demonstrated that can exhibit either n- or p-type doping by applying gate voltage, resulting in the change of carrier density. When considering the substrate effects on optoelectronic properties, there are two possibilities: electrical doping induced by charge transfer across the contact interface between the MoS_2 and the substrate and the substrate-dependent interference and absorption effects. The investigation of the Raman and PL spectra of MoS_2 monolayer on different substrates (dielectric and conducting) showed that the spectral weight between exciton and trion in PL and the frequency of A_{1g} Raman mode strongly depends on the substrate [63]. These effects were attributed to the substrate induced doping and change in the decay rates of the excitonic transitions.

MoS_2 also exhibits strong spin-orbit coupling which results in splitting of valence band in K point and induces two direct interband optical transitions, namely, the A and B excitons, both observed in PL and absorption spectra. Spin-orbit coupling and inversion symmetry breaking introduce coupled spin and valley physics that make it possible to control spin and valley degrees of freedom.

In addition to the ability of continuous modulation of the electronic structure and optical response, MoS_2 monolayers also exhibit mobility of at least 200 cm^2/Vs and a high current on/off ratio at room temperature. Previously mentioned enhanced Coulomb interactions that arise from reduced dielectric screening and relatively heavy particle band masses in monolayer MoS_2 give an ideal opportunity for exploring some fundamental issues of many-body correlated quasiparticles, like tightly bound negative trions. Furthermore, the fact that the valley and spin can be efficiently controlled by optical helicity, electrical and magnetic field, opens an opportunity for valleytronics applications with the valley indexes serving as information carriers [64].

1.2 DNA-based constructs

Natural structure and properties of a DNA molecules makes them extremely suitable for use in nanotechnology: with a diameter of $\approx$ 2 nanometers, modular structure and self-recognition properties of the base pairs, they are already practically a form of nanotechnology by themselves. Already back in 1982 Seeman proposed that DNA molecules can be used as building blocks for the assembly of geometrically defined objects with nanoscale features [65]. This revolutionary idea encouraged emergence of a new research field of a structural DNA nanotechnology. Additionally, as a chemically based (self)assembly system, DNA can be easily utilized in a number of bottom-up approaches to nanotechnology.

First approach to development of DNA based architectures is the multistranded approach (shown in figure 1.8a). This approach uses the self-recognition properties of DNA, to design the oligonucleotides that will self-assemble with each other based on the complementarity of base pairing and form a well-defined branched DNA motif. Such a motif, often called DNA tile, can then be further used as a building block in the assembly of discrete finite objects or infinite periodic lattices through sticky-end cohesion [67].

Second approach was developed in 2006 when Rothemund introduced scaffold-based DNA origami [68]. This approach uses folding of a long single-stranded DNA strand that serves as a scaffold by binding it with the hundreds of short oligonucleotides that serve as a staple strands into a desired form (as shown in figure 1.8b). The self-assembly is facilitated by annealing the scaffold macromolecules in the presence of an approximately 100-fold excess of staple strands for about one hour and results the extremely high percentage of the correctly assembled target structure. An overview of some of the structures realized till nowadays is shown in figure 1.9.
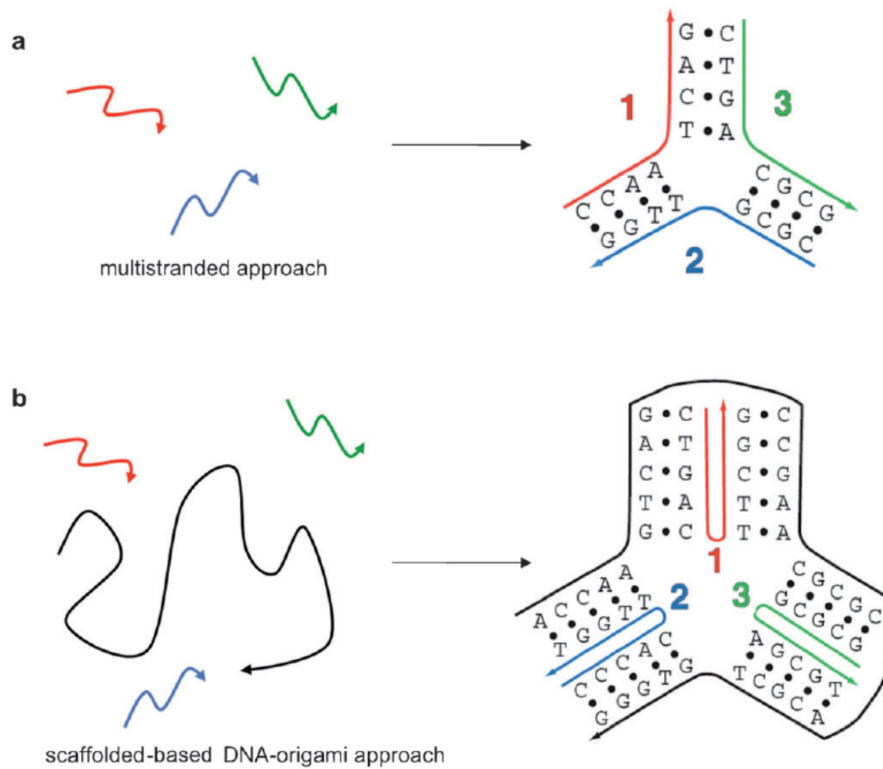
Figure 1.8: Schematic illustration of the two approaches to construction of DNA-based architectures. a) Multistranded approach. b) DNA origami technique. Adopted from [66].

DNA origami can further be functionalized in a controllable way with standard chemical groups used in biotechnology (ligands like biotin or thiol or fluorophores), which opens opportunity of combining them with other nanostructures, like metallic nanoparticles or some other biomacromolecules.

1.3 Hybrid materials

Both deoxyribonucleic acid (DNA) and two-dimensional (2D) materials based nanotechnology hold great potential for the development of extremely small devices with increasingly complex functionality. Decorating 2D materials with DNA (or other biomacromolecules) could lead to applications in (bio)chemical sensing [70, 71]. That is, in parallel with the development of 2D materials for applications in electronics, efforts are directed towards combining biological structures (as they are already nanomachines themselves) with the solid-state technology [72]. Recently, a doping effect was also found upon deposition of DNA on a 2D material for a disordered DNA overlayer [71]. DNA may additionally be combined with other materials like metallic nanoparticles (clusters), and arrays of these may form on DNA origami

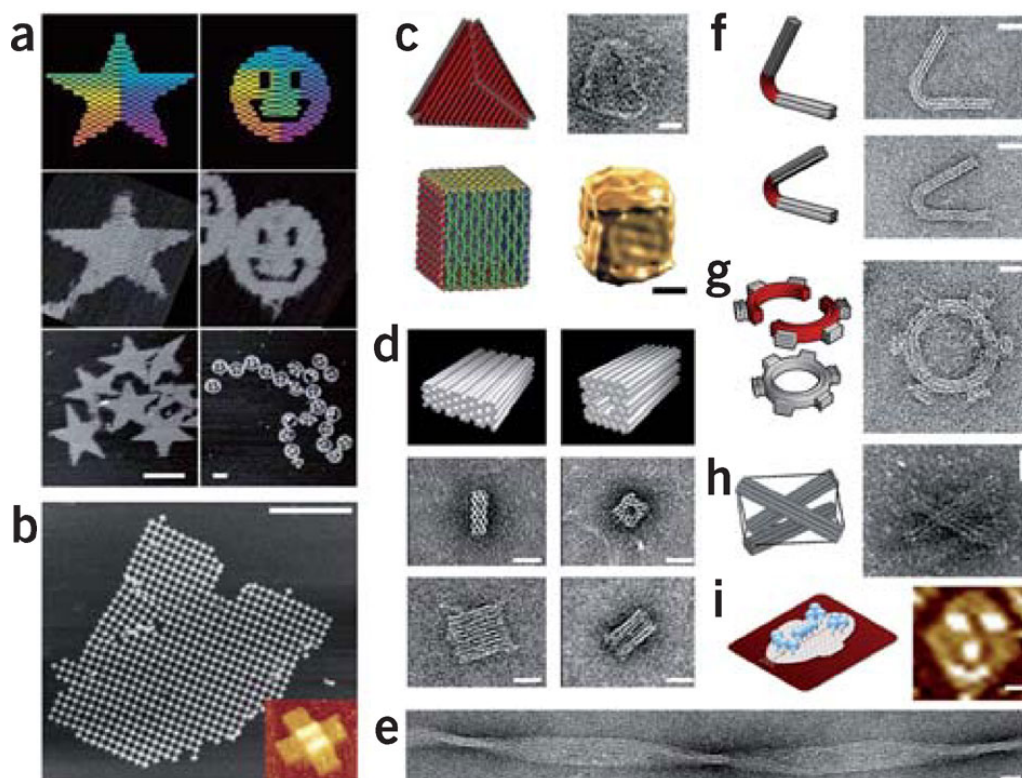**Figure 1.9: Some of the nanostructures built using DNA origami. (a) Single-layer DNA origami shapes (top) and AFM images of these objects (middle and bottom). The star and the smiley each have diameters of ≈100 nm. (b) DNA origami array formed from several hundred copies of a cross-shaped single-layer DNA origami object imaged by AFM. Inset shows 100 nm long cross-shaped origami monomer. (c) Container-like DNA origami objects (left) imaged with negative-stain TEM (top) and cryogenic TEM (bottom). (d) Multilayer DNA origami objects. (e) Multimeric multilayer DNA origami object with global twist deformation. (f,g) Multilayer DNA origami objects such as bent bars (f) and a gear with square teeth (g) displaying custom curvature. (h) Tensegrity prism created by combining multilayer DNA origami struts and ssDNA strings. (i) Single-layer DNA origami shape with site-directed protein attachments. Adopted from [69].**

template [73]. That is, two routes are complementary within this field: modifying the 2D crystal with DNA origami structures and controlling the assembly of DNA nanostructures and other biofunctional or compatible macromolecular assemblies with the nanopatterned support acting as a template. That is, self-assembled monolayers of small molecules, e.g. alkanethiols on gold or alkylsilanes on OH- surfaces are a known and routine method of engineering biocompatible and biofunctional solid-state surfaces [74, 75]. Ordered arrays of biomacromolecules like DNA or avidin could open routes to new biosensing applications [76] where different biomacromolecular pixels could be addressed or read by the underlying 2D electronic material instead of biochemical patterning [77].

As opposed to non-specific adsorption of DNA on graphene, in order to produce stronger, directed and specific binding, thiol bond can be utilized. Thiol bond is the covalent bond between gold and sulfur which results in very robust and adjustable interactions which are crucial in stabilization of nanostructures and transmission of electronic interactions between gold and sulfur-containing organic molecules [78]. These interactions which are usually mediated through the sulfhydryl functional group in thiols are extensively used in different areas of advanced research, like surface and materials science, molecular biology and inorganic chemistry. Wide spread of potential applications include drug delivery, molecular electronics, site-specific bioconjugate labelling and sensing. Bond is formed upon interaction at the gold-sulfur interface which results in deprotonation of the sulfydryl group and creation of thiyl radical (RS•), as opposed to the protonated SH group which can interact with gold only by weaker coordination-type bonds through the sulfur lone-pair electrons. Strength of the thiolate-gold (RS-Au) bond is close to that of the gold-gold bond, meaning that it can significantly modify the gold-gold bonding at the gold-sulfur interface. This leads to a rich chemistry of nanometer-scale gold constructs, as opposed to chemical inertness of a bulk gold.

1.4 Outline

Objective of this dissertation is design and construction of a hybrid system consisting of a suitable solid state substrate and layer of biomacromolecules. Such hybrid systems are currently widely studied, as they not only bridge the gap between living matter and technology but also have promising applications in nanotechnology as single molecule sensors or as part of bio-optoelectronic devices. During the research presented in this thesis, focus was mainly on the reproducible preparation and extensive characterization of the nanopatterns themselves, as they can later be used as a supports for different biomacromolecular layers. We started with both subsystems that possess similar symmetry or arrangement on a longitudinal scale: (nanopatterned) substrate consisting of a two-dimensional (2D) support (graphene or monolayer MoS_2) and adsorbed layer of biomacromolecules. Subsystems were first assembled and characterized separately, followed by assembly of a hybrid systems, as outlined below.

Chapter 2 gives overview of the materials and methods used in the experiments. Description of the experimental methods can be divided in two parts: first part deals with synthesis and characterization of the substrates and nanotemplates in UHV conditions and the second part is focused on synthesis, manipulation and

characterization of 2D materials and biomacromolecules under ambient conditions.

Chapter 3 focuses on results of incubation of gold substrates with DNA biomacromolecule in two forms, short strands and tetrahedra constructs, all chemically functionalized with disulphide groups. Several different types of gold surfaces were explored, in different incubation conditions (concentration, length, pH, etc.). Adsorption process was followed using QCM-D and the deposited layers were checked with AFM.

Chapter 4 deals with synthesis of a DNA-graphene hybrid. DNA binding to graphene is realized through binding to an array of AuIr nanoclusters. First, the work to find parameters for the synthesis of the metallic nanocluster array is presented, which is followed by description of the clusters themselves. Furthermore, the study of stability of the nanotemplate is given and finally the experiments on DNA tetrahedra adsorption on the nanotemplate alongside further characterization studies.

Chapter 5 considers DNA origami interactions with MoS_2 monolayer. After the synthesis and initial characterization of the MoS_2 monolayer, monolayer is transferred to a metallic substrate to enable detailed characterization on the atomic level (by STM). Features of the monolayer were imaged down to atomic level, with focus on atomic defects. Additionally, its electronic properties were explored with PL and STS. After adsorption of DNA tetrahedra, another extensive characterization was conducted.

Materials and methods

Experimental work presented in this thesis including both sample preparation and characterization was carried out either under ultra-high vacuum (UHV) conditions or under ambient conditions and/or in solutions, at several laboratories at Institute of physics, Zagreb, unless noted otherwise. UHV synthesis and characterization was carried out in UHV-STM chamber. Ambient synthesis of 2D materials, and also their lift-off and transfer to different substrates was done by D. Čapeta. Stability of 2D templates under ambient conditions was tested, followed by the DNA deposition, and then returned to UHV chamber for further imaging. Solutions of biomacromolecules samples (DNA tetrahedra) were prepared according to protocols described below and their quality was checked with electrophoresis. Quartz crystal microbalance with dissipation monitoring (QCM-D) was used for calibration of the deposited amount of biomacromolecules. Templates and final hybrid materials were characterized with atomic force microscope (AFM), scanning tunneling microscope (STM), scanning electron microscope (SEM) and optical measurements (photoluminescence (PL) and Raman measurements), depending on a sample. Optical measurements were performed by N. Vujičić. SEM measurements were conducted at Faculty of Chemical Engineering and Technology, University of Zagreb, by F. Faraguna using VEGA 3 TESCAN microscope, with a detector of secondary electrons (energies 5-10 kV).

MD simulations of AuIr system were preformed by P. Lazić, I. Lončarić and R. K. Trivedi from Ruđer Bošković institute, Zagreb. DFT simulations of $MoS_2/Ir(111)$ system were performed by B. Biel and A. Gallardo from Department of Atomic, Molecular and Nuclear Physics, Faculty of Science, University of Granada, Spain and Pablo Pou from Departamento de Física Teórica de la Materia Condensada & IFIMAC Facultad de Ciencias, Universidad Autónoma de Madrid, Spain.

2.1 Synthesis and characterization in UHV conditions

2.1.1 Substrate preparation

Preparation of most substrates was done in a UHV chamber under base pressure in the range of 10^{-9} mbar. Chamber consists of two main parts: one for a sample preparation and basic characterization (prep-chamber) equipped with Ar^+ sputtering gun, valves for dosing controlled amounts of gases (O_2, Ar, C_2H_4), metal evaporators and LEED setup for preliminary checks of sample quality. Second part houses UHV-STM and garage for storage of up to 5 samples. The sample heating of up to 1250°C is done via radiative and e-beam heating from the back of the sample. The sample temperature is monitored with K type thermocouple (chromel vs. alumel) in a direct contact with the crystal and an optical pyrometer. Loadlock mechanism mounted on a prep-chamber enables relatively fast insertion and extraction of the samples without loss of UHV conditions in the chamber, which can be done overnight, as opposed to opening the chamber (and losing UHV conditions) that takes about a week.

Two types of well defined (111) surfaces of single crystals were used as a substrates: Ir(111) and Au(111). Single crystals with a hat-shape form with a typical diameters of 6-8 or 8-10 mm, orientation accuracy better than 0.1° and purity of 99.99% were obtained from Mateck GmbH, Germany. Before use Ir (Au) crystal surface is cleaned during several sputtering-annealing-flash cycles. Ar^+ sputtering is done with sample kept at the room temperature with the ion energies of 1.5 keV (1 keV), (Ar pressure of 1.2×10^{-6} mbar), for 1-2 hours. After the sputtering, sample is annealed in oxygen atmosphere of 10^{-7} mbar, at 1000°C (700°C for Au(111)), for 5-10 minutes, finishing with a flash: heating of a sample up to 1250°C (850°C for Au(111)). These procedures ensure that most of the adsorbates on the surface are removed, leaving clean surface of a high structural quality constituting of a large (cca 100 nm) terraces separated by mono-atomic steps. Quality of the surfaces is checked by LEED, and cleaning procedure is repeated until sharp spots are obtained in a diffraction image.

2.1.2 Nanotemplate synthesis

Monolayer graphene is grown on a cleaned Ir(111) surface using two similar previously established procedures: temperature programmed growth (TPG) and chemical vapor deposition (CVD) [37]. For the TPG ethylene (C_2H_4) is deposited

on a sample at room temperature, by flowing the UHV chamber with 2×10^{-7} mbar of C_2H_4 for 1-2 minutes. After the valve is closed and pressure drops back to base, sample is shortly annealed at 1200°C (for $\approx$ 30 sec). Before the CVD sample is allowed to cool down below 200°C. CVD consists of preheating the sample to 850-1000°C, followed by release of 3×10^{-7} mbar of C_2H_4 for 5-10 minutes. To obtain best results (full monolayer coverage with single R0 orientation), one cycle of TPG is used, followed by several CVD cycles. Since the solubility of carbon in iridium is negligible [79] multilayer graphene growth does not occur in these procedures and once the whole surface is covered growth stops. Tungsten and iridium were evaporated using EFM 3 UHV Evaporator from Omicron, while for vanadium and molybdenum an older evaporator with similar design was used. Gold was evaporated from a home-made dispenser consisting of tungsten wire basket by passing up 6 A of current through it. For the intercalation of alkali metals (Cs and Li) commercially available dispensers from SAES Getters were used.

2.1.3 Scanning tunneling microscopy and spectroscopy (STM&STS)

Quantum effect of electron tunneling is the basic principle of scanning tunneling microscopy [80, 81]. Tip of a metallic needle that serves as a scanning probe is positioned sufficiently close (typically few Å) to the conducting surface, in order to achieve overlap of surface electrons wave functions between sample and the probe (tip), i.e. so that potential barrier between surface of the sample and tip becomes sufficiently narrow. Applying the bias voltage V_b between sample and the tip induces difference in respective Fermi levels, which further enables electron tunneling through vacuum barrier from higher to lower Fermi energy region, to fill in empty states. Resulting tunneling current I_t enables tracing of the surface with atomic resolution. Applied bias voltage has to be sufficiently small (in the order of 0.1 V), because higher voltages deform the barrier too much, resulting in field emission from the tip and strong interaction between sample and tip, with the resulting current no longer being tunneling current. Typical barrier height is 5 eV, which is the average work function of a metal surface.

Since the tunneling current depends on the overlap of the wave functions, it obviously depends on the distance d between apex of the tip and sample surface. The parallel can be drawn with the simple model of the tunneling between two

identical planparallel electrodes:

$$I_t \sim V_b e^{-2\kappa d} \tag{2.1.1}$$

where

$$\kappa = \frac{\sqrt{2m\phi}}{\hbar} \tag{2.1.2}$$

is inverse decay length for the wave functions in vacuum, ϕ is work function, m electron mass and $\hbar$ Planck constant [82].

This is a simplest 1D model that doesn't take into the account real geometry of the tip and the sample. Since real geometry of the tip apex is never truly known and is different for every probe, some approximations have to be taken into the account in order to derive relations that are simple enough to use, yet still good enough to describe more realistic situation. Such approach was developed by J. Tersoff and D. R. Hamann [83, 84]. They used Bardeen formalism in the low temperature limit and got the following relation for tunneling current:

$$I = \frac{2\pi}{\hbar} e^2 V \sum_{\mu,\nu} |M_{\mu\nu}|^2 \, \delta(E_\nu - E_F) \delta(E_\mu - E_F) \tag{2.1.3}$$

where e is the electron charge, V *is* the applied voltage, $M_{\mu\nu}$ is the tunneling matrix element between states Ψ_μ (of the tip) and Ψ_ν (of the surface), $E_{\mu,\nu}$ is the energy of the state $\Psi_{\mu,\nu}$ without tunneling, and E_F is Fermi level. Approximation is valid because experiments are conducted at a room temperature or lower, and tunneling is in only one direction. If tip of the probe is further approximated by ideal point probe its wave function is described by delta function and 2.1.3 becomes:

$$I \sim \sum_\nu |\Psi_\nu(\vec{r_0})|^2 \, \delta(E_\nu - E_F) \tag{2.1.4}$$

meaning that tunneling current is directly proportional to the local density of states (LDOS) at Fermi level of the surface $\rho(E_F)$. It follows then from the previous discussion that the tunneling current is in the form of

$$I \sim \rho(E_F) V e^{-2\kappa d} \tag{2.1.5}$$

meaning that the topography obtained by scanning the tip across the surface is in the fact contour map of the constant surface LDOS (at the Fermi level). Since tun-

neling current is strictly monotonically decreasing function of the distance between the sample and the tip it is possible to establish relatively simple feedback loop mechanism controlling that distance. Simplified schematics and the principle of the scanning tunneling microscope is shown on figure 2.1.
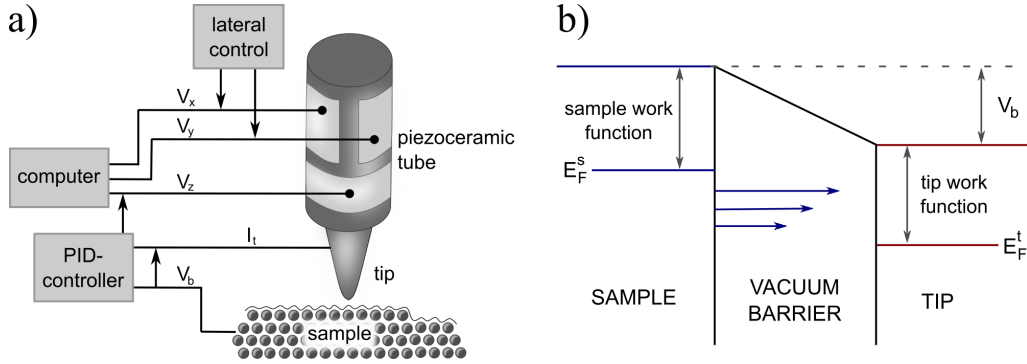

Figure 2.1: a) Simplified schemtaics of the STM operation. b) Electron tunneling between the tip and the surface.

Every probe tip has different arbitrary shape, but if it's assumed that is locally spherical with a radius R, estimation of the lateral resolution yields $\triangle x = \left[\frac{2(R+d)}{\kappa}\right]^{1/2}$ [83]. If the typical value of the work function is considered ($\phi = 5$ eV), along with the $R+d$ between $0.5 - 1.0$ nm lateral resolution of ~ 0.4 nm is obtained, which is in the range of typical interatomic distances in a crystal.

There are two different imaging modes of STM operation [81]. More commonly used is constant current mode (sometimes also called topography mode), when tunneling current is kept constant by continuous adjustment of tip-surface distance, as shown in Figure 2.2a. Adjustments are done via feedback voltage on the z-piezo V_z, and the STM image is generated from the height of the tip $z(x,y)$ as a function of the lateral movements of the tip x,y. Height dependence is obtained from the feedback voltage needed to keep the tip-surface distance constant. Speed of the feedback loop mechanism is the main limiting factor on the maximum imaging speed in this mode of operation. Other possible imaging mode is a constant height mode, which is not used very often because it's suitable only for imaging of a very flat surfaces without prominences taller than few Å. In this mode height of the tip is held constant, feedback loop voltage is not applied, the tip scans the surface rapidly and the image is obtained from tunneling current as a function of the position above the surface $I(x,y)$, as is shown in the figure 2.2b.

Atomic resolution which can be easily obtained even in the ambient conditions makes STM ideal tool of the nanoscience, but the interpretations of the results should always take into the account the fact that the obtained images are not necessarily
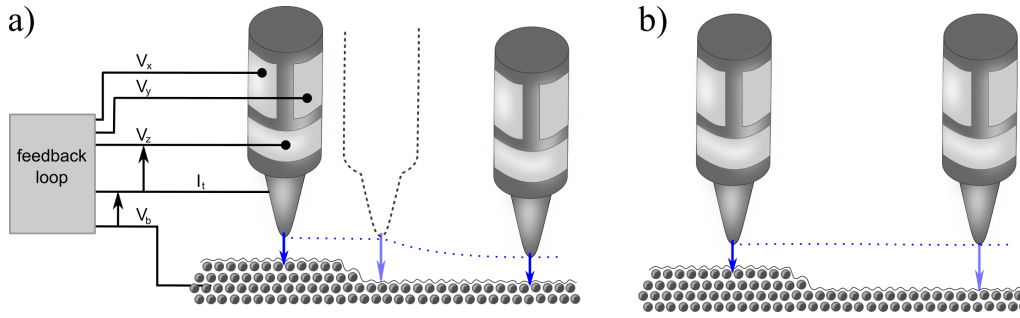
Figure 2.2: Two modes of STM operation: a) constant current mode and b) constant height mode.

topography images, but topography in the sense of LDOS of the surface electrons. Furthermore, due to the nonzero tip radius, certain artifacts can appear in the images and give seemingly meaningful results, while in fact being just the reflection of the specific geometry of the tip. However, due to the fact that the tunneling current is a monotonic function of the tip-sample distance, even for a relatively blunt tips there is high probability of the one atom on the apex which is isolated enough to carry the majority of the tunneling current, so such artifacts are more rare in STM imaging compared to AFM. As was previously mentioned, additional limitation that comes from the fundamental principles on which STM is built is possibility of imaging only the (enough) conductive samples. In the addition of imaging, STM is also used for spectroscopic measurements of the local electronic structure (STS). This is done by interrupting the feedback loop while keeping the tunneling gap constant. Then, if a voltage ramp is applied, measurement of a tunneling current in a dependence of a bias voltage gives spectra of a convolution of a tip and a sample LDOS [85]. In order to eliminate tip contributions and obtain reproducible spectra some specific requirements have to be met, namely spectra should be measured with a relatively blunt tip and with a large tip-sample distance (small tunneling current and large bias voltages).

STM and STS measurements in UHV were conducted with the Specs Aarhus VT-STM setup placed in a UHV chamber with a base pressure of 10^{-9} mbar. Measurements were done at room temperature, with the STM tip grounded and the sample put to a bias voltage. For the STM measurements in air a home-built STM of the Besocke type [86] was used, modified according to [87]. Electronics controlling the setup is completely realized according to [87]. Additional noise and vibration dampening was added. The STM images were processed using WSxM [88] and Gwyddion [89] software.

2.1.4 Low energy electron diffraction (LEED)

LEED [82] is a technique commonly used for preliminary characterization of surface structure in most UHV surface sensitive studies. It uses an electron gun which produces parallel beam of electrons of well defined energies (0-1000 eV, typically around 100 eV). Diffraction image is formed only from electrons that are elastically scattered from a surface (typically first few atomic layers), while the rest of them is eliminated with the system of metallic grids. Electrons which pass through fall on a fluorescent screen and form the image of a reciprocal lattice of a surface which directly reflects surface ordering. In this way, quality and contamination of the surface is easily monitored, as adsorbates will commonly either diffuse surface lattice, or form reconstructed one. Measurements are done at room temperature, with Omicron LEED system and the image from the screen was recorded with a Logitech C920 HD web camera.

2.2 Synthesis and characterization under ambient conditions

2.2.1 Graphene lift-off and transfer

The surface of a Ir(111) crystal covered with graphene was coated with a drop of 2% solution of Poly(methyl methacrylate) (PMMA) in anisole (Allresist AR-P 672). The sample was then dried until the PMMA solidified forming a reinforcing thin film on the graphene. Such film was subjected to electrochemical delamination [90, 91]. The crystal was immersed in a 1M NaOH solution and connected as the cathode while a piece of Pt foil served as an anode. The electrochemical process was divided into two steps. First, a voltage of around 1.2 V was applied which is sufficient to induce intercalation of electrolyte between graphene and Ir [92, 93, 94]. The edge of the intercalation front is visible under optical microscope as interference lines [92]. Second step of the process includes application of higher voltage (around 2-3 V) above the threshold for hydrogen evolution where large bubbles of H_2 gas lift the graphene together with PMMA layer from the Ir substrate. Graphene with PMMA was subsequently washed in deionized water and transferred onto a Si wafer terminated by 285 nm thick layer of SiO_2. PMMA was then removed by repeatedly washing the sample with dichloromethane. The final result of the transfer process is a graphene sheet of 6 mm in diameter on Si/SiO_2 visible with a naked eye.

2.2.2 MoS_2 synthesis and transfer

MoS_2 was grown in homemade CVD system using aerosol assisted CVD. MoO_3 precursor was aerosolized in 100SCCM ultra pure argon using 0.5 W 450 nm laser diode for local heating. Sulfur vapor was produced by heating 50-100 mg of S to 140°C by separate heater. Growth substrate, 285 nm SiO_2 on highly doped Si, was placed in center of furnace and heated to 750°C during growth. After growth, the substrate was cooled in furnace to 200°C in Ar stream before removal. Ir(111) single crystal was cleaned in UHV chamber using previously described Ar^+ sputtering - O_2 annealing cycles. Quality of surface was confirmed with LEED and STM before taking crystal out of UHV chamber. Ir(111) was taken out of UHV chamber via load-lock mechanism, and MoS_2 was transferred to Ir(111) using commercial polydimethylsiloxane (PDMS) film (X0 Gel-Film from GelPak)[95]. Briefly, wafer with grown MoS_2 was covered with the PDMS film and floated on deionized water [96, 97]. Penetration of water between the MoS_2 and SiO_2 caused delamination of the support film and MoS_2 in few minutes. Released PDMS/MoS_2 film was lifted with tweezers and, after drying, put in contact with the Ir(111) single crystal. Transfer process was completed by slowly lifting the PDMS film using micromanipulator. After the transfer, sample was immediately returned to load-lock, with the whole procedure done within 30 minutes from taking it out. Sample was annealed at 400K (125°C) for $\approx$ 12 hours in UHV before STM imaging.

2.2.3 DNA tetrahedra synthesis and characterization

DNA origami tetrahedra are synthesized from four (55nt $\approx$ 19 nm long) DNA oligonucleotides with sequences according to table 2.1 that were adopted from [98]. They carry chemical modifications of either a disulfide group (DS), a biotin (BT), or a Cy5 group at the 5'-end, and were received lyophilized from Microsynth, Switzerland. Before use, samples were dissolved in deionized water, down to 50 μM molecules concentration. Hybridization of oligos was done mixing 10 μl of 50 μM solutions of each of four strands in 1x TM buffer and 0.5 M NaCl, to obtain 5 μM tetrahedra solution. Once mixed, sample was put in contact with thermal bath at 95°C and slowly cooled down to 65°C over the course of 25-30 minutes, and then quenched to 4°C. Schematic illustration of a tetrahedron formation is shown in figure 2.3a, along with the schematic of an assembled tetraheron with edges of $\approx$ 5 nm in length (figure 2.3c). The resulting DNA tetrahedra have disulphide groups at three vertices and biotin on the forth [99]. Quality of the samples was checked using polyacrylamide gel electrophoresis (PAGE, 11%; 1.9 ml A-BA, 2.4 ml H2O, 1 ml 5x TBE) in 1x

Table 2.1

Names, Chemical Modifications, and Sequences of DNA Oligonucleotides. Adopted and slightly modified from [99].

oligo	Sequence and Optional Modification
o1	5'- ACATTCCTAAGTCTGAA AC ATTACAGCTTGCTACAC GA GAAGAGCCGCCATAGTA -3'
o2	5'- TATCACCAGGCAGTTGA CA GTGTAGCAAGCTGTAAT AG ATGCGAGGGTCCAATAC -3'
o3	5'- TCAACTGCCTGGTGATA AA ACGACACTACGTGGGAA TC TACTATGGCGGCTCTTC -3'
o4	5'- TTCAGACTTAGGAATGT GC TTCCCACGTAGTGTCGT TT GTATTGGACCCTCGCAT -3'
o1-DS	Sequence of Oligo-1 carrying a disulfide group via a hexamethylene (C6) linker at the 5' end
o2-BT	Sequence of Oligo-2 carrying a biotin group via a tri(ethylene glycol) (TEG) linker at the 5' end
o2-Cy5	Sequence of Oligo-2 carrying a Cy5 group via a TEG linker at the 5' end
o3-DS	Sequence of Oligo-3 carrying a disulfide group via a C6 linker at the 5' end
o4-DS	Sequence of Oligo-4 carrying a disulfide group via a C6 linker at the 5' end

TBE buffer (pH 8.3) under constant current of $\approx$ 10 mA (150 V, 5-15 mA) at $\approx$ 10°C for 75 minutes. Samples were diluted to concentration of 125 nM in TE buffer and 10% glycerole and 15 μl of this solution was applied on the gel. Typical result is shown in image figure 2.3b. For the deposition on the substrates 5 μM stock solution was diluted down to 125 nM in TE buffer and 100 μl droplet of this solution was applied to the clean crystal surface for 45 minutes, washed with 2 ml of EtOH:H$_2$O 1:1 mixture, then 3 ml H$_2$O, and finally dried in nitrogen stream.
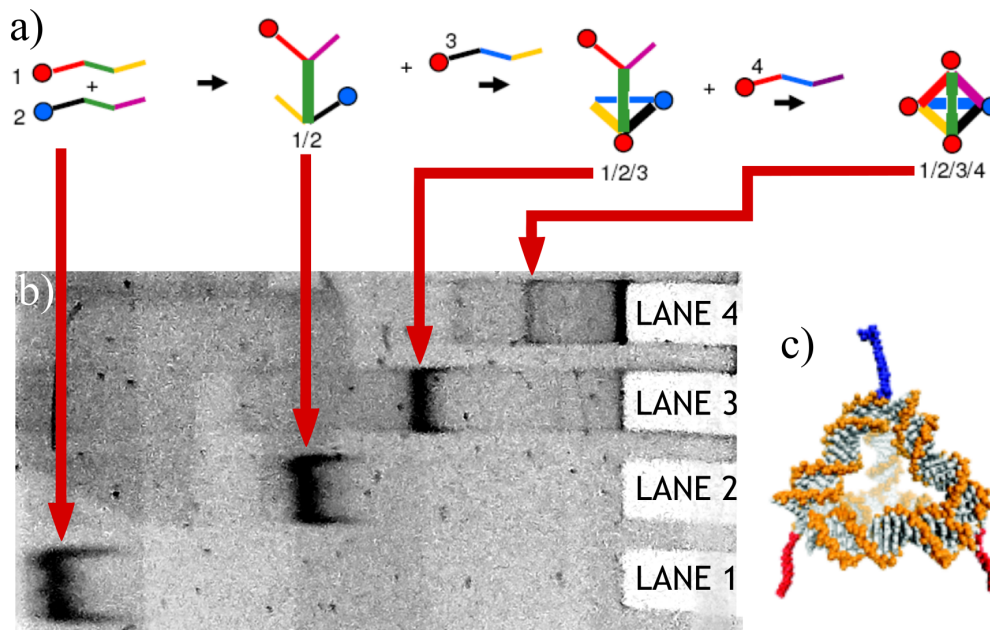

Figure 2.3: a) Step-wise formation of DNA tetrahedrons from oligonucleotides o1-DS, o2-BT, o3-DS and o4-DS shown schematically. b) Image of a gel electrophoresis of 4 possible steps in a tetrahedra formation (lane 1: oligomer, lane 2: dimer, lane 3: trimer, lane 4: tetrahedra). c) Schematic of an assembled tetrahedron. Adopted from [100].

2.2.4 Atomic force microscopy (AFM)

Although technique similar to STM in the manner of characterization of the surface with the scanning probe, and moreover developed from STM, AFM works on a fundamentally different physical principle which enables it to scan even the non-conductive samples [101, 102]. AFM's principle of operation is based on inter-molecular interactions between the sample and the probe with the sharp tip that scans the surface. Potential energy U_{ts} between the tip and the sample generates the force

$$F_{ts} = -\frac{\partial U_{ts}}{\partial z} \tag{2.2.1}$$

and depending on the mode of operation, the AFM measures F_{ts} or some variable derived from it. During the scanning, tip-sample distance is recorded, and the surface topography is derived from it. Schematic view of the AFM operation is shown in figure 2.4a.
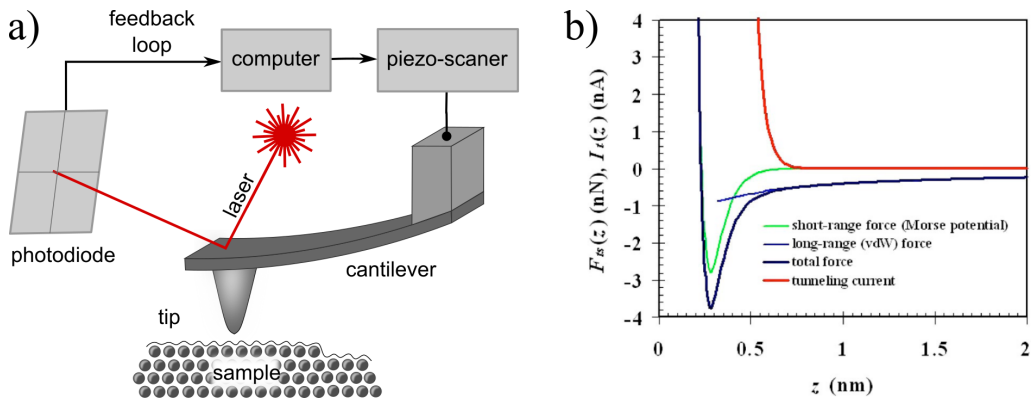

Figure 2.4: a) Simplified schematcs of AFM operation. b) Generalized view of the forces during AFM imaging and their comparison to the tunneling current. Adopted from [102].

Unlike the tunneling current which has rather short range, F_{ts} is composed from both short and long range components. To begin with, in vacuum there are short range chemical interactions (in a range of few Å), van der Walls, electrostatic and magnetic interactions (in a range up to 100 nm). Furthermore, in ambient conditions there are additional forces like meniscus forces (resulting from water and/or hydrocarbons adhesion layers formed on a tip and sample) and solvation forces in the solutions. Due to this abundance of different interactions U_{ts} can't be written in an analytical form, so approximate forms like Morse, Lenard-Jones or Stillinger-Weber potential are used for the general considerations of the tip-sample interactions [102].

Typically, force is attractive at larger distances, and becomes repulsive at closer range. General form of the force and its comparison to the tunneling current is shown in figure 2.4b. Due to nonmonotonic form of the force, it is possible to establish stable feedback loop only on the ranges of the curve that are locally monotone. So, we can classify different modes of AFM operation by the ranges of the force in which measurements are conducted. The most basic differentiation is on contact (also called static, or DC mode) and noncontact (also known as dynamic, or AC mode), the latter shown schematically in figure 2.5. Throughout the imaging in the contact mode, tip of the probe is in the direct contact with the sample, i.e., in the repulsive regime. Meanwhile, in the dynamic modes of operation, tip is oscillating at some excitation frequency, and we can further differentiate into two dynamic modes: amplitude modulation and frequency modulation. Additionally, it should be noted that AC mode is not necessarily non-contact - there is also an imaging mode in which tip touches the surface in the points of maximum amplitude (so called intermittent contact mode).
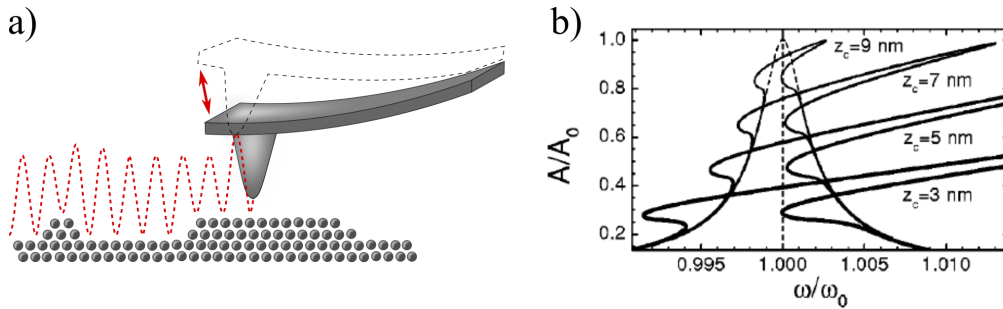

Figure 2.5: a) Schematic representation of an AFM dynamic mode of operation. b) Resonance curve of an AFM cantilever for different values of z_c. Adopted from [103].

For imaging biomacromolecules deposited on a surface, most commonly used mode of operation is dynamical mode with amplitude modulation: amplitude modulated AFM - AM-AFM in short, described in the following. Typical probe used in AFM measurements consists of a thin elastic beam - a cantilever, with a sharp tip on its end, as shown previously in figure 2.4a. In the dynamic imaging mode, cantilever-tip system is excited with external frequency, usually close to its resonant frequency. When the tip-surface distance is sufficiently small, F_{ts} affects cantilever oscillations and changes its amplitude, phase and frequency. Feedback loop keeps the amplitude constant, and from the changes in the parameters that are keeping the amplitude constant (usually voltage on the piezoelectric probe holder) topographic image of the surface sample is derived (figure 2.5a). Changes in the phase give additional information about the surface of the sample. For the more detailed deliberation

of the influence of the F_{ts}, closeness of the surface and its local properties on the movement of the probe equation of motion should be considered. For that several approximations have to be introduced, while problem is further complicated by the fact that there are nonlinear forces at show, which make it impossible to have analytical results. So, in order to do that, equation of the motion should be examined in more detail. Although the probe is cantilever shaped, if that is taken into account the problem complicates dramatically, while the approximation of a point mass on a spring gives adequate solution of the problem. Taking that into account, equation of motion of the probe can be written as [103, 104]:

$$m\ddot{z} + kz + \frac{m\omega_0}{Q}\dot{z} = F_{ts} + F_0\cos\omega t \qquad (2.2.2)$$

where Q is quality factor, k spring constant and ω_0 resonant frequency of a free spring. F_0 and ω are amplitude and frequency of a driving force. Stationary solution of a previous equation is in the form of

$$z(z_c, t) = z_0(z_c) + A(z_c)\cos[\omega t - \phi(z_c)] \qquad (2.2.3)$$

where z_0, A and ϕ are average deformation, amplitude and phase of oscillations, respectively, while z_c represents tip-surface distance without interactions and driving force. This solution however does not neglect nonlinear behaviour because they are implicitly included through dependence of amplitude, phase and z_0 on z_c. Through further deliberations, from virial theorem and additional approximations of small tip-surface interactions follows connection between driving frequency ω and oscillation amplitude A [103]:

$$\left(\frac{\omega}{\omega_0}\right)^2 = I + 1 - \frac{1}{2Q^2}\left[1 \pm \sqrt{1 + 4Q^2(\frac{A_0^2}{A^2} - 1 - I)}\right] \qquad (2.2.4)$$

where $A_0 = QF_0/k$ is free oscillation amplitude, while I keeps its dependence on F_{ts}:

$$I = \frac{2}{kA^2}\left(\frac{\langle F_{ts}\rangle^2}{k} - \langle F_{ts} \cdot z\rangle\right) \qquad (2.2.5)$$

where $\langle F_{ts}\rangle = \frac{1}{T}\oint F_{ts}\mathrm{d}t$, and $\langle F_{ts} \cdot z\rangle = \frac{1}{T}\oint F_{ts}z\mathrm{d}t$.

Although this result is not as simple form as the relation for the tunneling current (relation 2.2.4) it is general in a sense that it is valid for any form of the force $F_{ts}(z, z_c)$ because it states that surface properties influence steady state motion through mean

value of F_{ts}. Dependence on mean values is direct consequence of the periodicity of the oscillations. In the absence of the tip-surface interactions resonant curve becomes Lorentzian, a typical resonance curve of a driven harmonic oscillator (with dampening). Average value of F_{ts} is consequence of the competing attractive and repulsive interactions. Average force vanishes for the amplitudes smaller than z_c, with the increase of the amplitude tip is brought closer to the surface increasing the attractive interaction. With the further increase in the amplitude, repulsive component appears (in the moment of first mechanical contact between tip and the surface), and further increases until it predominates over attractive interactions. This kind of behaviour leaves its mark in the resonant curve of the cantilever, shown in figure 2.5b. Attractive interactions deform resonant curve by bending it toward the frequencies lower than resonant frequency, while repulsive stretch it toward higher frequencies. Combination of these effects generates two stable states in some specific frequency range. Regarding the time scales of the measurement, it should be noted that in AM-AFM amplitude changes are not instantaneous, rather, they happen on a timescale $\tau_{AM} \approx 2Q/f_0$ [102]. For the measurements under ambient conditions that is fast enough that it doesn't affect quality of the measurements. However, in the vacuum it becomes significant. Because of that, for the UHV measurements frequency modulated AFM (FM-AFM in short) is used more often. There are three possible ways of cantilever excitation: acoustic, magnetic and photothermal; and several different methods for cantilever deflection measurement. Most common of those (and one used for the measurements presented in this work) is optical method, using the laser beam reflecting from the upper side of the cantilever and whose deflection is registered on a detector (usually photodiode), as shown in figure 2.4a.

Moreover, like in the STM case, due to the nonzero tip radius, specific artifacts that give seemingly meaningful results can appear, while being result of a specific geometry of the tip apex. Due to the specific force dependence on distance, these effects are more prominent in the case of AFM. Additionaly, because of the fact that AFM directly feels intermolecular interactions, with the relatively simple changes or the upgrades (e.g. chemical functionalizations) of either the tip or the rest of the instrument, variations of the original technique were developed. These techniques enable measurements of the different surface properties in addition to the topography [105, 106], often simultaneously.

All AFM measurements presented in this work were carried out with Nanosurf FlexAFM in a dynamic force mode under ambient conditions. AppNano silicon tips with a nominal spring constant of 36-90 N/m, a tip radius less than 10 nm and a nominal resonant frequency of 160-225 kHz were used. Images were processed with

the Gwyddion software [89].

2.2.5 Quartz crystal microbalance with dissipation monitoring (QCM-D)

QCM-D is a thin film weighing and viscoelastic properties measuring device with submonolayer sensitivity that uses oscillation changes of a quartz sensor upon adsorption of a thin film [107, 108]. Basis of the apparatus is a single crystal quartz plate with metal (typically gold in our experiments) electrodes on both sides. Due to the piezoelectric properties of quartz, if sufficiently high AC voltage is applied an alternating expansion and contraction of the quartz crystal lattice is induced. When this driving frequency matches resonant frequency of the crystal a resonant condition occurs where wavelength of an induced standing wave is an odd integer of the thickness of the sensor. When additional mass is adsorbed on a sensor, resonance frequency shift occurs, and in the simplest case of a small rigid molecules distributed evenly over the sensor this change is related to the adsorbed mass via Sauerbrey relation [109]:

$$\Delta m = \frac{C}{n}\Delta f \tag{2.2.6}$$

where $n(= 1, 3, ...)$ is harmonic or overtone number and C reflects the mechanical properties of the sensor

$$C = \frac{t_q \rho_q}{f_0} \tag{2.2.7}$$

where t_q, ρ_q and f_0 represent thickness, density and resonant frequency of a sensor. In order for a relation 2.2.6 to be valid, three main conditions must be met. Mass of the adsorbed layer must be small compared to the mass of the sensor and the layer must be rigidly adsorbed and evenly distributed over the active area of a sensor.

However, when applying QCM-D to measurements in liquid some additional considerations should be taken into account because liquid can add additional contributions to the frequency change that are not considered in Sauerbrey relation. This contributions come from two different sources. First one stems from the fact that in a case of a very thick and/or viscoelastic film system becomes coupled oscillators for which Δf and Δm are no longer directly proportional. Second one is related to the fact that in liquid water molecules (or some other solvent molecules) can couple as an additional mass to the adsorbed film via direct hydration, viscous drag, or
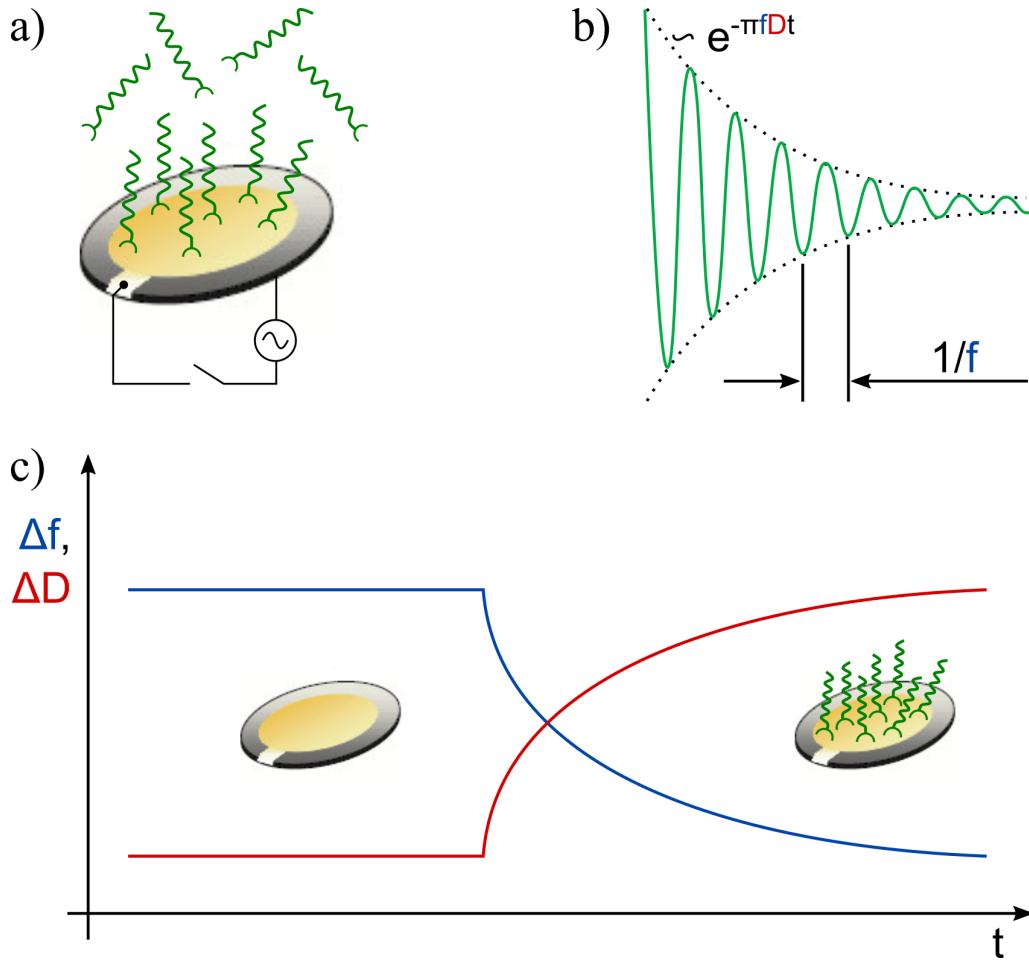
Figure 2.6: Schematic representation of QCM-D operation. a) QCM-D chip. b) Typical recorded signal during adsorption experiments from which Δf and ΔD are recorded. c) Representation of a typical curve obtained from simple adsorption experiment.

entrapment in cavities, making an effective layer of viscoelastic "hydrogel". This coupling can result in a measurements of an up to 4 times larger mass than the molar mass of the dry film. In order to take viscoelasticity of the adsorbed film into account its dissipation (D) should be monitored, which can be done in two ways. First one is to measure oscillation decay after a rapid excitation near the resonant frequency and the second one is impedance analysis. Our setup uses the first method, i.e. it measures output voltage amplitude (decay voltage) as a function of time. The signal is then fitted to an exponentially damped sinusoidal function $A(t)$ in the form of

$$A(t) = A_0 e^{-t/\tau} \sin(2\pi f t + \alpha) \tag{2.2.8}$$

where f is defined as $f = f_0 - fR$, with f_R being reference frequency. Dissipation,

a dimensionless parameter defined as

$$D = \frac{1}{Q} = \frac{E_{dissipated}}{2\pi E_{Stored}} \tag{2.2.9}$$

with Q representing the quality factor, can then be extracted from 2.2.8 as

$$D = \frac{1}{\pi f \tau} \tag{2.2.10}$$

During the measurement f and D are recorded for multiple harmonics of a resonant frequency ($n = 1, 3, 5, ...$) on the time scales of a milliseconds. This approach enables further modeling of the measurements to extract useful parameters like mass, thickness, density, viscosity, or storage modulus. Simplified representation of QCM-D operation is shown in figure 2.6.

QCM-D measurements were performed on Q-Sense E1 system (Biolin Scientific AB, Sweden) with QSX 301 Gold sensors (AT-cut, fundamental frequency 5 MHz, 100 nm gold coating, declared RMS roughness (0.9±0.2)nm).

2.2.6 Optical setup

Optical studies were conducted on the home-built optical setup based on confocal microscope in backscattered configuration that can be used for photoluminescence and Raman spectra measurements, whose schematic representation is shown in figure 2.7. Light from the semiconductor laser (Sapphire Coherent) with 532 nm (2.33 eV) excitation wavelength was focused to a spot with a diameter of less than a 2 μm on the sample by an objective lens ($\times$50; N.A.= 0.75). The excitation laser power was maintained sufficiently low to avoid damage to the sample. Collected backscattered light was guided to a spectrograph with focal length of f=303 mm and detected by a thermoelectrically cooled CCD through an optical fiber with a 50 μm core diameter, which acts as a confocal detection pinhole. Raman spectrometer with 300 and 1800 grooves/mm diffraction gratings were used to collect the photoluminescence and Raman spectra, respectively.
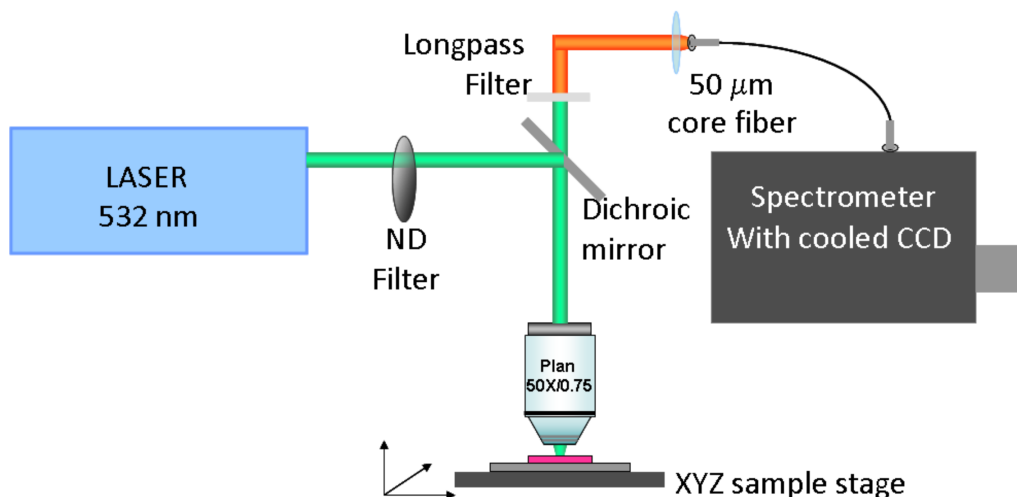
Figure 2.7: Schematic representation of optical setup used for PL and Raman measurements.

2.3 Theoretical simulations

2.3.1 Simulations of AuIr clusters

From the theoretical side, for the understanding of the AuIr cluster formation and their atomic structure molecular dynamics (MD) simulations [110] were used, since the formation of clusters is dynamical process. QuantumWise's Atomistix ToolKit code [111] was used for all simulations with dynamics of atoms modeled by Langevin equations of motion that set temperature of the system (canonical ensemble) via frictional and stochastic forces [112].

For investigation of the expected structure of cluster composed of Ir and Au atoms, ideal Ir and Au cluster were initially put close to each other. After relaxing the initial geometry MD simulations were performed with total integration time of 10-20 ps. Propagation step used was 1 fs and temperature of Langevin thermostat was set to 500-700 K. Although these temperatures are higher than in experiments, they are lower than melting temperatures and are used as a help to speed-up the dynamical processes of cluster formation. Using experimental temperatures would require much longer integration times that are not feasible (as the rates of dynamical processes are Arrhenius temperature dependent). At the end of each MD simulation, an additional relaxation was performed in order to obtain low temperature structure.

2.3.2 Simulations of MoS$_2$ on Ir(111)

Density Functional Theory (DFT) calculations were performed using the Vienna Ab initio Simulation Package (VASP) [113, 114]. VASP is a DFT-plane wave code that uses the pseudopotential approximation following the Projector Augmented Wave (PAW) approach [115]. To include the van der Waals interactions in the exchange-correlation potential [116] results for three different functionals were contrasted, namely the vdW-DF3 [117, 118], the optB86b-vdW and the optB88d-vdW [119]. Results from the last two did not differ and the optB86b-vdW was eventually employed during the simulations. The energy cutoff was set to 450 eV and the tolerance for ionic and electronic convergence to 0.01 eV/Å and 10^{-5} eV, respectively. For the density of states (DOS) calculations the sigma was set to 0.075. The STM images were simulated from the VASP converged results by means of the WSXM software [88], within the Tersoff-Hamann approximation.

Firstly, the isolated MoS$_2$ monolayer and bulk Ir systems were characterized. The optimized lattice constant and band gap value for the MoS$_2$ monolayer are 3.164 Å and 1.74 eV, in very good agreement with previous experimental [51, 120] and theoretical [121, 122, 123, 124, 125] reports. As for the Ir surface, a lattice constant of 2.73 Å was found, which is also in good agreement with previous experimental [126] and DFT [127, 128, 129] results. The Ir(111) surface was simulated by a 4 layers slab. To study the relative stability of the MoS$_2$ monolayer over the Ir substrate three different positions were investigated, with either the Mo atom, the S atom or the center of the hollow of the MoS$_2$ monolayer lying directly over the Ir atoms of the topmost layer of the metal slab. Only the two lower layers of the Ir slab were kept fixed during the relaxation process. The configuration where the Mo atoms lie directly over the Ir topmost atoms was the most stable one by 0.5 eV and was hence chosen as the initial geometry for our subsequent calculations. To minimize the strain due to the lattice mismatch between the MoS$_2$ and the Ir a 3×3 MoS$_2$ supercell over a 30° rotated $2\sqrt{3} \times 2\sqrt{3}$ Ir supercell was employed, doubling the cell for the study of the defected structures. This results in a tensile strain of 0.37% that was imposed solely on the metal.

The impact of several point-like defects in a MoS$_2$ monolayer deposited on a Ir(111) substrate was then studied by using a 6×6 supercell. The discretization of the first Brillouin zone was done by means of the Monkhorst-Pack scheme, using a grid of 5×5×1 special k-points for the relaxations and of 13×13×1 for the analysis of the electronic structure. A vacuum layer of 20 Å in the perpendicular direction of the slab was employed to avoid interaction between neighboring supercells.

CHAPTER 3

Biomacromolecules on flat gold surfaces

As a first step toward upgrading 2D material toward hybrid material, parameters for the adsorption of biomacromolecules should be optimized: like concentration and size of the biomacromolecules themselves, and also concentration of added salts, as well as pH, temperature and other parameters like ionic species. Since it was unpractical to explore these parameters using 2D materials, as their preparation is rather time consuming, a model surfaces had to be used, namely, flat gold surfaces of various types. Although gold is not as flat as for example mica or highly-oriented pyrolytic graphite (HOPG), which are commonly used substrates for SPM imaging, gold was used because attachment of biomacromolecules was intended via thiol bond (specific binding), not nonspecific binding that usually occurs on other types of substrates. Due to the nature of 2D materials used in our experiments, flat gold surfaces were most suitable.

3.1 Overview of gold substrates

Several different gold surfaces were used, which are depicted in figure 3.1a. For the QCM-D measurements commercially available chips were used, with the declared RMS roughness of 1 nm (gold substrate number 1 in figure 3.1a). This may seem like a low roughness, but if we take into account the size of used molecules, it's significant. Typical AFM image of the chip surface is shown in figure 3.1b, and the measured RMS roughness was 1.70 nm. In general, an RMS value translates to a peak-to-peak value which may be 6 to 8-fold larger than the RMS value for the studied region or section of the signal. Consequently, if the sensor's surface roughness amplitude is greater than the characteristic size of molecules or particles deposited on the surface for study then the said molecules or particles will be hidden by the features, the
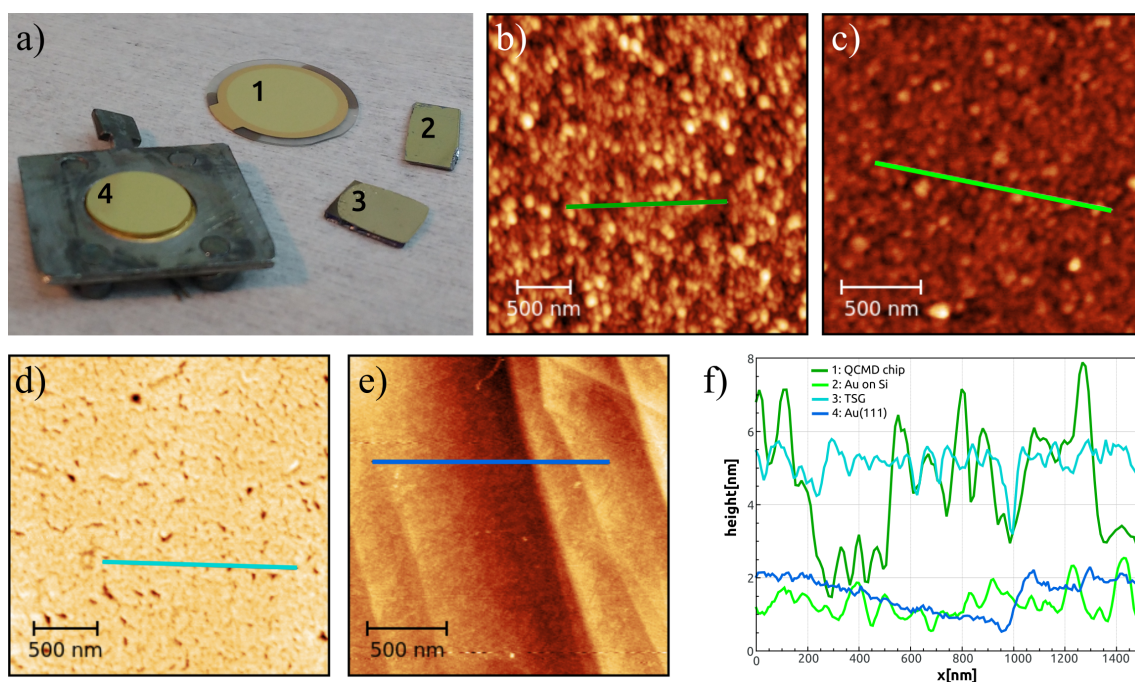
Figure 3.1: Surfaces tested for biomacromolecular adsorption. a) Picture of all four substrates: commercial QCM-D chip (1), thin layer of evaporated gold on SiO$_2$ wafer (2), TSG (3) and Au(111) monocrystal. b) Typical topography image of QCM-D chip. c) Typical topography image of gold layer on SiO$_2$. d) Typical topography image of TSG. e) Typical topography image of Au(111) surface. f) Comparison of profiles of all tested substrates.

valleys or troughs, of the sensor's surface. Thus, AFM images of the QCM-D chips showed no significant change in surface features after DNA deposition, meaning that the surface with lower roughness was needed to efficiently determine characteristics of the adsorbed layer with AFM. To achieve this, template stripped gold (TSG) surfaces were prepared with a following procedure. Thin gold film ($\approx$ 100 nm) is deposited on a SiO$_2$ wafer (gold substrate number 2 in figure 3.1a). This mid-step surface was also characterized with AFM, with typical topography image shown in figure 3.1c, and the obtained RMS roughness of 0.44 nm. Then, either clean piece of a wafer of a same type or a piece of freshly cleaved mica is glued to the surface of a gold covered wafer with epoxy glue. Before use, original wafer is carefully peeled of, leaving fresh, clean gold surface, which achieved RMS roughness down to 0.38 nm (gold substrate number 3 in figure 3.1a), whose typical AFM topography image is given in figure 3.1d. This procedure resulted in surface with lower roughness with relatively large flat domains separated with deep cracks, possibly as a result of peeling procedure. To overcome this, a procedure including chemical cleavage with tetrahydrofuran (THF) could be used [130], or the additional flame annealing after the surface preparation. However, due to the concerns that these procedures may

leave surfaces contaminated, we decided to use Au(111) single crystal sample (gold substrate number 4 in figure 3.1a), prepared before use in a UHV chamber with a previously described procedure (subsection 2.1.1). As shown in figure 3.1e, this is the surface with the highest structural quality of all tested substrates, with atomically flat terraces of several hundred nanometers in width. Comparison of profiles of all tested substrates is shown in figure 3.1f.

3.2 DNA tetrahedra adsorption

3.2.1 QCM-D adsorption monitoring

QCM-D was used for a quantitative measurement of specific adsorption of disulphide functionalized DNA on gold, as it can precisely measure attached amounts. Experiment run as following: first the blank buffer (without dissolved DNA, as specified in 2.2.3.) was run through the QCM-D system until equilibrium was reached (usually 1 hour). Then, the same buffer but with dissolved biomacromolecules was introduced into the system, until it fully replaced the blank buffer (2-3 minutes). This solution was was left to cycle until adsorption slowed down significantly. To remove all of the unspecifically adsorbed molecules EtOH:H_2O 1:1 mixture was introduced in the system until signal stabilized again, and then the same was repeated with deionized water. Afterwards, blank buffer was introduced again and the run was finished after the final signal stabilization, with the typical run shown in figure 3.2. From difference in Δf between first and last step in equilibrium, total specifically adsorbed mass can be calculated, and from that, density of molecules per unit area. Frequency measurements with a resolution of 1:10^{-10} in a one second interval are easily made, thus deposited mass can be measured even below 1 ng/cm^2 - that is, the deposition of less than a monolayer of molecules or particles may be detected. For the testing of adsorption parameters dsDNA with 120 bp length and disulphide group on one end was used, as it is readily available in comparison to DNA tetrahedra.

3.2.2 SPM characterization

Tetrahedra adsorbed on Au(111) crystal surface was imaged with AFM in ambient conditions and subsequently with STM in UHV. The AFM images of a surface after incubation procedure described previously (subsection 2.2.3) show significant difference from clean Au(111) surface, with deposited layer clearly visible (figure 3.3a-c). Molecules don't form full layer, but seem to form disordered network or a mesh that spreads continuously over monoatomic steps. Due to size of the AFM
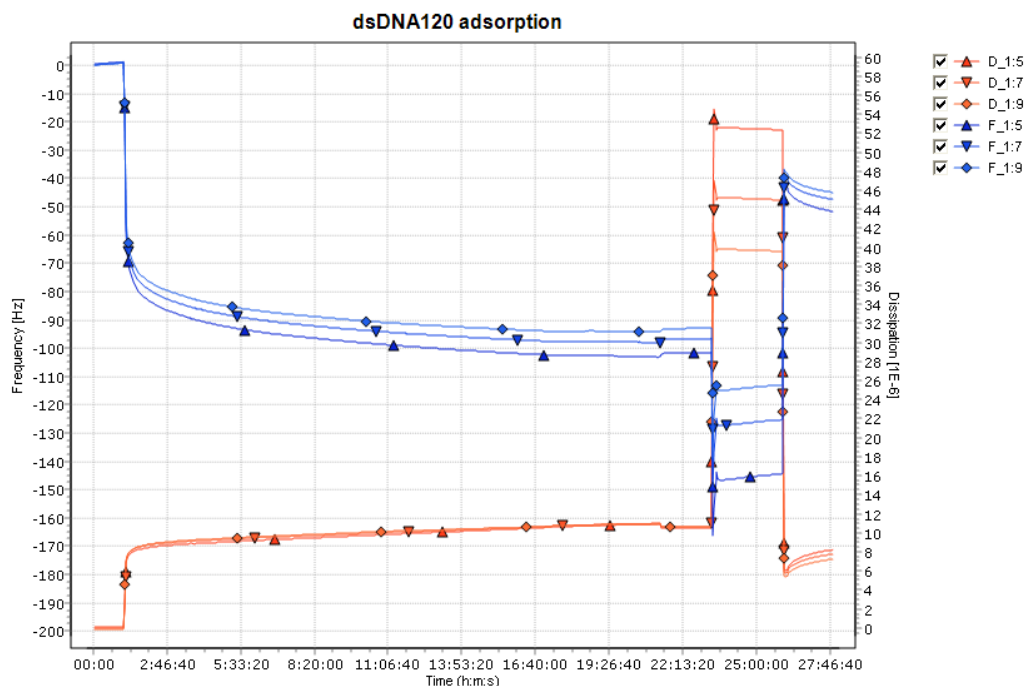
Figure 3.2: Example of a dsDNA adsorpion measurement with QCM-D.

tip whose radius is 3-10 nm which is in the range of the tetrahedra size (cca 5 nm edge length), single DNA tetrahedra couldn't be resolved with AFM imaging, but the height of the layer of 3-4 nm corresponds to expected tetrahedron height.

STM imaging in UHV reveals further details inside the mesh. While separate shapes roughly 5 nm in size are clearly discernible (figure 3.3d-f) they do not form ordered array, but are instead adsorbed randomly on the surface. This is not surprising due to the uniformity of the substrate and lack of any additional constraints that would initiate ordered assembly. Shape of the adsorbed biomacromolecules is distorted due to the fact that tetrahedra size and height are comparable to the tip apex size resulting in the possibility of enhanced tip-sample convolution and also because of the usual difficulties that arise from the imaging of the biomacromolecular layer with STM [131].

Moreover, due to the different surface properties of Au(111) compared to other substrates used in this work the optimal parameters for imaging on Au(111) will not correspond to the optimal parameters for other substrates. Same goes for the adsorption density, especially compared to MoS$_2$.
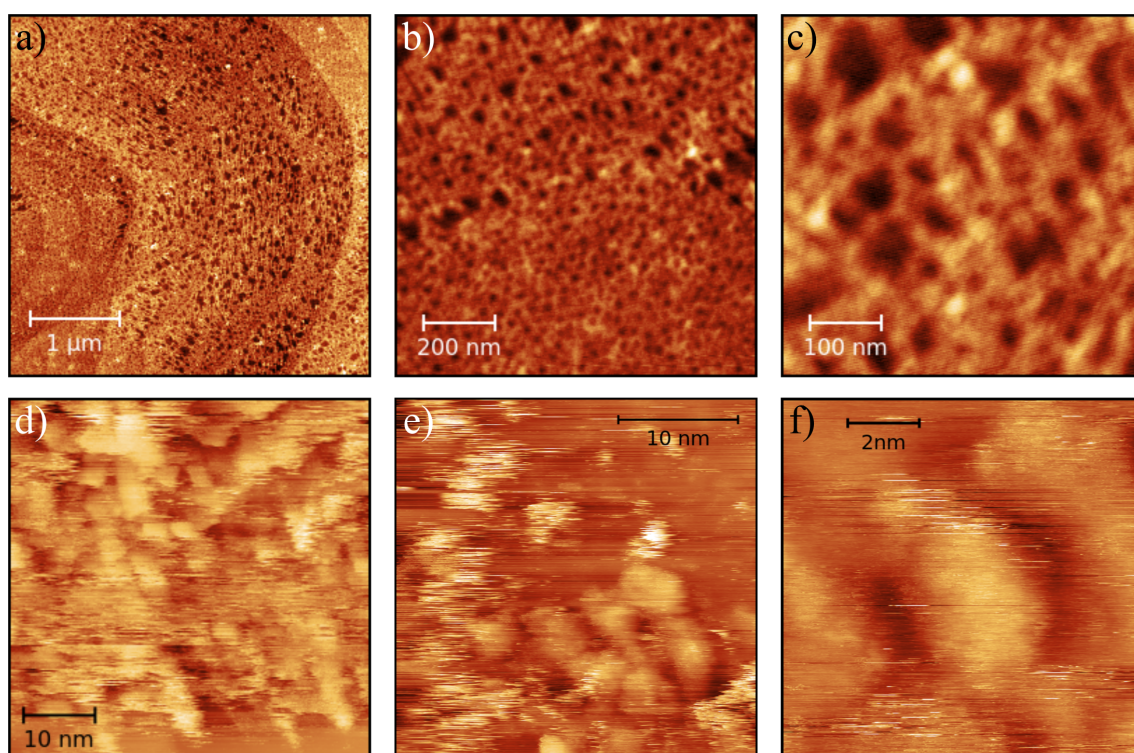
Figure 3.3: Au(111) surface after DNA tetrahedra adsorption. a)-c) AFM images of the sample imaged in ambient conditions. d)-f) Same sample imaged with STM in UHV conditions.

Metallic clusters and biomacromolecules on graphene

4.1 Metallic clusters growth

In order to achieve specific binding of DNA to graphene via thiol bond, graphene should be functionalized in advance for DNA functionalization. This can be realized via array of golden nanoclusters. In ordered to achieve highly ordered array, moiré superperiodicity of graphene on Ir(111) can be exploited as a template for the metallic cluster growth [42]. Moiré pattern is very suitable for the formation of ordered metallic cluster array, as many metals will upon evaporation readily form a lattice of clusters which follows a moire pattern beneath it. For those metals submonolayer coverage will result in a fairly monodisperse clusters, with maximum of one cluster per moiré cell. Clusters will never form on the atop regions of the moiré cell, and they prefer hcp to fcc region [41]. Once such cluster lattice is formed, characterization can be done in situ using STM and LEED. During STM characterization imaging parameters need to be carefully tuned, because not only does moiré contrast vary with their change (as shown in figure 4.1a), but also clusters can become transparent for certain range of parameters. For the cluster coverages close to full, for most of the tested metals either clusters or the moiré can be visualized, not both, for any chosen parameters. The exception were vanadium clusters, an example of what is shown in figure 4.1b. However, in a case of lower cluster coverages, both can be discerned for all tried metals, so lower dosages were used first to confirm formation of clusters. For the evaporation on sample at temperatures lower than room temperature cluster formation on fcc regions becomes more frequent and clusters grow larger (an example shown in figure 4.1c, where evaporation was done with sample at 0°C), so this should be avoided in order to obtain hexagonally ordered array.

From the tested metals, vanadium, molybdenum, tungsten and iridium all formed
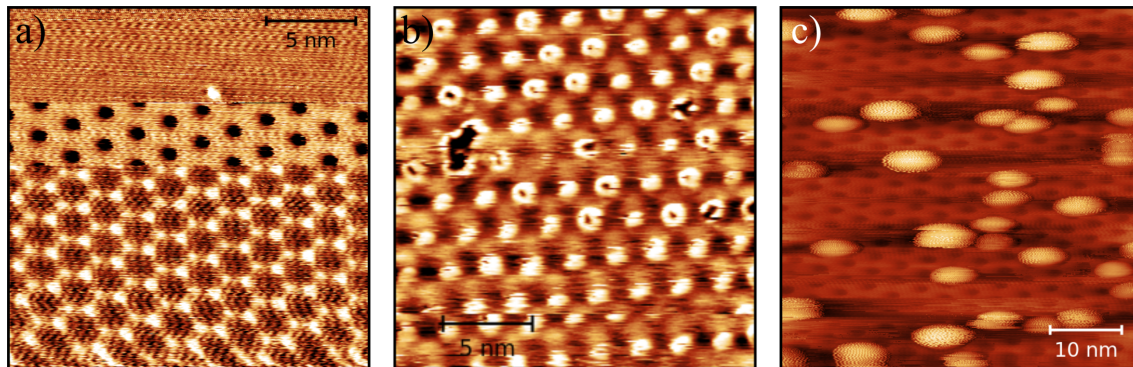
Figure 4.1: a) Changes in graphene moiré contrast with changes in imaging parameters. b) Vanadium clusters on graphene moiré. c) AuIr clusters formed after evaporation on on graphene on Ir(111) with sample at 0°C, resulting in larger cluster size. Besides being formed on hcp regions of the moiré, some also formed on fcc regions, resulting in a seemingly disordered lattice.

ordered clusters, while gold did not (as expected from previous report [42]). Gold formed large disordered polidisperse lumps, that prefer forming on domain boundaries (analogous to W on graphene domains differing from R0, as reported in [132]). So, in order to obtain clusters with gold, first another metal needs to form smaller clusters to serve as seed for gold adsorption. V, Mo, W proved not suitable for seeding, as gold formed disordered large clusters independently from ordered metallic clusters and formed clumps the same as without metal pre-deposition. However, gold did attach to iridium seed clusters, thus forming bimetallic AuIr clusters, as shown in figure 4.2a. Confirmation of the formation of bimetallic clusters comes from two facts: clusters increased in size (as shown in figure 4.2b) and polydisperse gold lumps were not present after Au deposition. Additionally, for higher cluster coverages, formation of ordered cluster array can be confirmed already with LEED as the every other spot in the diffraction pattern disappears for certain energies (figures 4.2c and d).

It should be added that at graphene domain boundaries larger Au clusters persisted, so only graphene of an excellent quality is a suitable platform for long-range ordered array of clusters formation i.e. formation of a nanotemplate. In that case limit to the size of an array domain comes from graphene wrinkles [133] which can't be eliminated with the utilized graphene preparation methods.
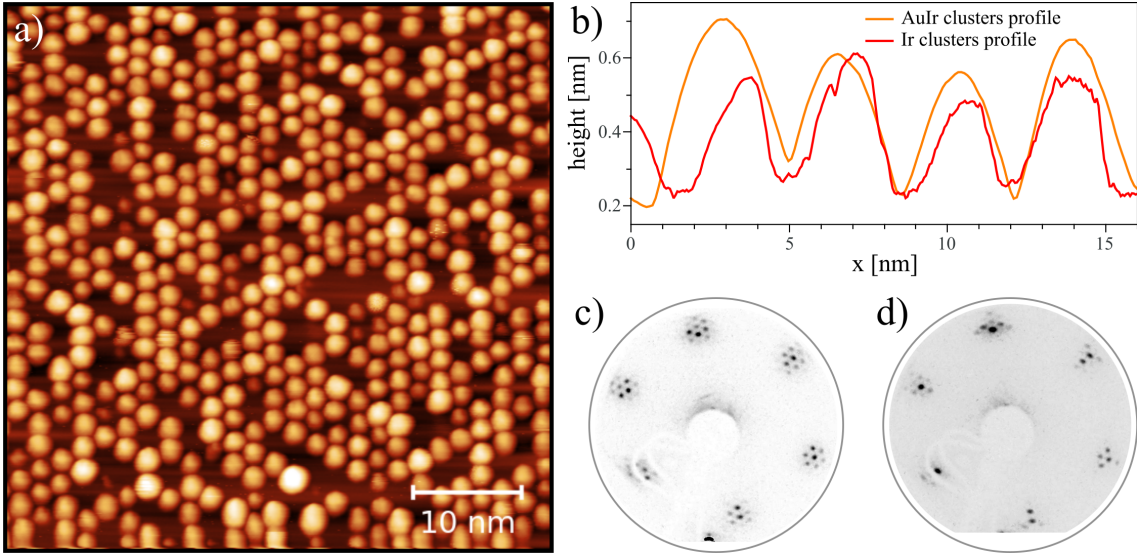
Figure 4.2: a) Aray of AuIr nanoclusters formed on graphene moiré. b) Comparison of cluster profiles before and after gold evaporation on previously synthesized iridium clusters. c) LEED pattern of a graphene on Ir(111) at E=76eV. d) LEED patten of a graphene on Ir(111) after AuIr cluster formation at E=76eV.

4.2 AuIr seeded cluster array

4.2.1 Structure

As previously mentioned, depending on imaging parameters contrast changes between moiré and clusters, only one of the subsystems is visible at the time. In a case of lower cluster coverages, both can be discerned. However, for subsequent biomacromolecules deposition high coverages are needed, so amounts of deposited Ir and Au were slowly increased until optimal coverage was obtained. Since height profiles determined from STM scans are not "real" heights, but heights in a sense of LDOS, average number of atoms per cluster $\bar{s}$ is more accurately determined from surface coverage Θ [40]:

$$\bar{s} = \frac{A_m \Theta}{n} \tag{4.2.1}$$

where A_m represents size of a moiré cell and n is cluster density defined as number of clusters per moiré cell. For graphene on Ir(111) $A_m = (87 \pm 3)$, and Θ is determined by deposition of the same amount of metal (gold and iridium, but in separate experiments) on the flat Ir(111) surface. Both metals, upon evaporation, form well defined monolayer islands, so coverage of the surface is easily determined from STM images of the surface. For the parameters used to form AuIr clusters $\Theta(Ir) = 0.1$

and $\Theta(Au) = 0.15$, so with $n = 1$ for full coverage average numbers of atoms per cluster are $\bar{s}(Ir) = 9$ and $\bar{s}(Au) = 13$.

To gain the insight into structure of clusters at atomic level, theoretical investigation through MD simulations was conducted as well. Ideally, the so-called *ab initio* MD simulations in which forces are obtained from density functional theory would be used but simulating the full system during typical formation time with this method is far beyond available computational power. Alternatively, one could use interatomic potential which is fast to evaluate, but unfortunately, there are no accurate potentials that are fitted to system containing at the same time Ir, Au, and C atoms. However, if the restriction is made to only Ir and Au atoms, such potentials exist [134, 135, 136], and they give rather good description of metallic clusters [137]. Therefore, the dynamics of formation of AuIr clusters was studied without explicit inclusion of the surface, with the technical details of the MD simulations described in subsection 2.3.1.

Several runs were performed with different initial structures and temperatures that lead to the same conclusion, while two examples with different initial Au cluster structures are elaborated in more detail in the following. Figure 4.3 shows results for two icosahedral clusters with 13 atoms each. Structure used in this example is the most stable geometry for the metallic clusters of around 10 atoms. Left panel of the figure shows optimized Ir_{13}/Au_{13} structure. As can be seen in the middle panels of the figure (which show structure at the last step of dynamics), Ir atoms are strongly bound to each other and the structure of initial Ir cluster during the dynamics does not distort much. Au atoms however are less strongly bound and their initial structure is destroyed. When the final relaxation is performed (cooling toward T=0 K or in the last case T=700 K) obtained structures contain some Au atoms that are bound only to the Ir cluster. This implies that expected final structure is Ir core / Au shell structure. The fact that Ir atoms are more strongly bound than Au atoms stems from the almost twice larger cohesive energy of Ir compared to Au. Figure 4.4 shows the case when initial gold cluster is of fullerene type with 16 atoms, and the configurations at the end of the simulation resemble the previous case. These results therefore show that the core-shell structure for Ir/Au clusters is highly expected, as opposed to a mixed phase.

4.2.2 Stability

Further use of such a nanotemplate for biomacromolecular adsorption necessitates testing its stability under variety of conditions. Initially we observed that AuIr

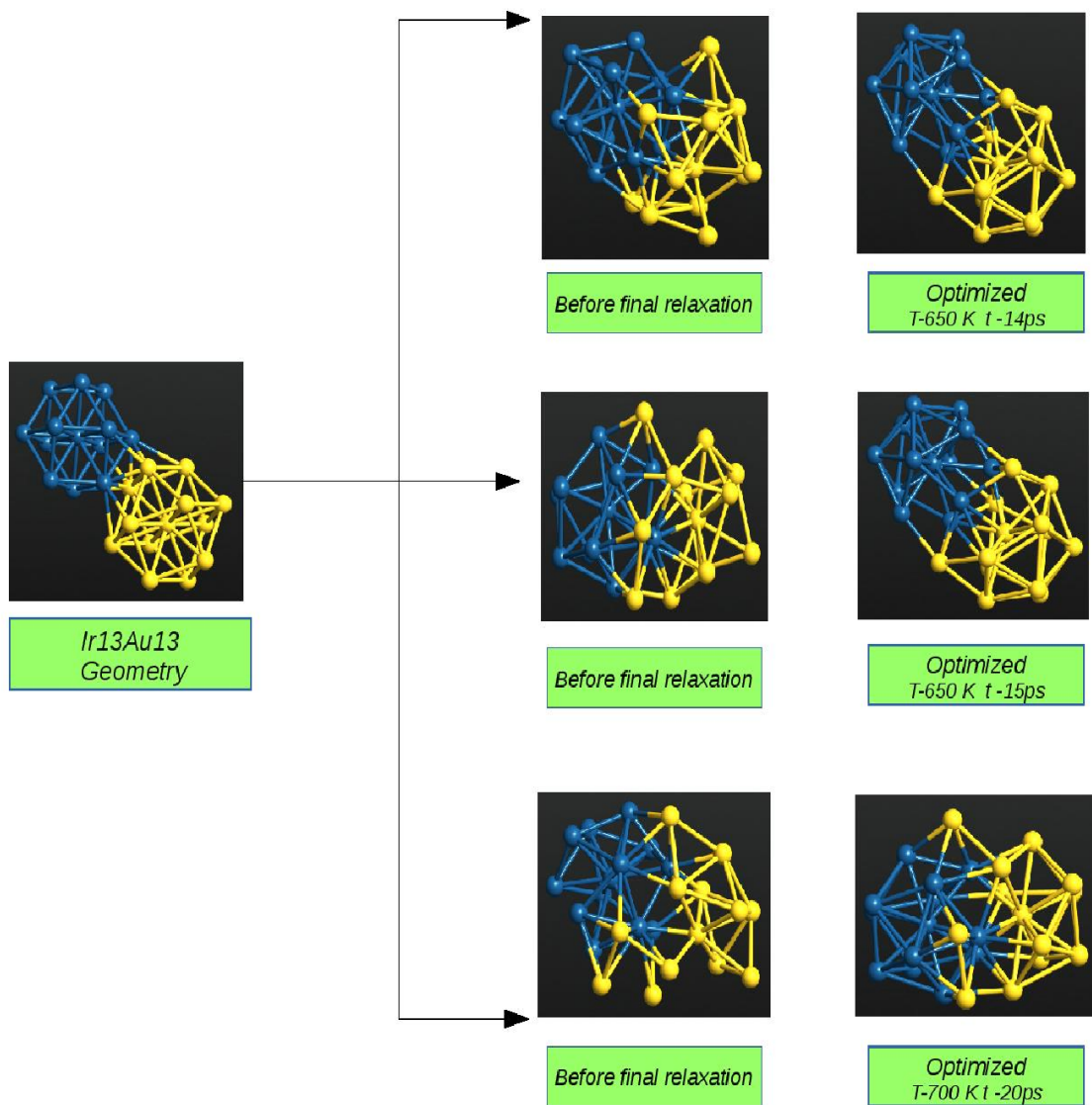**Figure 4.3:** Ir$_{13}$/Au$_{13}$. Left panel: Initially optimized geometry. Middle panel: Positions at last step of dynamics. Right panel: Optimized geometry after molecular dynamics run.
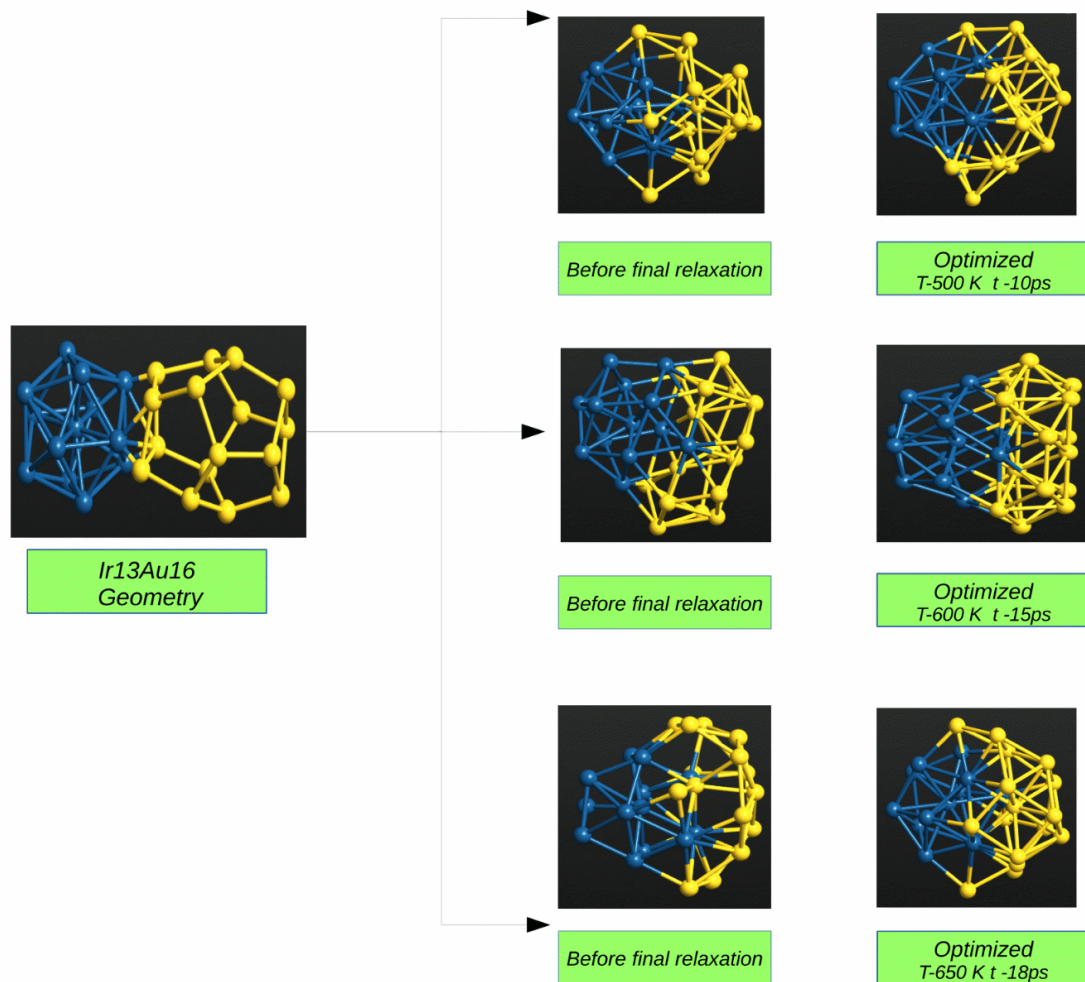
Figure 4.4: Ir_{13}/Au_{16}. Initially optimized geometry. Middle panel: Positions at last step of dynamics. Right panel: Optimized geometry after molecular dynamics run.

clusters exhibit lower tolerance on removal upon STM imaging, than purely Ir clusters [138]. It is known from previous reports [139] that clusters are easily picked from the graphene with the STM tip, but the parameters to do so are too extreme for imaging. For the AuIr clusters, it is possible to remove them from graphene with commonly used imaging parameters (namely, for V_b=0.4V and I_t=1.3nA), which implies that after gold deposition clusters become less strongly bound. Parameters for cluster imaging were usually around V_b=1.4V and I_t=0.4nA, with typical image shown in figure 4.5a. Upon zoom-in on a smaller area and subsequent imaging (around 10 images) with previously mentioned parameters for cluster removal, all the clusters from that area were removed. Interesting to note is the fact that after removal of the clusters, moiré becomes visible again (in the area where clusters were removed, with the parameters used for cluster removal). When the scan range is enlarged, area where clusters were removed is clearly visible (figure 4.5b). Slight distortion of the square is due to thermal drift. It is interesting to note that the clusters were not just swept away, they would appear at the edges of the cleaned area in that case, but were picked up by STM tip. This type of easy cluster manipulation opens opportunities for additional tailoring of such nanotemplates.

Furthermore, stability to conditions out of UHV were tested [138]. Imaging of a sample one week after it was removed from the UHV chamber and held at ambient conditions proved that cluster array survives such conditions. Also, when imaged with AFM that sample didn't show presence of the intercalated areas which were usually present on a graphene on Ir(111) samples exposed to air, that can probably be attributed to spontaneous intercalation from air. Additionally sample was washed with deionized water what didn't influence the array, and previous reports have shown that such nanopaterns are resistant to washing with isopropanole [140], which indicated that DNA tetrahedra deposition should not remove the array.

As a first step towards applicability, we planned to perform lift-off and transfer of the AuIr nanocluster array together with graphene. To realize transfer of a complete graphene layer, Cs intercalation is usually performed as first step. Upon intercalation of Cs nanopattern lattice disordering occurred [138]: 1ML intercalation results in unpinning of AuIr clusters and their consequently increased mobility which leads to lattice disorder. This is confirmed both with STM and LEED: in a LEED diffraction pattern moiré spots completely vanished while $(\sqrt{3} \times \sqrt{3})$R30° structure of intercalated Cs becomes clearly visible [141]. STM images shown in figures 4.5d and e show that clusters are still present on the surface of the intercalated graphene, but all of the hexagonal ordering have disappeared. On the areas where intercalation didn't occur (visible in figure 4.5d) ordered cluster array is still present. Intercalation
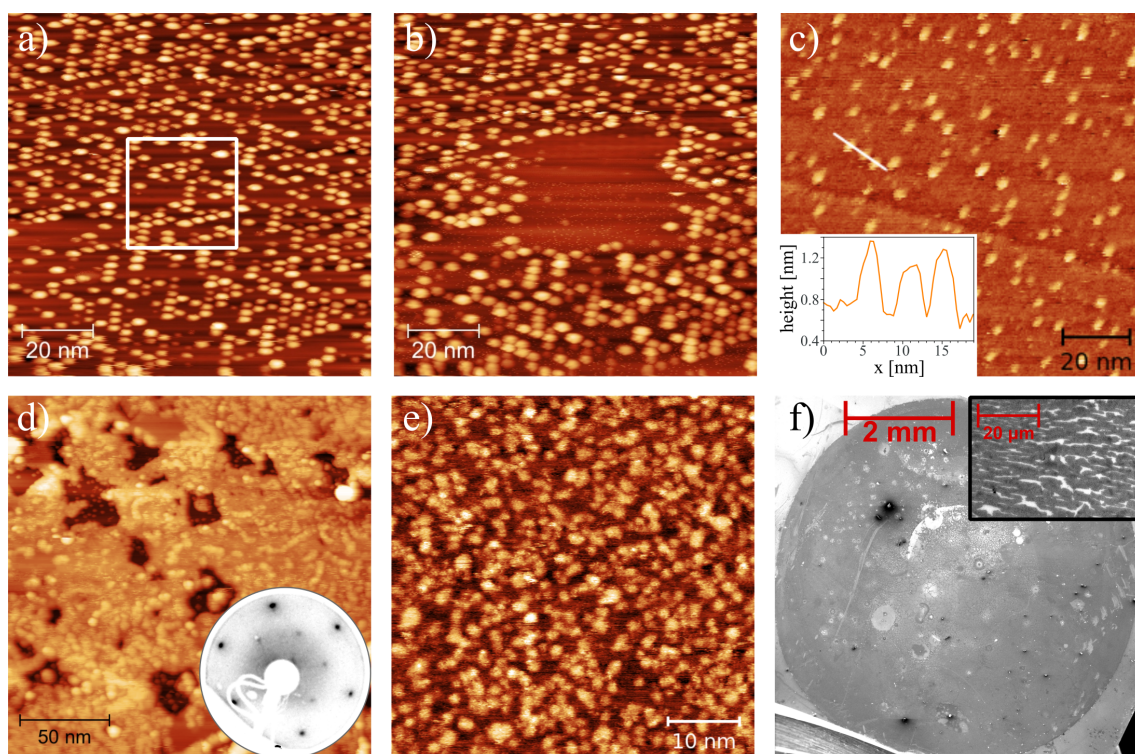
Figure 4.5: a) Typical STM image of AuIr cluster lattice on graphene (V_b=1.4V and I_t=0.4nA). b) Same area shown in a) after cluster removal (done with V_b=1.4V and I_t=0.4nA), imaged with same parameters. c) AuIr cluster lattice of small coverage after one week in ambient conditions, imaged with ambient STM. Inset shows profile marked in the image. d) STM image of a nanopattern after intercalation of 1ML of Cs: clusters disorder upon intercalation. Inset shows LEED image of the sample at E=76 eV with $(\sqrt{3} \times \sqrt{3})$R30° structure of intercalated Cs clearly visible. e) STM image of an intercalated area after Cs intercalation showing aparent disorder in cluster lattice. f) SEM image of a graphene transfered to SiO$_2$ substrate.

with Li had similar results (images not shown).

Several routes were tried out to overcome this, and in the end successful transfer of the graphene to SiO$_2$ without previous intercalation in UHV was realized, according to procedure described in subsection 2.2.1. SEM images of a sample proved that majority of the graphene have survived the transfer (figure 4.5f), but GISAXS measurements of a sample showed that clusters were all removed from the graphene during the transfer [142].

4.3 DNA tetrahedra adsorption

Due to the fact that clusters detach from the graphene upon lift-off and transfer, adsorption of biomacromolecules to the nanotemplate could be achieved only

on the as-synthesized samples still on Ir(111). DNA tetrahedra adsorption on the nanotemplate was conducted according to the previously described incubation protocol (subsection 2.2.3), immediately after the sample was taken out of load-lock, to prevent additional adsorbates from air as much as possible. After incubation sample was immediately returned to load-lock, and imaged with UHV-STM afterward. Eventually, the sample was taken out of the chamber and imaged with AFM under ambient conditions.
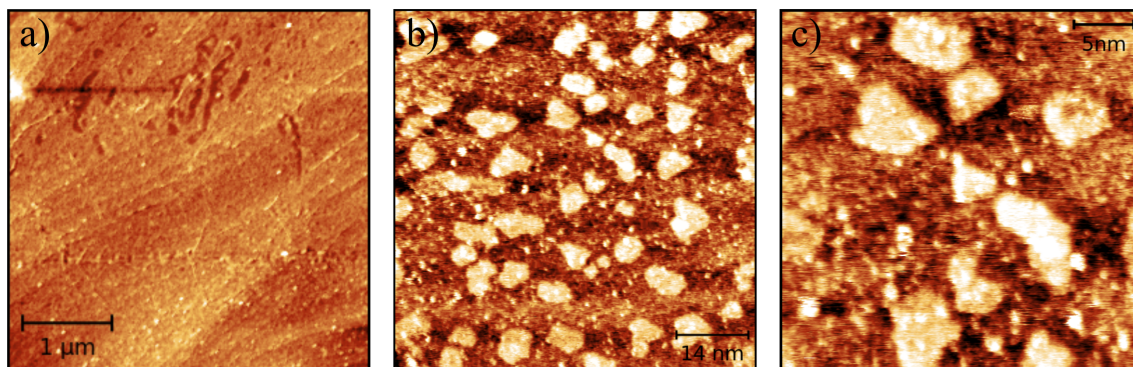

Figure 4.6: a) AFM image of the adsorbed DNA tetrahedra layer on AuIr clusters on graphene on Ir(111). b)&c) Same sample imaged with STM in UHV.

AFM images show adsorbed layer of similar height and features as the one formed on Au(111), as shown in figure 4.6a. As before, molecules don't form full layer as there are occasional holes in it, but overall layer appears more dense. Again, due to size of the AFM tip whose radius is 3-10 nm which is in the range of the tetrahedra size (cca 5 nm edge length), single DNA tetrahedra couldn't be resolved with AFM imaging.

With the STM, separate molecules can be discerned. However, imaging parameters that proved to be suitable for the imaging of DNA tetrahedra were ones usually used for cluster removal, so during the imaging most of the clusters on the area not covered with tetrahedra were removed. Two typical STM images are shown in figure 4.6b and c. Although they form relatively dense layer, coverage is not complete and molecules do not form orderly assembled layer. Most of them do not exhibit tetrahedral shape, with few exceptions, which probably means that they have either aggregated or were partially destroyed during STM imaging.

Since this nanotemplate is only stable while kept on the single crystal on which it was synthesized, it is not suitable for further applications. However, as a template it can be used to study assembly upon adsorption of different kinds of biomacromolecules functionalized with linkers which can form thiol bonds.

CHAPTER 5

Biomacromolecules on MoS$_2$ monolayer

5.1 Macroscopic structure and transfer of monolayer MoS$_2$

MoS$_2$ monolayer was grown on 300 nm SiO$_2$/Si substrates by CVD growth according to procedures described in subsection 2.2.2. The parameters of the synthesis of samples investigated in this work were adapted to ensure homogeneous monolayer growth over a millimeter large scales without significant amount of bi- or multilayers. While on the edges of the sample there were parts with still separate flakes with saw-like edges (as opposed to usual straight edges whose growth in our case resulted with significant amount of multilayer growth in the middle sections of the flakes), most of the other area (millimeter scales) was covered only with the monolayer, exhibiting almost insignificant presence of bilayer flakes. The as-grown samples were inspected with optical microscopy (figure 5.1a), SEM (figure 5.1b& d) and AFM (5.2). SEM and AFM imaging show the same features: uncoalesced flakes exhibit irregular edges, with occasional 5-10 nm tall wrinkles across the sample (on length scales of several to hundreds of micrometers) and some scarce adsorbates, mostly on the edges of the flakes [143].

For further experiments leading to potential future applications, efficient sample transfer procedure (without significant loss and with as few additionally produced defects as possible) is necessary. Transfer procedure via PDMS stamp used in this work is a method which was already successfully applied for the transfer of atomically thin layers between wide range of different substrates [95, 96, 97]. Our focus was on transfer of monolayer MoS$_2$ from the SiO$_2$/Si growth substrate to: (i) single-crystal Ir(111) surface or (ii) clean SiO$_2$/Si substrates. While the latter
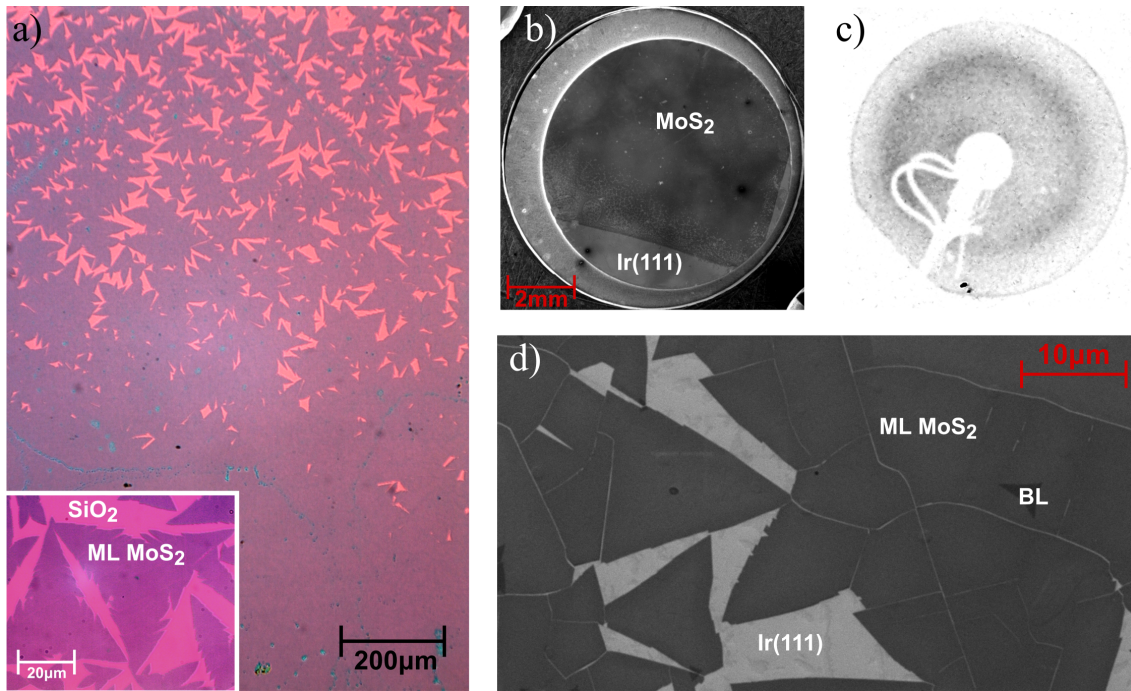
Figure 5.1: a) As grown monolayer MoS$_2$ on SiO$_2$ substrate imaged with optical microscope. Inset shows zoom-in on a area with separate flakes, which exhibit saw-like edges. b) SEM image of a whole sample surface of monolayer MoS$_2$ after transfer to Ir(111) monocrystal. c) LEED pattern of monolayer MoS$_2$ on Ir(111) at E=71eV. d) SEM image of transfered monolayer MoS$_2$ on Ir(111) with visible cracks on the domain boundaries.

route was used as a way to confirm the strain release upon lift-off from the growth substrate and can be considered as an initial step in preparation of high quality devices from individual CVD monolayers or stacked ones into heterostructures on a dielectric support, the former route enabled a non-destructive characterization of atomic-scale defects and local electronic properties with STM and STS, methods requiring conductive substrate as opposed to usual TEM characterization which introduces additional defects during imaging [144, 145, 146, 147]. MoS$_2$ layer was systematically examined during every step of the transfer process with AFM, SEM, optical microscopy and optical characterization (PL and Raman spectroscopy), to precisely determine when macroscopic irregularities such as cracks and wrinkles may appear during transfer.

Imaging on a large scale with optical microscope and SEM (figure 5.1b) confirms successful uniform transfer of a large-scale monolayer to both substrates. Although monolayer area extends over millimeter distances, the crystallographic orientation of MoS$_2$ randomly varies across the sample due to anisotropic growth (caused by the heterogeneous nucleation and growth of randomly oriented single-crystal flakes

on SiO$_2$ substrate). This was also subsequently confirmed with low energy electron diffraction (LEED), showing a circular intensity from all possible rotations of MoS$_2$ on Ir(111) shown in figure 5.1c. Zoom-in to micrometer scales with SEM (figure 5.1d) showed almost complete transfer, with small uncovered areas and/or negligible amount of bilayers. On micrometer scale, the layer shows presence of wrinkles or cracks every several micrometers, a known effect that is related to a local strain imposed by the growth at elevated temperatures or by subsequent mechanical manipulation. Samples indicated high uniformity on the nanometer-scale and proved suitable for characterization with STM.

AFM images of the as-grown samples are in accordance with SEM images [143]: flakes exhibit saw-like edges, with occasional wrinkles (on a scale of tens to hundreds of micrometers) and some scarce adsorbates, mostly on the edges of the flakes (figure 5.2a-c). AFM phase images give nice contrast between MoS$_2$ layer and substrate (for all explored substrates), as shown in figure 5.2c&e.
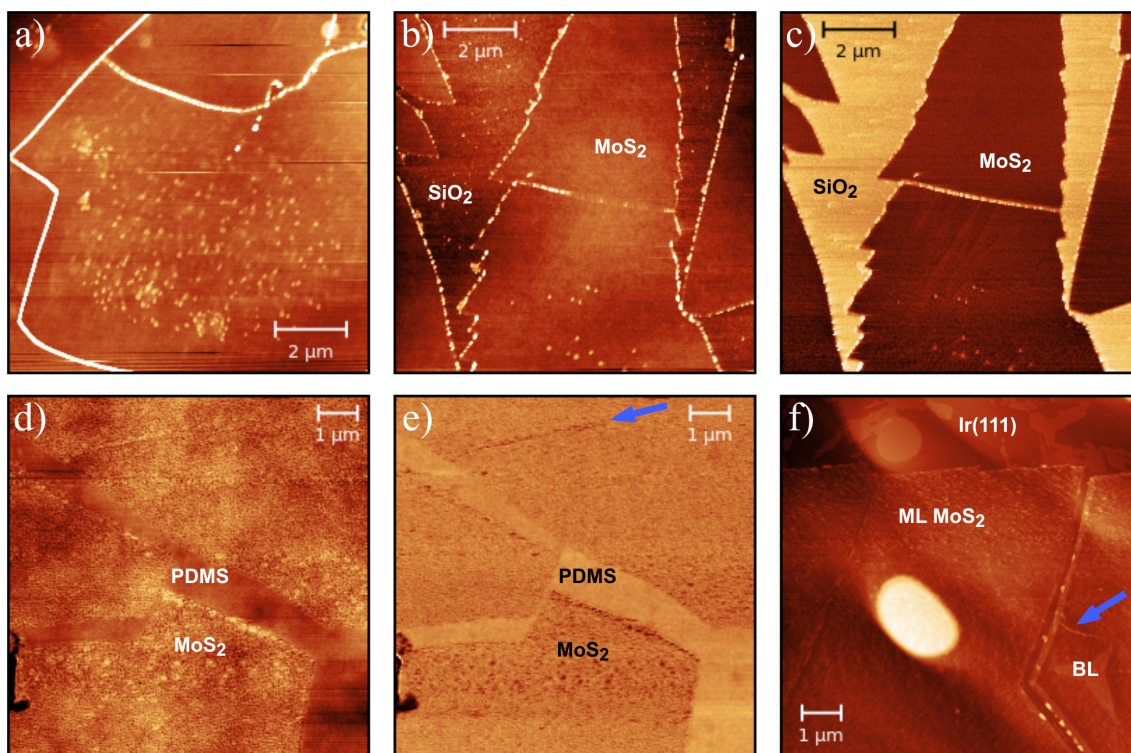
Figure 5.2: a)&b) Typical AFM topography images of the as grown MoS$_2$ monolayer on SiO$_2$ substrate. c) Phase image of an area shown in b). d) Typical AFM image of MoS$_2$ monolayer on PDMS. e) Phase image of an area shown in d). f) Typical AFM image of MoS$_2$ monolayer after transfer to Ir(111).

During transfer, already on PDMS, cracks and wrinkles appear. Cracks with submicrometer lateral scale form on the edges of grain boundaries (which were

visible already in SEM and optical microscope, and in AFM appear as wrinkles for whom is assumed that probably occur as boundaries of two growing domains close up and overlap in the process). Additional small wrinkles (indicated by blue arrows in figures 5.2e&f) sometimes appear on the flake edges, which are assumed to be a consequence of the lift-off mechanism. Image of a typical area on PDMS is shown in figure 5.2d&e. After the completion of the transfer, AFM images (with a typical one shown in figure 5.2f) of MoS$_2$ on Ir(111) show that edges along the cracks sometimes get folded (overturned). Also, some additional adsorbates are visible on Ir(111) close to the edges of the MoS$_2$ layer.

5.2 Microscopic structure and defects after transfer to Ir(111)

For STM characterization, samples transferred from the growth substrate to Ir(111) were readily inserted into a load-lock system of the ultra high vacuum (UHV) setup and quickly pumped down and baked at 400K for 10-12 hours before insertion into UHV. In the UHV system, samples were preliminary inspected by LEED as mentioned previously and extensively characterized with STM&STS. In specific cases, when STM imaging included area of MoS$_2$ flake edges, a dynamical ripping or flipping of flake edges during imaging often occurred (even though imaging parameters were rather conventional: V=500m I=1.3nA), as shown in figure 5.3a and indicated with blue arrow. This indicates relatively weak bonding character of MoS$_2$ overlayer and a metal substrate. In areas away from the MoS$_2$ edges, STM imaging is very stable in the whole range of applied imaging parameters. Set of STM topographs regarding large-scale imaging is presented in figure 5.3b. The characteristic feature clearly visible over all scan ranges in figures 5.3b-e regard a long-range corrugation at characteristic length scales of the order of 5-10 nm. The amplitude of this corrugation varies in the range 0.2-2 nm. Specifically height variation in figure 5.3e is 0.5 nm. Rippling of the 2D layer evokes some similarities to a well-known moiré effect typical for epitaxial systems. For comparison, in figure 5.3f an STM image of moiré structure of graphene on Ir(111) is shown. The distinction between perfectly periodic moiré structure of graphene and a nonperiodic long-range corrugation of the MoS$_2$ overlayer is however pronounced and the nanoscale rippling of the MoS$_2$ overlayer can be more directly compared to STM topography of single-layer graphene on SiO$_2$/Si surface [148, 149]. Similar corrugations were also observed on epitaxial MoS$_2$ on graphene [150], with the band gap size and position very similar to our results, as discussed in a next subsection. Corrugations in our samples could be attributed to interaction
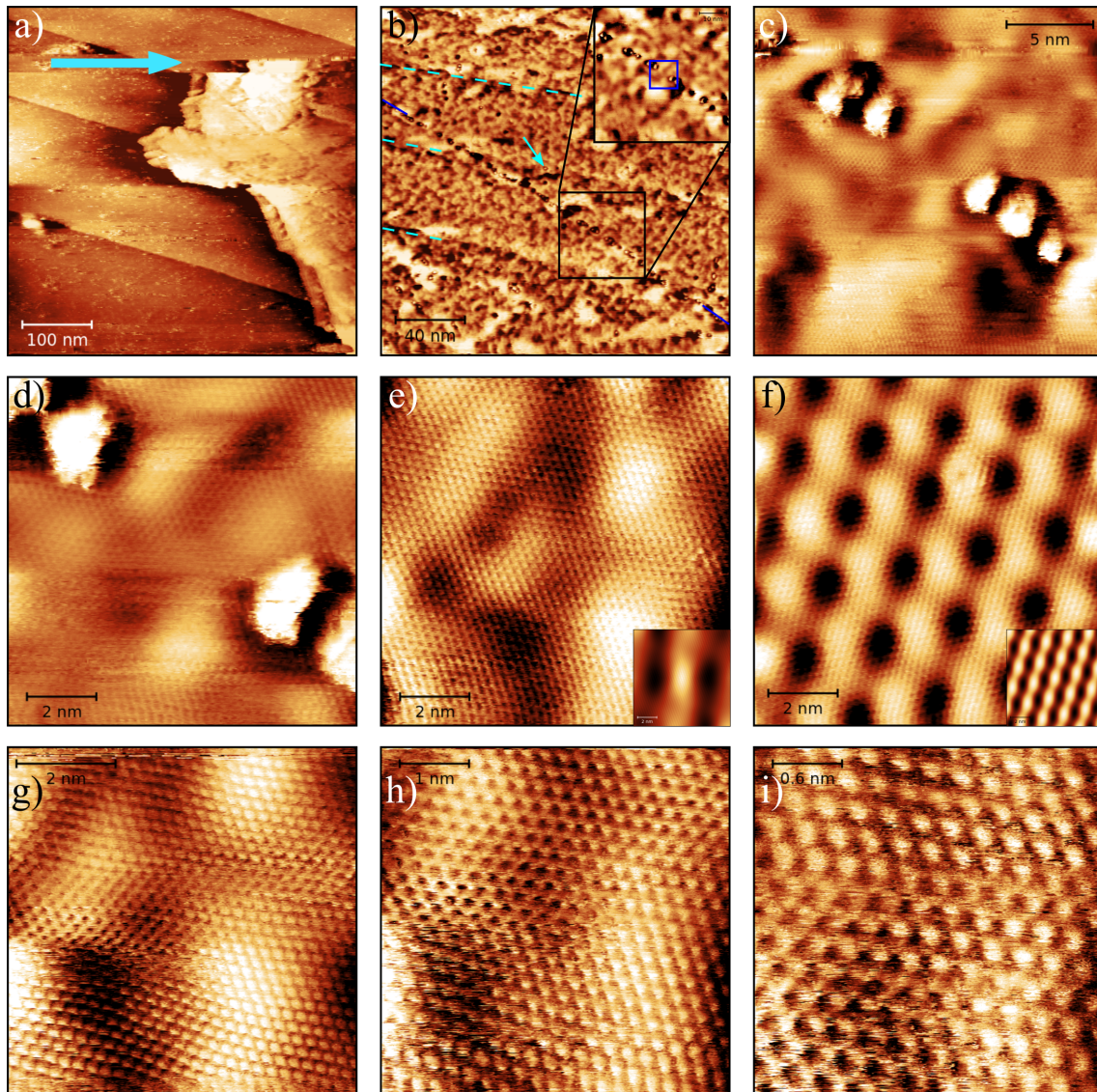
Figure 5.3: a) Large scale STM image of the edge of MoS$_2$ flake, with the point of ripping with the STM tip indicated with blue arrow. Image measured after this one on the same position showed no trace of a MoS$_2$ flake. b)Large scale STM image of the MoS$_2$ flake away from the edge. c) Zoom in on a line of point defects shown in b). d) Further zoom-in from b)&c which clearly shows that these defects are not domain boundary. e) Typicall atomic scale STM image of the corrugations, with autocorrelation image shown in inset. f) Moiré of a graphene on Ir(111) for comparison with e), with autocorrelation image shown in inset. g)-i) Zoom in in the area shown in e) that demonstrates contrast changes between hexagonal and honeycomb lattice.

with substrate even though this interaction is relatively weak (demonstrated by flake edge ripping, and the presence of a measurable band gap). Thus, taking into the account height variations over the sample, we cannot exclude the possibility of trapped/intercalated atoms between monolayer and Ir substrate, that could have

been introduced during transfer process.

In order to try to explain this apparent height variation i.e. brightness modulation, corresponding simulations were performed. This modulations could be caused by a topographic corrugation (change in height) or either be an effect of the metal-induced dipole (doping) or a change in the coupling between the metal and the MoS$_2$. This was investigated by changing (i) the distance between the MoS$_2$ layer and the metal (inducing a corrugation) and (ii) the coupling between them by modifying the composition of the top-most Ir layer. As shown in figure 5.4, the corrugation does not induce big changes in the STM images. However changing the coupling in certain ways can dramatically influence the images. Substituting Ir atoms by Mo affects the structure far less than simply removing Ir atoms or substituting them by S atoms. This most likely attributes the modulation effect to different hybridization rather than doping or level alignment, but further simulations are necessary for the complete understanding of this effect, which is out of the scope of the present work.
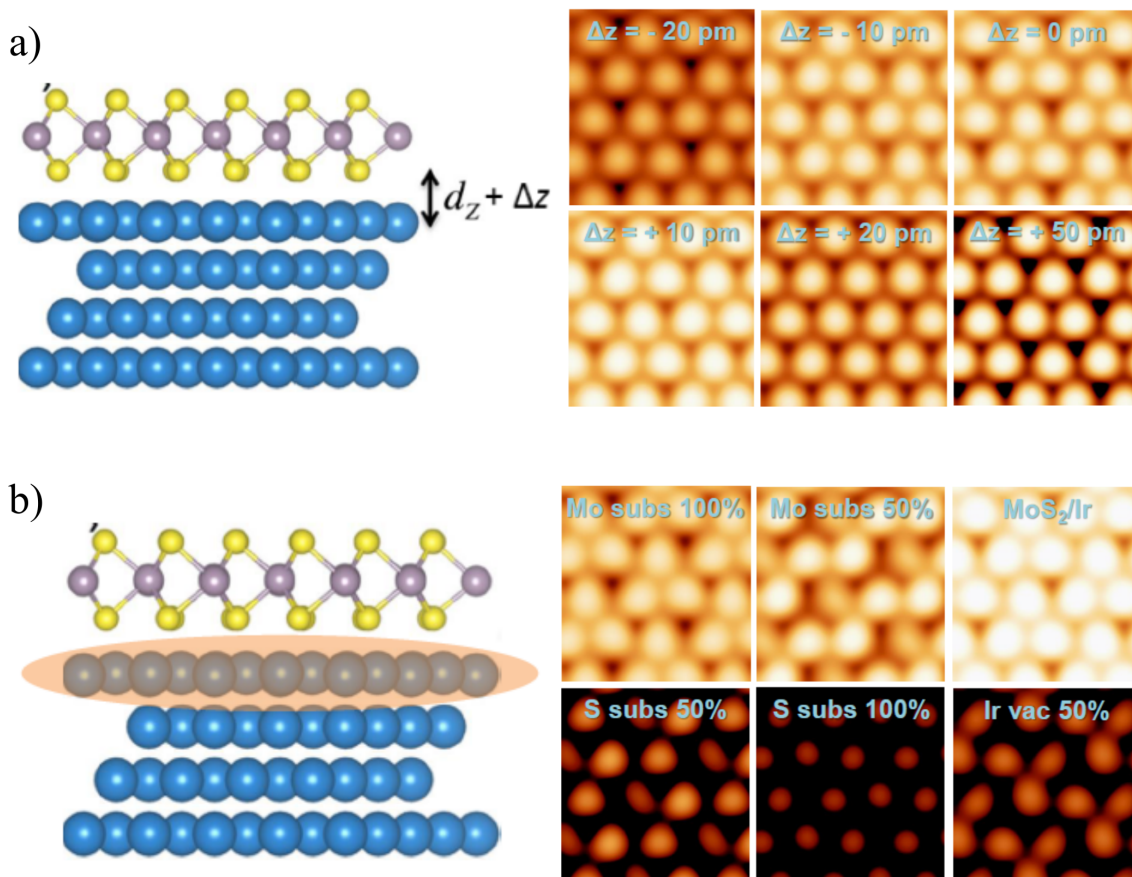

Figure 5.4: a) Investigation of the effect of the MoS$_2$-metal separation on the STM contrast in TH approach with V= -0.1 V. b) Investigation of the effect on the STM contrast of the MoS$_2$-metal interaction by changing the composition of the top metal layer in TH approach with V= -0.1 V.

Additional visible features in STM images presented in figure 5.3b include clear presence of Ir(111) monoatomic steps below continuous MoS$_2$ layer (light blue dashed lines in figure 5.3b) or larger adsorbate-like defects [50] present even on the largest scales and imaged as bright protrusions with locally extended dark surrounding (figure 5.3c, shown in more detail in figure 5.3d). From our characterization it appears that these type of defects are sometimes formed along the line (in a direction not necessarily correlated to that of Ir steps). Zooming-in on such lines of larger defects does not reveal apparent grain boundary, instead atomic resolution shows continuous propagation of crystal lattice across the line separating individual adjacent protrusions (figure 5.3d). We cannot, however, exclude the possibility of a grain boundaries with very small lattice rotations, as often observed in graphene [31], where small lattice rotations are noted from rotation of the moiré lattice that serves as a magnifying lens. In the absence of such magnifying lens, we can only argue that if bright protrusions follow the grain boundary, the lattice rotation angle is in the range of $\sim 1°$, i.e. extremely low.

Furthermore, related to the atomic resolution imaging of the areas of MoS$_2$ lattice without defects, it was observed that the lattice can be imaged in two different contrasts, i.e. like honeycomb or like hexagonal lattice [143]. This is apparently related to the rippling effect where elevated (brighter) areas in the nanoscale rippled layer typically exhibit hexagonal lattice contrast while the lower (darker) areas exhibit honeycomb lattice, as clearly visible in figure 5.3e and g-i. This effect is also known from imaging of epitaxial graphene, e.g. in figure 5.3f, where interaction with the substrate delicately influences lattice symmetry breaking in the imaged overlayer. Similar reasoning regarding the interaction with the substrate can be assumed with rippled MoS$_2$ consisting of areas closer or further apart from the Ir(111) substrate. In addition, we note that due to sandwiched structure of MoS$_2$, imaged honeycomb lattice exhibits variation of STM contrast within the individual rings, where three corners show brighter contrast and can be attributed to sulphur atoms, while darker corners can be attributed to contribution from molybdenum atoms in the underlying layer. By using a well-known lattice parameter of epitaxial graphene on Ir(111) [41] and measurements on MoS$_2$ performed with the same tip we determine the lattice parameter of our MoS$_2$ samples to be (0.30 ± 0.01) nm [143], which is in accordance with previously reported value [151, 152].

Generally, STM imaging towards smaller scales enables visualization of point defects even before crystal lattice is clearly resolved, as shown in a topograph in figure 5.5a. Such imaging also enables an insight into laterally variable concentration of point defects. For example, the upper right area of figure 5.5a is much poorer in
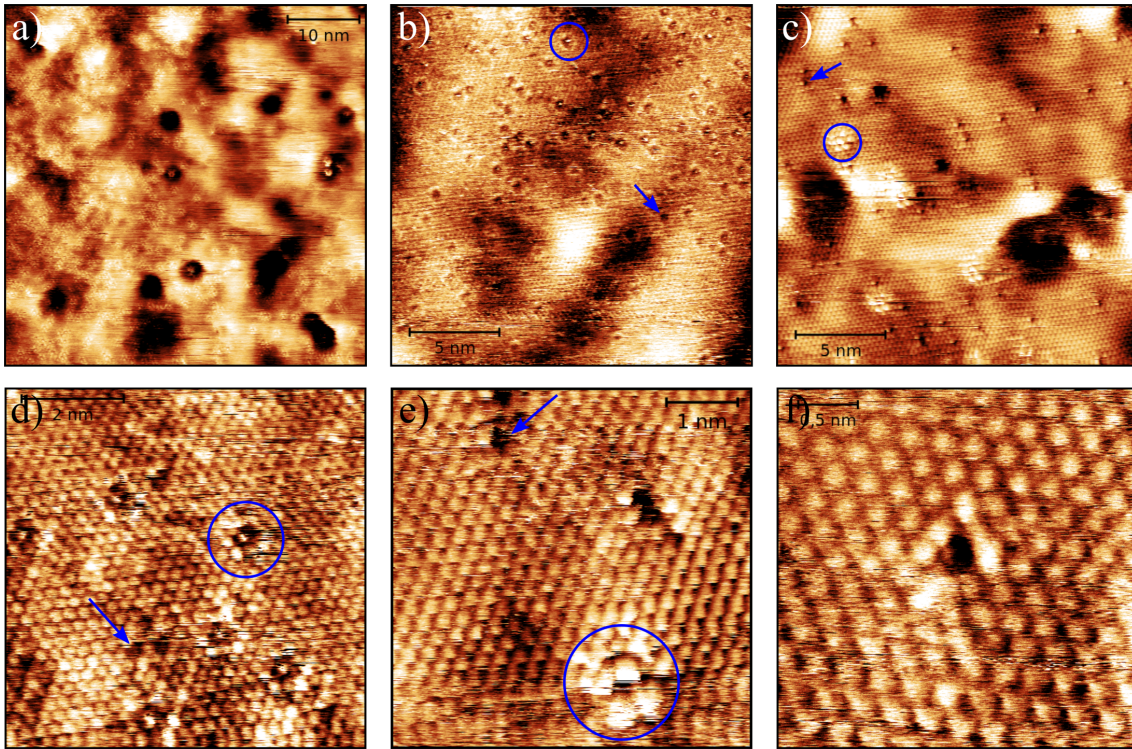
Figure 5.5: STM images of atomic defects exhibiting dependence of their appearance on imaging parameters. Generally, (up to) two types of defects can be distinguished, with similar looking defects in (b)-(d) indicated by arrows and circles. (a) Larger area with variations in defect density (V$_b$=170mV and I$_t$=1.2nA). (b) V$_b$=260mV and I$_t$=3nA, (c) V$_b$=-136mV and I$_t$=-1.4nA, (d) V$_b$=51mV and I$_t$=1.6nA. (e) Zoomed in area around indicated defects in (c) (V$_b$=-136mV and I$_t$=-1.4nA). (f) Zoom in on a triangle-like point defect (V$_b$=-136mV and I$_t$=-1.8nA).

defects than few tens of nanometers to the left area of figure 5.5a with much higher concentration of defects. It is also apparent that different concentration of defects is not specifically related to apparently higher or lower rippled areas of the MoS$_2$ layer. This is clearly visible in larger magnification images in 5.5b and c, which represent ideal image size for reliable statistical analysis of point defect concentrations. Defect density varies on the scales of tens of nanometers, but the maximum defect density found in our samples is around $2 \times 10^{13}/cm^2$, and the average value extracted from the statistical analysis on many STM images is $1 \times 10^{13}/cm^2$ [143], which is the same range as reported for the natural MoS$_2$ [50, 153]. Considering the fact that there are areas of the sample with far less defects than the average, we believe that further optimization of synthesis parameters will lead to even higher quality CVD monolayer MoS$_2$ samples.

Visibility and appearance of the point defects in STM images strongly depends on the applied imaging parameters (bias voltage and tunneling current) as expected
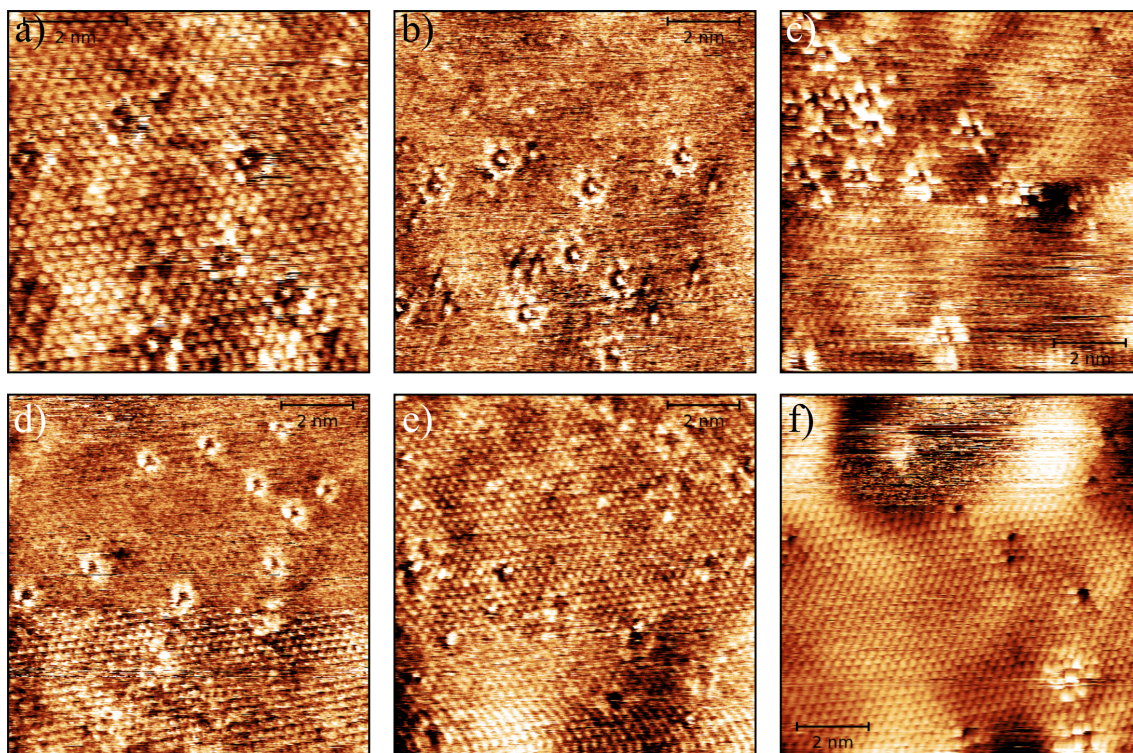
Figure 5.6: More of the STM images of atomic defects for a range of parameters with dependence of their appearance on imaging parameters. a) V$_b$=51mV and I$_t$=1.6nA, b) V$_b$=210mV and I$_t$=3.4nA, c) V$_b$=160mV and I$_t$=2nA, d) V$_b$=136mV and I$_t$=3.5nA, e) V$_b$=136mV and I$_t$=2.6nA, f) V$_b$=-136mV and I$_t$=-1.4nA

from semiconducting nature of MoS$_2$ and in line with previous reports [50, 153], with more examples shown in 5.6. In contrast to featureless larger bright protrusions mentioned in description of figure 5.3, there are at least two types of atomic defects identified in STM. Both types of defects are visible only in a small range of bias voltages. Moreover, their appearance changes within that narrow voltage range and we could resolve different shapes. Examples of similarly looking shapes are indicated by circles or arrows in 5.5.

The nature of these imaged atomic-scale defects can be revealed with the help of DFT calculations presented in figure in 5.7, with possible candidates that include sulfur monovacancy and divacancy, two different types of sulfur vacancies (lower or upper S missing) or S and Mo monovacancies. As seen in the presented simulated STM images, S divacancies and on-top vacancy look quite similar, while bottom S vacancy differs significantly. This could explain observation of 2 types of defects in STM images, as possibly S vacancy on top layer and divacancy looking the same (as dark triangle or circle), while S vacancy at bottom layer differs significantly (and possibly corresponding to flower-like observed shapes). As the details of the simulated

STM images depend on the simulated LDOS, they will be further elaborated in the next subsection.

MoS$_2$	S vacancy at top	S vacancy at bottom	S divacancy	ideal
isolated V=-0.1V				
on Ir(111) V=-0.1V				
on Ir(111) V=0.1V				
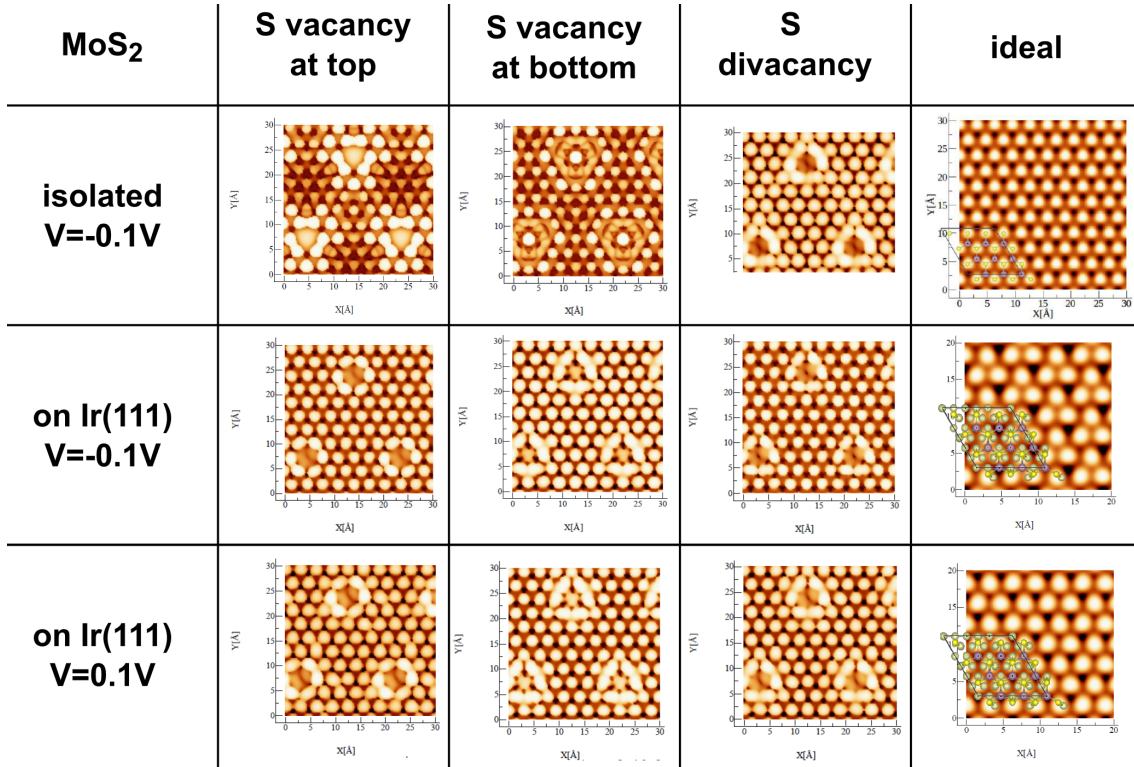
Figure 5.7: Overview of the simulations of STM images of monolayer MoS$_2$, with different types of defects and imaging parameters. S vacancy at top layer of MoS$_2$ and S divacancy exhibit similar features, while S vacancy at bottom layer of MoS$_2$ adopts different ones, which can account for two observed types of defects in STM measurements.

Additionally we performed annealing at 500K (215°C) for 30 minutes in UHV (10^{-9} mbar), to test how elevated temperatures affect the quality of our sample. Upon the annealing, no changes could be detected in LEED patterns, but in large scale STM images the sample surface appeared more flat, i.e. less rippled. However, significant disordering is induced on the atomic scale, as shown in figure 5.8. Numerous larger defects were introduced, often of the types not observed prior to annealing. Imaging with SEM and AFM didn't show any significant differences from the non-annealed sample.

5.3 Optical and electronic properties

Each step of the transfer process was followed by PL and Raman spectroscopy characterization of monolayer MoS$_2$, performed for each sample under ambient conditions [143]. Resulting curves are shown in figures 5.9 and 5.10. The dominating

Figure 5.8: Typical STM images of a MoS$_2$ on Ir(111) after annealing at 500K.

feature of PL is the A-peak exciton which relates to optical band-gap of single layer MoS$_2$ and which can be reliably fitted, its energy positions are indicated in figure 5.9 for each measured sample. The most prominent behaviour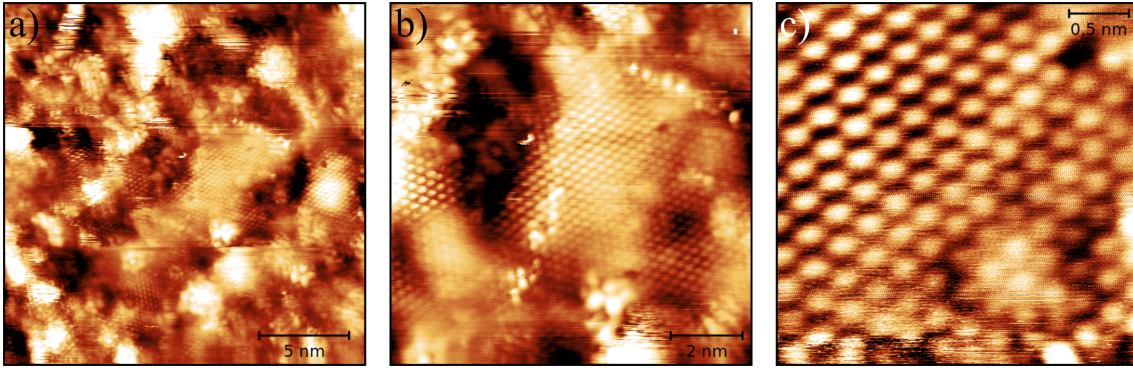 of PL spectra is a blue-shift shift of the optical band gap of ∼0.1 eV after the transfer from the growth substrate. Namely, the as grown MoS$_2$ exhibits optical band gap of 1.82 eV, and immediately after the transfer to any of the used substrates, the band gap is increased towards ∼1.9 eV. Besides this blue shift, we note the variation of the absolute PL intensity. The maximum intensity is recorded for MoS$_2$ on PDMS support and is more than 60% greater than that of the as grown sample, while subsequent transfers from PDMS to other substrates results in lower PL intensities, especially for MoS$_2$ on Ir(111), where PL intensity is an order of magnitude smaller than on PDMS. Raman spectroscopy characterization in figure 5.10 corresponds to same sample spots examined by PL in figure 5.9. Characteristic MoS$_2$ Raman peaks corresponding to out of plane A$_{1g}$ and in-plane E$^1_{2g}$ modes are recorded for each substrate and their values determined and indicated in figure 5.10, except for MoS$_2$/Ir(111) where the Raman active modes of MoS$_2$ appear to be completely suppressed.

PL spectra presented in figure 5.9 consist of A (1.82-1.90 eV) and B exciton (1.96-2.03 eV) peaks, that arise as a result of direct optical transitions from the near band edge [51, 52]. Moreover, another common feature at energies between 1.80 and 1.85 eV appears and it is associated with the emission from charged excitons (trions) of the A excitonic transition (A-) [54]. The energies presented in figure 5.9 correspond to A exciton transition, just to emphasize the influence of different substrates on PL spectrum [63, 154], both in peak positions and intensity. By fitting the data to Lorentzian functions, quantitative information about the PL spectra features can be extracted. Concerning PL peak position, as grown MoS$_2$ exhibits optical band gap of 1.82 eV and immediately after transfer (on all three explored
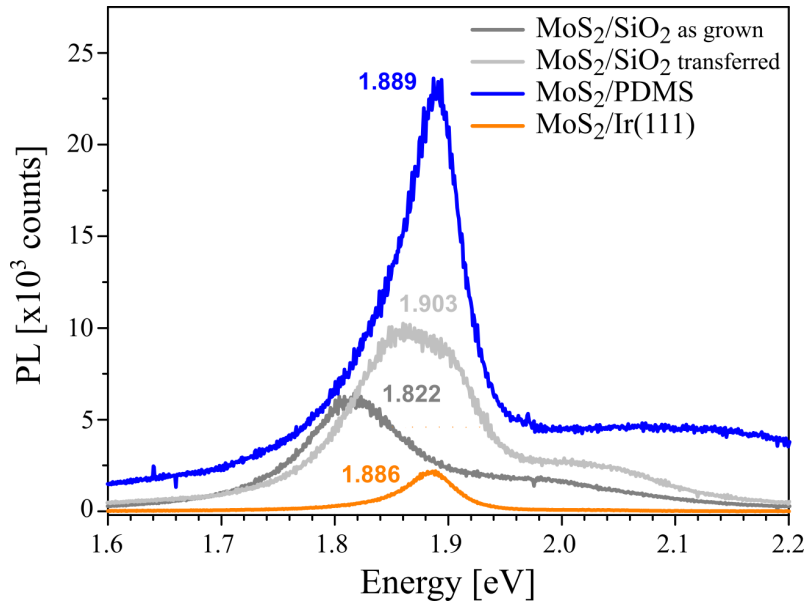
Figure 5.9: PL measurements of a MoS_2 monolayer on different substrates.
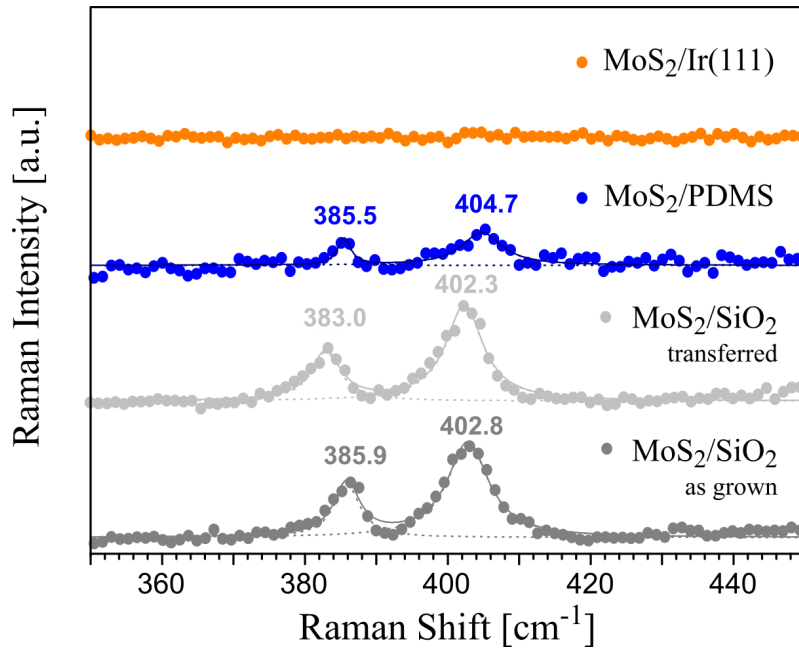
Figure 5.10: Raman measurements of a MoS_2 monolayer on different substrates.

substrates SiO_2, PDMS and Ir(111)) the optical band gap is increased to 1.9 eV, i.e. it is blueshifted by approximately 0.1 eV after the transfer. This effect is attributed to the release of tensile strain [155], intrinsic to the CVD grown MoS_2 on SiO_2 due to the difference in thermal expansion coefficient between MoS_2 and silica substrate resulting in a significant contraction mismatch during the fast-cooling process from the growth temperature toward room temperature. Estimation of this CVD growth-

induced strain variations, can be drawn from previous DFT calculations [155] and a relationship between the PL peak position shift and the strain variations can be obtained. The relative change of the calculated band gap with respect to uniaxial strain (44 meV per % strain) matches quite well the experimental results concerning the PL peak position shift with strain [58, 156]. Upon the transfer of MoS$_2$ to a new SiO$_2$/Si substrate, A exciton resonance shifts for about 80 meV, which corresponds to 1.83% of the global tensile strain in the as grown MoS$_2$ sample. The similar results were obtained by other groups [51, 155] with PL of the transferred monolayer on SiO$_2$/Si substrate being blueshifted and broader.

Overall PL signal intensity for transferred MoS$_2$/SiO$_2$ is 64% greater than PL intensity of as grown MoS$_2$/SiO$_2$ sample. PL of MoS$_2$ on PDMS shows practically no change in peak position and overall higher PL intensity compared to that of MoS$_2$ on SiO$_2$ (both as grown and transferred) due to the low interaction [157]. In fact, it was observed that the optical properties of MoS$_2$ on PDMS resemble those of free-standing MoS$_2$ (possibly due to the reduced charge transfer between the PDMS and MoS$_2$, which is much smaller than that of MoS$_2$/SiO$_2$ samples [63]). The PL intensity for MoS$_2$ sample transferred on PDMS has 3.9 times higher intensity than the as grown MoS$_2$/SiO$_2$ sample for the same excitation intensity. On the other hand, metallic iridium substrate also affects the PL intensity via additional nonradiative paths for exciton recombination (such as charge transfer processes and dipole-dipole interaction) [63, 158, 159, 160, 161] and the absolute observed PL intensity on Ir is 2.8 times lower than on SiO$_2$ for the same incident laser power.

Raman spectroscopy has proven to be an effective tool to determine, not only the number of layers of MoS$_2$, but also the built-in strain [162] in the layers as well as their doping level [163]. Figure 5.10 shows a comparison of the Raman spectra measured for MoS$_2$ single-layers deposited onto the different substrates. In the Raman spectrum, two characteristic Raman peaks appeared: E$_{2g}^1$ mode (around 385 cm^{-1}) and A$_{1g}$ mode (around 403 cm^{-1}). The distance between the A$_{1g}$ and E$_{2g}^1$ peaks (Δ = A$_{1g}$ - E$_{2g}^1$) was approximately 18.5 cm^{-1}, which is characteristic of monolayer MoS$_2$. The intensities and energies of E^1 $_{2g}$ and A$_{1g}$ modes are clearly modulated by the substrate. The Raman spectrum on specific sample was collected at the same location where the corresponding PL spectrum was taken. Softening of the E$_{2g}^1$ mode is observed after the transfer processes since it is known to be sensitive to the strain in the material [162, 164].

The complete absence of Raman signal on iridium substrate at least for our experimental conditions can be explained by the fact that iridium as a substrate suppresses Raman active modes [165]. Both Ir(111) [166] and Pd(111) [167, 168] are

intermediate between strongly and weakly interacting metal substrates for layered materials where the strength of the film-substrate interaction correlates with the ability to observe the Raman-active phonons.
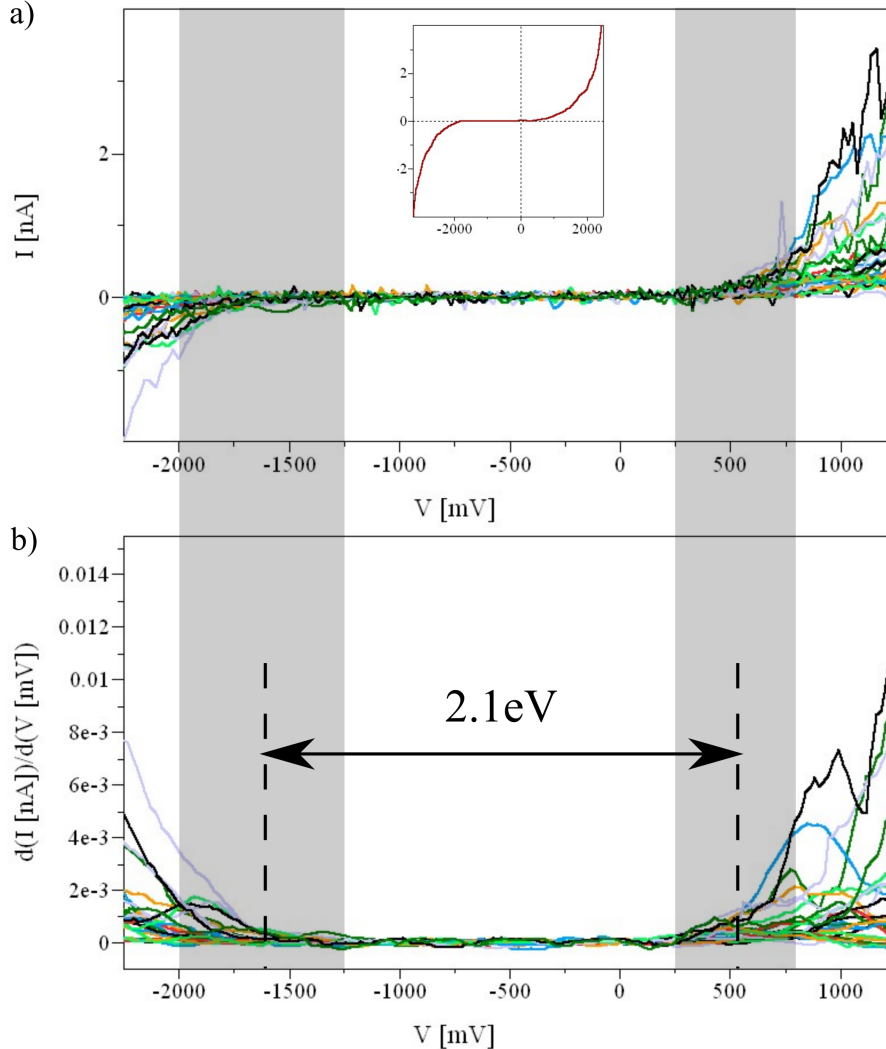
Figure 5.11: a) I(V) spectra measured with STS, with one typical spectrum in the inset. b) dI/dV spectra calculated from measured I(V) spectra.

In the course of STM characterization in UHV, also a band gap of MoS_2 on Ir(111) was characterized with STS. In order to obtain STS spectra that have dominant contribution from the sample (as with the images, resulting spectra are also convolution of the tip and sample contribution) I_t is reduced, while V_b is increased to increase tip-sample distance [169]. STS measurements were typically performed after detailed atomic resolution characterization was obtained. This enabled us to ensure that there are no adsorbates or large defects and/or domain boundaries in the area inspected by STS, where several I(V) spectra were taken on different parts of the image. Procedure was repeated for different areas of the sample, always within

the area without large defects. The fact that our experiments were performed at room temperature and due to certain level of thermal drift, we were not able to make spectroscopy on individual point defects. Measured spectra and their derivatives are showed in figure 5.11a and 5.11b, respectively, confirming in each case semiconducting character and n-doping of the MoS_2 monolayer. The dI/dV spectra enabled us reliable extraction of the gap width for individual spectra. Thus determined average width of the band gap is found to be (2.1 ± 0.1)eV [143]. From the difference in band gap determined from STS and the optical band gap, exciton binding energy can be estimated to $\sim$0.2eV, which is in accord with previous reports [57, 170].

Position of the band gap indicates n-doping compared to freestanding MoS_2 monolayer. Two main possible sources of the doping are atomic defects (mostly sulfur vacancies [171]) and interaction with metallic substrate, which will be discussed in more detail in the following with the aid of DFT calculations.
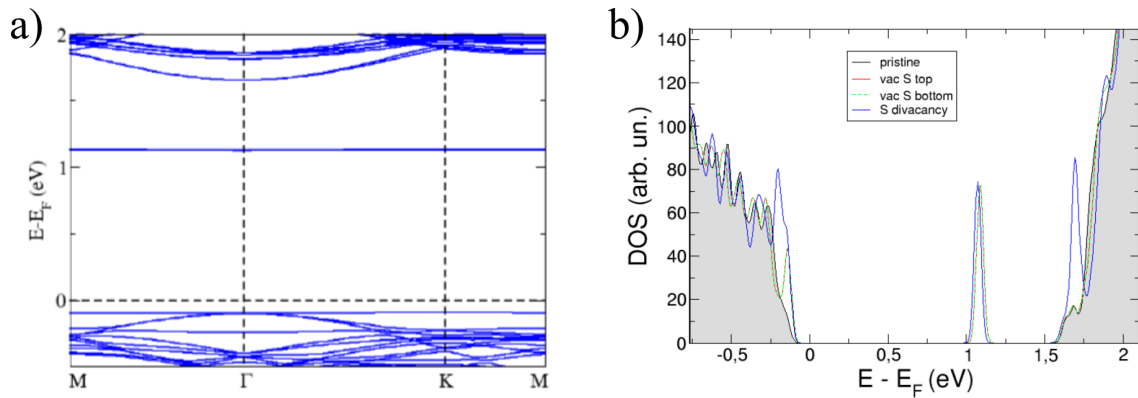
Figure 5.12: Simulated electronic structure of freestanding MoS_2 monolayer. a) Band structure in a presence of a S vacancy at the top layer. Calculations for the other two types of atomic S defects are not shown, because of large similarity. b) Comparation of DOS for a pristine layer and specific defects.

The simulated STM images of the isolated (without metal substrate), pristine (no defects) MoS_2 monolayer (shown in top right corner in the figure 5.7) is basically the image of the outer region of the states of the conduction or valence band (depending on bias voltage) edge. These states are highly hybridized states between S and Mo ("bonds" for the valence band). Hence, far from the layer the Tersoff-Hamann (TH) approach first "sees" the S (bright), then the hollow (most likely the bonds), and then, darker, the Mo. The presence of the defects induces a very localized peak in the mid-gap, at $\sim$1.2 eV above the Fermi level for all the S vacancies (S vacancy at top and bottom layer and S divacancy), as shown in image 5.12. This state has mostly the contribution from the d orbital of the Mo atom closest to the defect. The state induced by the S monovacancy in the mid-gap is very much localized around

the neighbouring Mo atoms (with a rapid decay in the perpendicular direction). Therefore, in the STM images this defect can be seen as a dark triangle/hole (a missing S), both for empty and filled states. When we approach the tip to the MoS$_2$ at the opposite side of the vacancy this state is, in contrast, seen as a blurred bright feature extending over the closest S's. As for the S divacancy, one of the peaks of the conduction bands slightly enters the gap, somewhat modifying the conduction band, but the STM images are nevertheless very similar to those of the monovacancy (a dark triangle).

When the metal Ir(111) substrate is included in the simulations for both pristine and defected MoS$_2$, two main effects on the electronic structure of the system occur [128, 129]. Firstly, the bonding between the metal surface and the closest S's of the MoS$_2$ hybridizes the Mo-S states. This induces gap states, and metallization, of the MoS$_2$, as seen in figure 5.13. Additionally, pinning of the Fermi level occurs and triggers the shift of the MoS$_2$ levels towards negative energies (which can be associated with n-doping observed in STS measurements).
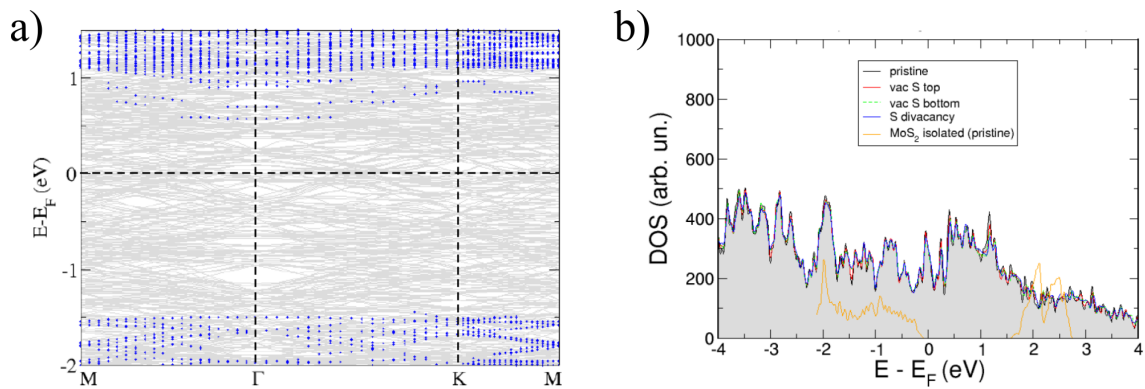
Figure 5.13: Simulated electronic structure of MoS$_2$ monolayer on Ir(111). a) Band structure with Ir contributions in grey and MoS$_2$ contributions in dashed blue lines. b) Comparation of DOS for a pristine layer and specific defects.

5.4 DNA tetrahedra adsorption

In order to proceed towards the adsorption of DNA tetrahedra, stability of the MoS$_2$ monolayer on Ir(111) upon immersion in liquids (deionized water and TE buffer) was checked. Immersion in both liquids did not introduce additional macroscopic defects. Adsorption was conducted according to previously established protocol (subsection 2.2.3), and sample was characterized using UHV-STM, AFM and PL (in addition to SEM, where no discernible differences were observed).

AFM images of DNA tetrahedra adsorbed on MoS$_2$/Ir(111) substrate on the large scale show some difference compared to the absorption on two other substrates, namely, density of the adsorbed layer was much lower, as shown in figures 5.14a&b. Measured heights of the adsorbates are 3-4 nm, in accordance with previously mentioned adsorbed layers on graphene and Au(111), as shown in profile in figure 5.14c.
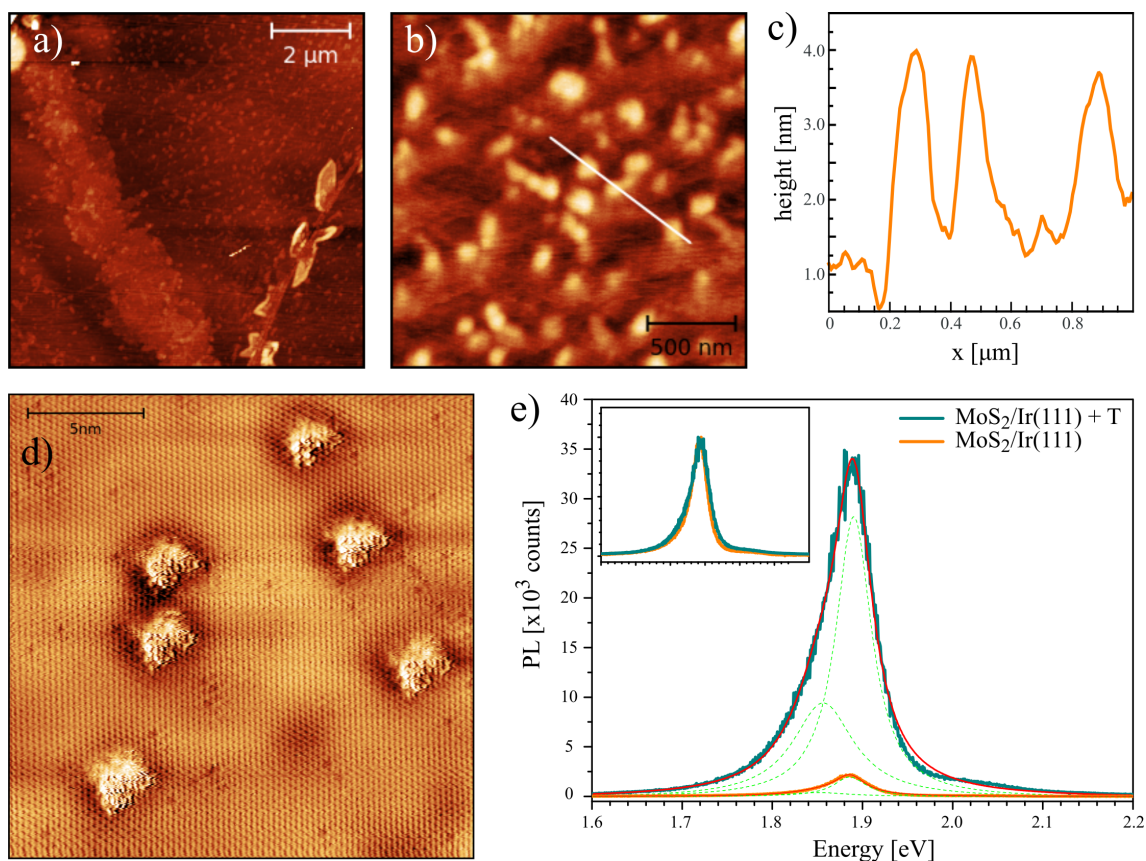
Figure 5.14: a)&b) AFM topography images of the adsorbed DNA tetrahedra layer on MoS$_2$ monolayer on Ir(111). c) Profile marked in the b). d) STM image of separate tetrahedra adsorbed on MoS$_2$. d) PL measurements before and after tetrahedra adsorption. Inset shows same spectra after normalization.

STM imaging in UHV show that biomacromolecules have adsorbed randomly on the surface, and it is assumed that disulphide groups bonded with sulfur vacancies, as S vacancy sites are more reactive than rest of the surface [57]. Around the molecules darker areas appeared, which can be attributed to the charge transfer and/or charge trapping in these areas (figure 5.14d). In the figure 5.14d tetrahedra exhibit similar shape and orientation. This is due to the fact that compared to the tip apex they are relatively sharp protrusions, so tip-sample convolution has a significant role in their imaging. Tetrahedra are adsorbed relatively randomly on the surface (as was expected in the absence of a template which could induce ordering), but by

changing the parameters of the adsorption (concentration in the buffer and length of incubation) their total number can be tuned. Since MoS$_2$ monolayer is easily transferred to different substrates this system is open for further application, as opposed to tetrahedra adsorbed on AuIr lattice on graphene on Ir(111).

The PL spectra of a MoS$_2$ monolayer on Ir(111) measured before and after DNA tetrahedra adsorption show a 16-fold increase in the PL peak intensity (figure 5.14e), with no change in the overall spectral shape (as shown in inset in figure 5.14e where normalized spectra are compared). There are two known possible causes for such PL enhancement. The first is the influence of charge transfer from DNA to MoS$_2$: the phosphate backbone of DNA nanostructures attracts and holds hole carriers on the side of MoS$_2$, thereby n-doping the MoS$_2$ [71]. This would result in the charge exciton population (trions) increase after the DNA tetrahedra adsorption [172]. Overall exciton and trion populations can be extracted from the peak areas: before the adsorption of tetrahedra A/A-area ratio of the MoS$_2$/Ir(111) sample is 2.8 while afterward it is 1.9. From this, we can conclude that charge transfer in the presence of DNA, i.e. additional n-doping of MoS$_2$ monolayer is not the reason of PL enhancement.

Second possible cause for PL enhancement is the suppression of nonradiative recombination of excitons at defect sites. Since MoS$_2$ surfaces contain regions with a large number of defect sites in the form of sulfur vacancies, adatoms on the surface and numerous impurities act as deep-level traps which contribute to defect-mediated nonradiative recombination, resulting in a PL suppression [56]. Since the sulfur vacancies also represent chemically reactive sites on the surface, we assume that these sites are actually sites of the tetrahedra binding. Unlike the mechanism of the conversion between exciton and trions, we observed no changes in PL spectral shape after DNA adsorption on surface (inset in figure 5.14d). However, huge enhancement of PL spectrum can be attributed to the defect reduction and, consequently, defect-mediated nonradiative recombination minimization [17] due to specific binding of disulphide groups to S vacancies. To further investigate the carrier recombination dynamics, we should perform time-resolved measurements on both as-transferred and DNA treated samples which is out of scope of the present work.

Conclusions

Motivation for the work presented was the building of a hybrid system, consisting of a solid state substrate and a layer of biomacromolecules, which are currently widely studied, as they not only bridge the gap between living matter and technology but also have promising applications in nanotechnology as single molecule sensors or as part of bio-optoelectronic devices. While our final goal was a hybrid system consisting of a two-dimensional (2D) support (graphene or monolayer MoS_2) and adsorbed layer of biomacromolecules, we were mostly focused on the reproducible preparation and extensive characterization of the nanopatterns themselves, as they can later be used as a supports for different biomacromolecular layers. As a part of this work two hybrid systems were created and their structure and properties were studied with diverse experimental techniques. A focus on the potential applications in future devices like sensors or bio-optoelectronic devices was always kept.

One hybrid system was realized with graphene grown on Ir(111) which exhibits moiré effect, a hexagonal superperiodicity with lattice constant of 2.5 nm. This feature provides a very suitable template for growth of ordered metallic nanoclusters. Our goal were the golden clusters as they should specifically bind sulfur functionalized biomacromolecules. For the gold clusters cluster seeding with iridium was necessary. Thus we obtained ordered array of bimetallic clusters consisting of ≈ 20 atoms, whose internal structure may be recognized (by DFT calculations) as core-shell.

Resulting AuIr cluster array was proven to be stable upon exposure to ambient air and liquid conditions. On the other hand upon intercalation with Cs or Li in UHV cluster disordering occurs. Further, after transfer to SiO_2 substrate clusters were completely removed. Due to the fact that clusters proved unstable in regard to the graphene transfer, adsorption of biomacromolecules could have been attempted only on the as-synthesized nanotemplates, still bound to Ir(111).

The biomacromolecular structure of choice was DNA origami tetrahedra which

have hexagonal symmetry similar to moiré and whose characteristic size (length of the edges) can be adjusted on the nanometer scale, while its vertices can be functionalized with different chemical groups depending on the planned use. We opted for approximately 5 nanometers long edges (that is double the lattice constant of the moiré) and disulphide groups on the three vertices, to enable thiol bonds with the nanopattern. DNA tetrahedra adsorbed readily on the nanopattern, however, they did not assemble into lateral long-range ordered array. Since this nanotemplate turned out to be only stable while kept on the single crystal on which it was synthesized, it is not suitable for further applications. However, as a template it can be used to study individual macromolecule adsorption and assembly upon adsorption of different kinds of biomacromolecules functionalized with linkers which can form thiol bonds.

Second investigated 2D support was monolayer MoS_2, which was synthesized on SiO_2 wafer and transferred to Ir(111) surface for nano-scale characterization. Monolayer was extensively characterized during every step of the transfer process, and final substrate examined down to atomic level. We concluded that our procedures yielded high quality CVD grown monolayer MoS_2 of millimeter scale size with defect density in the same range as samples exfoliated from the natural MoS_2. During the transfer process, immediately after lift-off from the substrate on which layer was synthesized, release of a tensile strain occurs resulting in a widening of the optical band gap. Upon transfer to the Ir(111) surface there is strong suppression of the PL signal due to the interaction with the metallic substrate. However, upon the adsorption of the DNA tetrahedra PL signal increased 16 fold, while the overall spectral shape remains unchanged. This increase is signal can be attributed to the suppression of nonradiative recombination channels.

This research advances interdisciplinary research between DNA nanotechnology and 2D TMD based device technology. The strong and stable PL from defects sites of MoS_2 may have promising applications in optoelectronic devices.

Prošireni sažetak

1 Uvod

Od samih početaka razvoja mikroelektronike i integriranih krugova, površine, kao granična područja dvaju materijala ili dvije faze, imaju značajnu ulogu prilikom osmišljavanja i razvoja novih uređaja. Davne 1959. u svom slavnom govoru [1] R. P. Feynman je skrenuo pozornost na tada relativno neistraženo područje minijaturizacije tehnologije te tako pokrenuo revoluciju u području. Čitajući danas zapis njegovog govora, očito je kako su se mnoge stvari koje je predvidio ostvarile (kao što su npr. smanjivanje računala, pohrana velike količine podataka u malom prostoru, manipulacija pojedinim atomima [2] i sinteza novih materijala), dok su neke ipak još uvijek neostvarene. Kako tehnologija napreduje, sve se više elektroničkih elemenata može smjestiti na području iste površine, po Mooreovom zakonu (koji kaže da se broj tranzistora po integriranom krugu udvostručuje svake dvije godine [3]). Ipak, daljnje smanjivanje tehnologije koja je bazirana na siliciju približava se fizikalnoj granici mogućeg, te je potraga za adekvatnom zamjenom vrlo popularna tema istraživanja[4, 5].

U 2004. grafen [6] je došao na scenu donoseći brojna obećanja mogućih primjena u daljnjem razvoju elektronike. Iako je grafen bio prvi, a još uvijek je i daleko najistraživaniji dvodimenzionalni (2D) materijal, nije jedini. Još od samih početaka istraživanja grafena, postalo je jasno da unatoč dotadašnjem uvriježenom mišljenju da takvi materijali neće moći biti stabilni (što su potvrđivali teorija i eksperimenti koji su proučavali stabilnost tankih filmova), ipak postoje te je otkrivena još nekolcina 2D materijala, kao što su molibden disulfid, volfram disulfid (predstavnici dihalkogenida prijelaznih metala) ili heksagonalni borov nitrid (hBN). Ove se 2D kristale smatra dobrom potencijalnom građom za iduću generaciju nosivih, savitljivih, rastezljivih i prozirnih elektroničkih uređaja zbog njihovih iznimnih električnih, optičkih i mehaničkih svojstava.

Grafen je monosloj ugljikovih atoma uređenih u kristalnu rešetku pčelinjih saća odnosno heksagonalnu rešetku sa dva atoma u bazi. Duljina veze između susjednih

ugljikovih atoma iznosi 1.42 Å, dok je konstanta rešetke 2.45 Å [21]. Kristalna rešetka nastaje hibridizacijom s, p_x i p_y atomskih orbitala pojedinih ugljikovih atoma koja rezultira jakim kovalentnim sp^2 vezama (i posljedično σ vrpcom), dok preostale p_z orbitale tvore valentnu (π) i vodljivu (π^*) vrpcu. Rezultirajuća elektronska disperzija je linearna u okolini Fermijevog nivoa, sa π i π^* vrpcama koje se dotiču u K i K' točkama Brillouinove zone, čineći grafen polumetalom. Posljedično, transport elektrona u grafenu opisan je (relativističkom) Diracovom jednadžbom i nosiocima naboja koji se opisuju kao relativističke kvazičestice bez mase mirovanja. To rezultira iznimnim karakteristikama kao što su balistički transport i velika mobilnost koja slabo ovisi o temperaturi, ambipolarna vodljivost i kvantni Hallov efekt [25]. Osim elektronskih, grafen posjeduje i mnoga druga iznimna svojstva, kao što su Youngov modul od ≈ 1.0 TPa, termalna vodljivost od ≈ 5000 $Wm^{-1}K^{-1}$, nepropusnost na mnoge plinove te prihvaćanje raznih adsorbata. Iako postoji mnogo metoda za dobivanje grafena, uzorci istraživani u ovom radu dobiveni su epitaksijalnim rastom na površini monokristala Ir(111) u komori s ultra-visokim vakuumom. Tako dobiveni grafen je monosloj visoke kvalitete, koji prekriva čitavu površinu uzorka, promjera 6 mm. Zbog nesumjerljivosti grafenske i iridijeve kristalne rešetke, dolazi do pojave superperiodične naboranosti grafena, sa konstantom rešetke od 2.5 nm, koja se naziva *moiré* strukturom [41]. Ovaj sustav pogodna je podloga za rast uređenih metalnih nanočestica, koje se dobivaju naparivanjem male količine metala na grafen, pri čemu pojedini metalni atomi sjedaju na preferirano mjesto na *moiré* rešetci, čineći uređenu matricu metalnih nanočestica sa konstantom rešetke istom kao i *moiré* [40, 42].

Monosloj molibden disulfida, kao predstavnik dihalkogenida prijelaznih metala (TMD), je jedan od najčešće istraživanih danas. Iako se TMD naširoko istražuju već desetljećima, njihove 2D varijante su prototip modernih materijala sa širokim rasponom svojstava koje se protežu od metalnih do poluvodičkih, te nekih egzotičnih poput supravodljivosti i valova gustoće naboja [44, 45]. Monosloj MoS_2 je veoma stabilni poluvodič sa direktnim međuvrpčanim procjepom koji ima mnoštvo potencijalnih primjena u elektronici, fototranzistorima, fotodetektorima, senzorima, izvorima svjetlosti, optoelektroničkim uređajima i savitljivoj elektronici [17]. Sastoji se od heksagonalne rešetke molibdenovih atoma ugniježđenih između dva sloja sumporovih atoma, također heksagonalnog uređenja, s konstantom rešetke koja iznosi 3.16 Å i debljinom monosloja od 3.01 Å [49, 50]. Dok je mnogoslojni, *bulk* MoS_2 poluvodič sa indirektnim procjepom od 1.3 eV, u granici jednog sloja postaje poluvodič sa direktnim procjepom od ≈ 2 eV. Širina procjepa, a time posljedično i optoelektronička svojstva (npr. fotoluminiscencija - PL) se dodatno mogu modificirati vanjskim utjecajima kao što su naprezanje, dopiranje, kemijski tretmani ili uvođenje dodatnih

defekata.

Struktura i svojstva čine DNK molekule iznimno pogodnima za primjene u nanotehnologiji, od promjera od ≈ 2 nanometra i modularne strukture do svojstva međusobnog prepoznavanja parova baza. Specifičnost sekvence DNK koristi se u pristupu od dna prema gore (*bottom-up approach*), gdje se osmišljavanjem sekvence samosastavljanjem dolazi do nanostruktura željenog oblika [65, 68], koje dodatno mogu biti funkcionalizirane na lako kontrolirani način. DNK se također može kombinirati i sa ostalim materijalima, npr. sa metalnim nanočesticama (klasterima) ili drugim biomakromolekulama.

Nanotehnologija bazirana na DNA kao i na 2D materijalima ima velike potencijale za razvoj iznimno malih uređaja sa sve složenijom funkcionalnošću. Nadalje, funkcionalizacija 2D materijala s DNA (ili drugim biomakromolekulama) ima potencijalne primjene u (bio)kemijskim senzorima [70, 71]. Dakle, usporedno s razvojem 2D materijala za primjenu u elektronici, dodatni napori su usmjereni prema kombiniranju bioloških struktura (koje su već same po sebi nanostrojevi) i tehnologije temeljene na modernim materijalima [72].

Za razliku od nespecifične adsorpcije DNK na grafen, za jače, specifično vezanje, može se koristiti tiolna veza. Tiolna veza je kovalentna veza između zlata i sumpora koja rezultira vrlo robusnim i prilagodljivim interakcijama koje su presudne za stabilizaciju nanostruktura i prijenos elektronskih međudjelovanja između zlata i organskih molekula sa sumporom [78]. Jačina te veze između tiola i zlata (RS-Au) je bliska jačini veze između pojedinih atoma zlata, što znači da može znatno modificirati vezanje atoma zlata na granici između zlata i sumpora. Posljedično, za razliku od kemijske inertnosti zlata na velikim skalama, nanometarski objekti građeni od zlata se odlikuju bogatom kemijom.

2 Materijali i metode

Eksperimenti opisani u ovom radu, uključujući pripremu i karakterizaciju uzoraka, provedeni su ili pod uvjetima ultra-visokog vakuuma (UHV) ili u atmosferskim uvjetima i/ili u otopinama. UHV sinteza grafena i metalnih nanoklastera te njihova karakterizacija kao i karakterizacija $MoS_2/Ir(111)$ sustava, te oba hibridna sustava provedena je u UHV-STM komori, pri bazičnom tlaku od 10^{-9} mbar.

Za preliminarnu karakterizaciju uzoraka korištena je difrakcija elektrona niskih energija (LEED), a za detaljnu pretražna tunelirajuća mikroskopija (STM) i spektroskopija (STS). Za pripremu iznimno čiste visoko uređene monokristalne podloge

korišteni su ciklusi bombardiranja ionima argona i prženja u kisiku. Sinteza grafena provođena je kombinacijom TPG i CVD ciklusa [37]. Uređena matrica metalnih klastera na grafenu dobivena je naparivanjem ≈ 0.1 ML iridija i zlata.

Transfer grafena sa Ir(111) na SiO_2 podlogu proveden je postupkom elektrokemijske delaminacije [90, 91]. Sinteza monosloja MoS_2 provedena je u CVD peći kućne izrade. Prijenos na čisti Ir(111) kristal proveden je uz pomoć PDMS filma [95, 96, 97], unutar pola sata od vađenja kristala iz vakuuma. Ispitana je stabilnost obje 2D podloge pod atmosferskim uvjetima i u tekućinama, te je provedena depozicija DNK tetraedara, nakon čega su uzorci vraćeni u UHV komoru na daljnju karakterizaciju.

Kao prikladna biomakromolekula pokazala se DNK struktura vrlo visoke simetrije - DNK origami tetraedar [98]. Ta struktura posjeduje heksagonalnu simetriju analognu *moiré* rešetci grafena sa karakterističnom veličinom (duljinom stranica) koja se može prilagođavati na nanometarskoj skali, dok im se vrhovi mogu funkcionalizirati različitim kemijskim skupinama koje se koriste u biotehnologiji (kao što su vezivne molekule poput biotina, tiola ili fluorofora), ovisno o planiranoj upotrebi. Izabrali smo duljine stranica od otprilike 5 nm (što je dvostruka duljina konstante rešetke *moiréa*) i disulfidne skupine na 3 vrha, koje omogućuju tiolno vezanje na prikladnu podlogu [99].

Otopine DNK tetraedara pripremeljene su prema navedenim protokolima, te je njihova kvaliteta provjerena uz pomoć elektroforeze. Kvarcna mikrovaga sa mogućnošću mjerenja disipacije (QCM-D) korištena je za kontrolu depozicije biomakromolekula. 2D podloge i konačni hibridni materijali karakterizirani su mikroskopom atomskih sila (AFM), pretražnim tunelirajućim mikroskopom (STM), skenirajućim elektronskim mikroskopom (SEM) te mjerenjem optičkih svojstava (fotoluminiscencija (PL) i Raman), ovisno o uzorku. Dodatno, za razjašnjenje atomske građe AuIr nanočestica provedene su simulacije molekularne dinamike (MD), dok je $MoS_2/Ir(111)$ sustav modeliran uz pomoć teorije funkcionala gustoće (DFT).

3 Biomakromolekule na ravnim podlogama zlata

Kao prvi korak od 2D materijala prema hibridnom materijalu bilo je potrebno optimizirati parametre za adsorpciju biomakromolekula: poput koncentracije i veličine samih biomakromolekula, kao i koncentracije dodanih soli, pH, temperature i drugih parametara. Budući da nije bilo praktično istraživati sve ove parametre na samim 2D materijalima jer je njihova priprema vremenski zahtjevna, korištene su modelne

površine, konkretno različite ravne površine zlata. Isprobane su površine komercijalnog QCM-D čipa, tanki sloj zlata evaporiran na SiO_2 čip, TSG zlato i Au(111) monokristal. Od ispitanih površina, jedino se Au(111) kristal pokazao prikladnim za efikasnu karakterizaciju AFM-om i STM-om nakon adsorpcije biomakromolekula. Zbog toga je proces adsorpcije praćen QCM-D-om, a SPM karakterizacija provedena na Au(111), na kojem je adsorpcija provedena analognim protokolom. Nakon adsorpcije DNK tetraedara na Au(111) površinu AFM mjerenja ukazuju na formiranje nepotpunog monosloja, no zbog radijusa zakrivljenosti vrha AFM probe, pojedinačni tetraedri se ne mogu razlučiti. STM karakterizacijom u UHV uvjetima razaznaju se pojedini tetraedri, nasumce raspoređeni po površini.

4 Metalne nanočestice i biomakromolekule na grafenu

Da bi se postiglo specifično vezanje DNK na grafen preko tiolnih veza, potrebno je prvo funkcionalizirati grafen. Grafen na Ir(111) podlozi posjeduje dodatnu superperiodičnost od tzv. *moiré* efekta, heksagonalne simetrije sa konstantom rešetke od 2.5 nm. *Moiré* rešetka je vrlo pogodna podloga za formiranje metalnih nanočestica, jer se male količine (0.1-0.2 ML) nekih metala naparene na gr/Ir(111) spontano uređuju u nanočestice, sa centrima uvijek na istom području *moiré* jedinične ćelije [42]. Iako se zlato (koje je specifično potrebno da bi se mogle formirati tiolne veze) napareno na gr/Ir(111) ne uređuje u nanočestice, moguće ih je dobiti prethodnim naparivanjem prekursora nekog metala koji daje uređene dobro definirane klastere. Isprobano je više metala, od kojih se iridij pokazao najpogodnijim. Dobivena je uređena matrica AuIr kompozitnih nanoklastera koji se sastoje od $\approx$ 20 atoma, sa unutarnjom strukturom od Ir jezgre i Au ljuske, što je potvrđeno MD simulacijama [138].

Potvrđena je stabilnost klastera na izlaganje atmosferskim uvjetima i izlaganju tekućinama. Kao prvi korak prema potencijalnoj primjeni, planiran je prijenos grafena zajedno sa klasterima na SiO_2 podlogu. Prvi korak oubičajene procedure prijenosa je interkalacija Cs u UHV. No, interkalacija grafena sa Cs ili Li rezultira uništenjem uređene strukture matrice. Dodatno, nakon završenog prijenosa grafena na SiO_2 podlogu, čestice više nisu prisutne. Zbog toga je adsorpcija DNK tetraedara provedena samo na tek sintetiziranom nanopredlošku na Ir(111) podlozi.

Nakon adsorpcije DNK tetraedara, AFM mjerenja prikazuju adsorbirani sloj molekula vrlo sličan onom formiranom na Au(111). Mjerenja STM-om potvrđuju

adsorpciju DNK tetraedara, međutim, prilikom adsorpcije nije došlo do uređenja molekula. Pošto je ova podloga primjenjiva samo dok se nalazi na Ir(111) monokristalu, nema potencijala za daljnje primjene, osim za proučavanje uređene adsorpcije biomakromolekula funkcionaliziranih sa kemijskim skupinama koje se mogu vezati tiolnom vezom.

5 Biomakromolekule na MoS$_2$ monosloju

Monosloj MoS$_2$ koji je sintetiziran na SiO$_2$/Si podlozi prenesen je uz pomoć PDMS sloja na Ir(111) monokristalnu podlogu, za detaljnu karakterizaciju na nanometarskoj skali. Parametri sinteze su prilagođeni rastu jednog atomskog sloja, sa što manjom prisutnošću dijelova sa 2 ili više atomskih slojeva. Tek sintetizirani uzorak okarakteriziran je uz pomoć optičkog mikroskopa, AFM-a i SEM-a, te je potvrđena uniformnost i kvaliteta uzorka. Iako se uz rubove uzorka mjestimično nalaze mjesta koja nisu u potpunosti prekrivena, dobiven je monosloj veličine milimetra s prosječnom gustoćom defekata usporedivom s onom prirodog MoS$_2$ [50, 153]. Na rubovima uzorka javljaju se karakteristični otoci sa rubovima pilastog oblika, a po cijelom uzorku se na skalama od 10-100 μm javljaju nabori visine 5-10 nm. Tijekom procesa prijenosa, dok se uzorak nalazio na PDMS podlozi, AFM karakterizacija otkriva pojavu pukotina i dodatnih nabora, vidljivih i nakon prijenosa na konačni substrat. Nakon prijenosa na Ir(111) uzorak je vraćen u UHV i okarakteriziran LEED-om i STM-om. Iz tih mjerenja i dodatnih DFT simulacija, zaključujemo da je MoS$_2$ monosloj slabo vezan s podlogom, da se na uzorku javljaju dodatne nasumične korugacije, te da postoje barem dvije vrste atomskih defekata, čija gustoća varira na skalama od desetak nm [143].

Optička i elektronička svojstva dobivena iz PL, Raman i STS mjerenja ukazuju na elektronički procjep od 2.1 eV, i optički od 1.9 eV, te n-dopiranje [143]. Prateći PL i Raman signal u svakom koraku postupka prijenosa, dolazimo do zaključka da nakon podizanja uzorka sa podloge na kojoj je sintetiziran dolazi do oslobađanja od naprezanja, što je vidljivo u proširenju optičkog međuvrpčanog procjepa. No, nakon polaganja na Ir(111) podlogu dolazi do jakog gušenja PL i Raman signala, kao rezultat međudjelovanja s metalnom podlogom.

Nakon adsorpcije DNK tetraedara, AFM karakterizacija otkriva da je adsorbirani sloj znatno rjeđi nego u slučaju dva prethodna substrata, za iste parametre adsorpcije. STM otkriva da su po površini raspoređeni nasumično, a pretpostavljamo da su vezani disulfidnim skupinama na sumporne vakancije. Dodatno, došlo je do šesnaesterostrukog povećanja PL signala, dok je oblik spektra ostao nepromijenjen.

6 Zaključak

Motivacija za ovaj rad bila je izgradnja hibridnog sustava, koji se sastoji od 2D kristalne podloge i sloja biomakromolekula. Takvi sustavi se danas uvelike istražuju, jer ne samo da predstavljaju granicu između žive tvari i tehnologije, već imaju i mnoštvo potencijalnih primjena u nanotehnologiji kao senzori sa osjetljivošću na razini pojedine molekule ili kao dio bio-optoelektroničkih uređaja. Iako je konačni cilj ovog rada bio hibridni sustav koji se sastoji od 2D podloge (grafena ili monoslojnog MoS_2) i adsorbiranog sloja biomakromolekula, glavni fokus bio je na reproducibilnoj pripremi i opsežnoj karakterizaciji samih 2D nanopredložaka, budući da se kasnije mogu koristiti kao podloge za različite biomakromolekularne slojeve. U sklopu ovog rada ostvarena su dva hibridna sustava te su im struktura i svojstva istražena različitim eksperimentalnim tehnikama.

Prvi ostvareni hibridni sustav temelji se na grafenu naraštenom na Ir(111) podlozi što rezultira pojavom tzv. *moiré* efekta, heksagonalne superperiodičnosti sa konstantom rešetke od 2.5 nm. Cilj su nam bile zlatne nanočestice pošto se na njih mogu specifično vezati biomakromolekule funkcionalizirane sumporom. Da bi se postigla uređena matrica zlatnih nanočestica potrebno je prvo deponirati prekursore iridija, čime se dobiva uređena matrica AuIr kompozitnih nanoklastera koji se sastoje od $\approx$ 20 atoma, sa unutarnjom strukturom od Ir jezgre i Au ljuske. Rezultirajuća matrica AuIr klastera se pokazala stabilnom na izlaganje atmosferskim uvjetima i izlaganju tekućinama. Ipak, prilikom interkalacije grafena sa Cs ili Li atomima u UHV uvjetima dolazi do uništenja uređene strukture matrice. Nadalje, nakon prijenosa grafena na podlogu od SiO_2, nanočestice su u potpunosti uklonjene. Zbog činjenice da su klasteri pokazali nestabilnost s obzirom na transfer grafena, adsorpciju biomakromolekula bilo je moguće provesti samo na tek sintetiziranim nanopredlošcima, još uvijek na Ir(111) podlozi.

Uzimajući u obzir kemijski sastav podloga (površine koje sadrže zlato ili sumpor), biomakromolekule od interesa trebaju biti funkcionalizirane tiolnim skupinama, što su u našem slučaju DNA origami tetraedri s tiolnim skupinama na vrhovima. Iako su se DNA tetraedri adsorbirali na nanopredložak, to nije rezultiralo njihovim dugodosežnim lateralnim uređenjem. Pošto je ova podloga stabilna samo dok se nalazi na podlozi na kojoj je i sintetizirana, nije pogodna za daljnje primjene. No, kao predložak može koristiti u istraživanju vezanja i uređenja pojedinih biomakromolekula funkcionaliziranih sa skupinama koje mogu tvoriti tiolnu vezu prilikom adsorpcije.

Druga ispitivana 2D podloga je MoS_2 monosloj, koji je sintetiziran na silicij-

skoj podlozi te potom prenesen na površinu Ir(111) kristala za karakterizaciju na nanometarskoj skali. Pri svakom koraku postupka prijenosa monosloj je detaljno okarakteriziran, a na krajnjoj, iridijevoj podlozi istražen je do atomske razine. Ove procedure rezultirale su visokokvalitetnim MoS_2 monoslojem veličine reda milimetra i gustoćom defekata koja je usporediva s monoslojnim uzorcima dobivenim iz prirodnog MoS_2. Tijekom postupka prijenosa, neposredno nakon dizanja sa supstrata na kojem je sintetiziran, u uzorku dolazi do oslobođenja od naprezanja što rezultira proširenjem optičkog međuvrpčanog procjepa. Nakon prijenosa na Ir(111) površinu dolazi do jakog gušenja PL signala uzrokovanog interakcijom s metalnom podlogom. Međutim, nakon adsorpcije DNA tetraedra, dolazi do šesnaesterostrukog povećanja PL signala, bez promjene u obliku spektra. Ovo povećanje signala moglo bi se pripisati gušenju neradijativnih rekombinacijskih kanala. Ovo istraživanje doprinosi interdisciplinarnim istraživanjima između DNA nanotehnologije i 2D TMD tehnologije. Jak i stabilan PL signal uzrokovan atomskim defektima u MoS_2 ima potencijalne primjene u optoelektroničkim uređajima.

Bibliography

[1] R. Feynman, "There's plenty of room at the bottom," Eng. Sci. **23** (1960).

[2] E. K. Eigler and D. K. Schweizer, "Positioning single atoms with a scanning tunneling microscop," Nature **344**, 524–525 (1990).

[3] G. Moore, "Cramming more components onto integrated circuits," Electronics **38** (1965).

[4] A. P. Graham, G. S. Duesberg, R. V. Seidel, M. Liebau, E. Unger, W. Pamler, F. Kreupl, and W. Hoenlein, "Carbon nanotubes for microelectronics?" Small **1**, 382–390 (2005).

[5] C. Berger, Z. Song, T. Li, and X. Li, "Ultrathin epitaxial graphite: 2D electron gas properties and a route toward graphene-based nanoelectronics," J. Phys. Chem. B **108**, 1–5 (2004).

[6] K. S. Novoselov, a. K. Geim, S. V. Morozov, D. Jiang, Y. Zhang, S. V. Dubonos, I. V. Grigorieva, and a. a. Firsov, "Electric field effect in atomically thin carbon films." Science **306**, 666–9 (2004).

[7] R. E. Peierls, "Quelques propriétés typiques des corpses solides," Ann. Inst. H. Poincaré **5**, 177 (1935).

[8] L. D. Landau, "On the theory of phase transitions. II," Zh. Eksp. Teor. Fiz. **11**, 26 (1937).

[9] N. D. Mermin and H. Wagner, "Absence of ferromagnetism or antiferromagnetism in one- or two-dimensional isotropic Heisenberg models," Phys. Rev. Lett. **17**, 1133–1136 (1966).

[10] N. D. Mermin, "Crystalline Order in Two Dimensions," Phys. Rev. **176**, 250 (1968).

[11] J. Meyer, A. Geim, and M. Katsnelson, "The structure of suspended graphene sheets," Nature **4** (2007).

[12] M. Xu, T. Liang, M. Shi, and H. Chen, "Graphene-Like Two-Dimensional Materials," Chem. Rev. **113**, 3766–3798 (2013).

[13] H. S. Lee, S.-w. Min, Y.-g. Chang, M. K. Park, T. Nam, H. Kim, J. H. Kim, S. Ryu, and S. Im, "MoS 2 Nanosheet Phototransistors with Thickness-Modulated Optical Energy Gap," Nano Lett. **12**, 3695–3700 (2012).

[14] Z. Wang, W. Zhu, Y. Qiu, X. Yi, A. V. Bussche, A. Kane, H. Gao, K. Koski, and R. Hurt, "Biological and environmental interactions of emerging two-dimensional nanomaterials," Chem. Soc. Rev. **45**, 1750–1780 (2016).

[15] Y. Zhang, L. Zhang, and C. Zhou, "Review of chemical vapor deposition of graphene and related applications," Acc. Chem. Res. **46**, 2329–2339 (2013).

[16] M. J. Allen, V. C. Tung, and R. B. Kaner, "Honeycomb carbon: A review of graphene," Chem. Rev. **110**, 132–145 (2010).

[17] C. Qin, Y. Gao, Z. Qiao, L. Xiao, and S. Jia, "Atomic-Layered MoS2 as a Tunable Optical Platform," Adv. Opt. Mater. **4**, 1429–1456 (2016).

[18] Q. H. Wang, K. Kalantar-Zadeh, A. Kis, J. N. Coleman, and M. S. Strano, "Electronics and optoelectronics of two-dimensional transition metal dichalcogenides," Nat. Nanotechnol. **7**, 699–712 (2012).

[19] J. Wilson and A. Yoffe, "The transition metal dichalcogenides discussion and interpretation of the observed optical, electrical and structural properties," Adv. Phys. **18**, 193–335 (1969).

[20] A. D. Yoffe, "Layer Compounds," Annu. Rev. Mater. Sci. **3**, 147–170 (1973).

[21] A. K. Geim and K. S. Novoselov, "The rise of graphene." Nat. Mater. **6**, 183–91 (2007).

[22] K. S. Novoselov, A. K. Geim, S. V. Morozov, D. Jiang, M. I. Katsnelson, I. V. Grigorieva, S. V. Dubonos, and a. a. Firsov, "Two-dimensional gas of massless Dirac fermions in graphene." Nature **438**, 197–200 (2005).

[23] M. S. Toshiaki Enoki, Morinobu Endo, *Graphite intercalation compounds and applications* (Oxford University Press, 2003).

[24] K. I. Bolotin, K. J. Sikes, J. Hone, H. L. Stormer, and P. Kim, "Temperature-Dependent Transport in Suspended Graphene," Phys. Rev. Lett. **101**, 1–4 (2008).

[25] A. Geim, "Graphene: status and prospects," Science **324**, 1530–1534 (2009).

[26] K. A and M. N. H, *Strong Solids 3rd edition* (Oxford: Clarendon Press, 1986).

[27] F. Liu, P. Ming, and J. Li, "Ab initio," Phys. Rev. B **76**, 064120 (2007).

[28] Y. Shao, J. Wang, H. Wu, J. Liu, I. A. Aksay, and Y. Lin, "Graphene based electrochemical sensors and biosensors: A review," Electroanalysis **22**, 1027–1036 (2010).

[29] A. Varykhalov and O. Rader, "Graphene grown on Co(0001) films and islands: Electronic structure and its precise magnetization dependence," Phys. Rev. B **80**, 6–11 (2009).

[30] L. Zhao, K. Rim, H. Zhou, and R. He, "The Atomic-scale growth of large-area monolayer graphene on single-crystal copper substrates," Arxiv Prepr. arXiv . . . (2010).

[31] J. Coraux, A. T. N'Diaye, C. Busse, and T. Michely, "Structural coherency of graphene on Ir(111)." Nano Lett. **8**, 565–70 (2008).

[32] D. Usachov, A. Dobrotvorskii, A. Varykhalov, O. Rader, W. Gudat, A. Shikin, and V. Adamchuk, "Experimental and theoretical study of the morphology of commensurate and incommensurate graphene layers on Ni single-crystal surfaces," Phys. Rev. B **78**, 1–8 (2008).

[33] S.-Y. Kwon, C. V. Ciobanu, V. Petrova, V. B. Shenoy, J. Bareño, V. Gambin, I. Petrov, and S. Kodambaka, "Growth of semiconducting graphene on palladium." Nano Lett. **9**, 3985–90 (2009).

[34] P. Sutter, J. T. Sadowski, and E. Sutter, "Graphene on Pt(111): Growth and substrate interaction," Phys. Rev. B **80**, 1–10 (2009).

[35] P. W. Sutter, J.-I. Flege, and E. A. Sutter, "Epitaxial graphene on ruthenium." Nat. Mater. **7**, 406–11 (2008).

[36] K. V. Emtsev, A. Bostwick, K. Horn, J. Jobst, G. L. Kellogg, L. Ley, J. L. McChesney, T. Ohta, S. a. Reshanov, J. Röhrl, E. Rotenberg, A. K. Schmid, D. Waldmann, H. B. Weber, and T. Seyller, "Towards wafer-size graphene layers by atmospheric pressure graphitization of silicon carbide." Nat. Mater. **8**, 203–7 (2009).

[37] J. Coraux, A. T N'Diaye, M. Engler, C. Busse, D. Wall, N. Buckanie, F.-J. Meyer zu Heringdorf, R. van Gastel, B. Poelsema, and T. Michely, "Growth of graphene on Ir(111)," New J. Phys. **11**, 023006 (2009).

[38] S. Stankovich, D. A. Dikin, R. D. Piner, K. A. Kohlhaas, A. Kleinhammes, Y. Jia, Y. Wu, S. T. Nguyen, and R. S. Ruoff, "Synthesis of graphene-based nanosheets via chemical reduction of exfoliated graphite oxide," Carbon **45**, 1558 – 1565 (2007).

[39] N. A. Kumar, S. Gambarelli, F. Duclairoir, G. Bidan, and L. Dubois, "Synthesis of high quality reduced graphene oxide nanosheets free of paramagnetic metallic impurities," J. Mater. Chem. A **1**, 2789–2794 (2013).

[40] A. N'Diaye, S. Bleikamp, P. Feibelman, and T. Michely, "Two-Dimensional Ir Cluster Lattice on a Graphene Moir{é} on Ir(111)," Phys. Rev. Lett. **97**, 1–4 (2006).

[41] A. T. N'Diaye, J. Coraux, T. N. Plasa, C. Busse, and T. Michely, "Structure of epitaxial graphene on Ir(111)," New J. Phys. **10**, 043033 (2008).

[42] A. T. N'Diaye, T. Gerber, C. Busse, J. Mysliveček, J. Coraux, and T. Michely, "A versatile fabrication method for cluster superlattices," New J. Phys. **11**, 103045 (2009).

[43] P. Feibelman, "Pinning of graphene to Ir(111) by flat Ir dots," Phys. Rev. B **77**, 1–7 (2008).

[44] B. Sipos, A. F. Kusmartseva, A. Akrap, H. Berger, L. Forró, and E. Tutiš, "From Mott state to superconductivity in 1T-TaS2," Nat. Mater. **7**, 960–965 (2008).

[45] A. H. Castro Neto, "Charge Density Wave, Superconductivity, and Anomalous Metallic Behavior in 2D Transition Metal Dichalcogenides," Phys. Rev. Lett. **86**, 4382–4385 (2001).

[46] T. Ando, A. B. Fowler, and F. Stern, "Electronic properties of two-dimensional systems," Rev. Mod. Phys. **54**, 437–672 (1982).

[47] B. K. Ridley, "The electron-phonon interaction in quasi-two-dimensional semiconductor quantum-well structures," Journal of Physics C: Solid State Physics **15**, 5899–5197 (1982).

[48] Q. Wang, P. Wu, G. Cao, and M. Huang, "First-principles study of the structural and electronic properties of MoS2–WS2 and MoS2–MoTe2 monolayer heterostructures," J. Phys. D. Appl. Phys. **46**, 505308 (2013).

[49] P. a. Young, "Lattice parameter measurements on molybdenum disulphide," J. Phys. D. Appl. Phys. **1**, 936–938 (1968).

[50] R. Addou, L. Colombo, and R. M. Wallace, "Surface Defects on Natural MoS 2," ACS Appl. Mater. Interfaces **7**, 11921–11929 (2015).

[51] K. F. Mak, C. Lee, J. Hone, J. Shan, and T. F. Heinz, "Atomically thin MoS2: A new direct-gap semiconductor," Phys. Rev. Lett. **105**, 2–5 (2010).

[52] A. Splendiani, L. Sun, Y. Zhang, T. Li, J. Kim, C. Y. Chim, G. Galli, and F. Wang, "Emerging photoluminescence in monolayer MoS2," Nano Lett. **10**, 1271–1275 (2010).

[53] D. Y. Qiu, F. H. da Jornada, and S. G. Louie, "Optical Spectrum of MoS$_2$: Many-Body Effects and Diversity of Exciton States," Phys. Rev. Lett. **111**, 216805 (2013).

[54] K. F. Mak, K. He, C. Lee, G. H. Lee, J. Hone, T. F. Heinz, and J. Shan, "Tightly bound trions in monolayer MoS2." Nat. Mater. **12**, 207–11 (2013).

[55] S. S. Singha, D. Nandi, and A. Singha, "Tuning the photoluminescence and ultrasensitive trace detection properties of few-layer MoS2 by decoration with gold nanoparticles," RSC Adv. **5**, 24188–24193 (2015).

[56] M. Amani, D.-H. Lien, D. Kiriya, J. Xiao, A. Azcatl, J. Noh, S. R. Madhvapathy, R. Addou, S. KC, M. Dubey, K. Cho, R. M. Wallace, S.-C. Lee, J.-H. He, J. W. Ager, X. Zhang, E. Yablonovitch, and A. Javey, "Near-unity photoluminescence quantum yield in Mo2," Science (80-.). **350**, 1065 LP – 1068 (2015).

[57] S. Tongay, J. Suh, C. Ataca, W. Fan, A. Luce, J. S. Kang, J. Liu, C. Ko, R. Raghunathanan, J. Zhou, F. Ogletree, J. Li, J. C. Grossman, and J. Wu, "Defects activated photoluminescence in two-dimensional semiconductors: interplay between bound, charged, and free excitons," Sci. Rep. **3**, 2657 (2013).

[58] H. J. Conley, B. Wang, J. I. Ziegler, R. F. Haglund, S. T. Pantelides, and K. I. Bolotin, "Bandgap Engineering of Strained Monolayer and Bilayer MoS2," Nano Lett. **13**, 3626–3630 (2013).

[59] S. Tongay, J. Zhou, C. Ataca, J. Liu, J. S. Kang, T. S. Matthews, L. You, J. B. Li, J. C. Grossman, and J. Q. Wu, "Broad-Range Modulation of Light Emission in Two-Dimensional Semiconductors by Molecular Physisorption Gating," Nano Lett **13**, 2831–2836 (2013).

[60] B. Cho, M. G. Hahm, M. Choi, J. Yoon, A. R. Kim, Y.-J. Lee, S.-G. Park, J.-D. Kwon, C. S. Kim, M. Song, Y. Jeong, K.-S. Nam, S. Lee, T. J. Yoo, C. G. Kang, B. H. Lee, H. C. Ko, P. M. Ajayan, and D.-H. Kim, "Charge-transfer-based Gas Sensing Using Atomic-layer MoS2," Sci. Rep. **5**, 8052 (2015).

[61] S. Bertolazzi, J. Brivio, and A. Kis, "Stretching and breaking of ultrathin MoS 2," ACS Nano **5**, 9703–9709 (2011).

[62] K. He, C. Poole, K. F. Mak, and J. Shan, "Experimental demonstration of continuous electronic structure tuning via strain in atomically thin MoS2," Nano Lett. **13**, 2931–2936 (2013).

[63] M. Buscema, G. A. Steele, H. S. J. van der Zant, and A. Castellanos-Gomez, "The effect of the substrate on the Raman and photoluminescence emission of single layer MoS2," Nano Res. **7**, 561–571 (2014).

[64] H. Zeng, J. Dai, W. Yao, D. Xiao, and X. Cui, "Valley polarization in MoS2 monolayers by optical pumping," Nat. Nanotechnol. **7**, 490–493 (2012).

[65] N. C. Seeman, "Nucleic acid junctions and lattices," J. Theor. Biol. **99**, 237–247 (1982).

[66] B. Saccà and C. M. Niemeyer, "DNA Origami: The Art of Folding DNA," Angew. Chemie Int. Ed. **51**, 58–66 (2012).

[67] N. C. Seeman, "DNA in a material world," Nature **421**, 427–431 (2003).

[68] P. W. K. Rothemund, "Folding DNA to create nanoscale shapes and patterns." Nature **440**, 297–302 (2006).

[69] C. E. Castro, F. Kilchherr, D.-N. Kim, E. L. Shiao, T. Wauer, P. Wortmann, M. Bathe, and H. Dietz, "A primer to scaffolded DNA origami," Nat. Methods **8**, 221–229 (2011).

[70] Y. Lu, B. R. Goldsmith, N. J. Kybert, and a. T. C. Johnson, "DNA-decorated graphene chemical sensors," Appl. Phys. Lett. **97**, 8–11 (2010).

[71] H.-Y. Park, S. R. Dugasani, D.-H. Kang, J. Jeon, S. K. Jang, S. Lee, Y. Roh, S. H. Park, and J.-H. Park, "n- and p- Type Doping Phenomenon by Artificial DNA and M - DNA on Two-Dimensional Transition Metal Dichalcogenides," ACS Nano **8**, 11603–13 (2014).

[72] A. Rakitin, P. Aich, C. Papadopoulos, Y. Kobzar, a. Vedeneev, J. Lee, and J. Xu, "Metallic Conduction through Engineered DNA: DNA Nanoelectronic Building Blocks," Phys. Rev. Lett. **86**, 3670–3673 (2001).

[73] M. G. Warner and J. E. Hutchison, "Linear assemblies of nanoparticles electrostatically organized on DNA scaffolds." Nat. Mater. **2**, 272–7 (2003).

[74] M. Mrksich and G. M. Whitesides, "Using self-assembled monolayers to understand the interactions of man-made surfaces with proteins and cells," Annu. Rev. Biophys. Biomol. Struct. **25**, 55–78 (1996).

[75] G. M. Whitesides, J. K. Kriebel, and J. C. Love, "Molecular engineering of surfaces using self-assembled monolayers," Sci. Prog. **88**, 17–48 (2005).

[76] A. Sassolas, B. D. Leca-Bouvier, and L. J. Blum, "DNA biosensors and microarrays." Chem. Rev. **108**, 109–39 (2008).

[77] K. M. Blocker, K. L. Kiick, and M. O. Sullivan, "Surface Immobilization of Plasmid DNA with a Cell-Responsive Tether for Substrate-Mediated Gene Delivery," Langmuir **27**, 2739–2746 (2011).

[78] H. Häkkinen, "The gold–sulfur interface at the nanoscale," Nat. Chem. **4**, 443–455 (2012).

[79] W. J. Arnoult and R. B. McLellan, "The solubility of carbon in rhodium, ruthenium, iridium and rhenium," Scripta Metallurgica **6**, 1013 (1972).

[80] G. Binnig, H. Rohrer, C. Gerber, and E. Weibel, "7x 7 reconstruction on Si (111) resolved in real space," Phys. Rev. Lett. **50** (1983).

[81] G. Binnig and H. Rohrer, "Scanning tunneling microscopy—from birth to adolescence," Rev. Mod. Phys. **59**, 615–625 (1987).

[82] M. C. Desjonqueres and D. Spanjaard, *Concepts in Surface Physics* (Springer-Verlag, Berlin, 1996).

[83] J. Tersoff and D. Hamann, "Theory and application for the scanning tunneling microscope," Phys. Rev. Lett. **50**, 1998–2001 (1983).

[84] J. Tersoff and D. Hamann, "Theory of the scanning tunneling microscope," Phys. Rev. B **31**, 805–813 (1985).

[85] C. J. Chen, *Introduction to Scanning Tunneling Microscopy Second Edition* (Oxford university press, 1993).

[86] K. Besocke, "An easily operable scanning tunneling microscope," Surf. Sci. **181**, 145–153 (1987).

[87] M. Wilms, M. Schmidt, G. Bermes, and K. Wandelt, "New and versatile ultrahigh vacuum scanning tunneling microscope for film growth experiments," Rev. Sci. Instrum. **69**, 2696 (1998).

[88] I. Horcas, R. Fernández, J. M. Gómez-Rodríguez, J. Colchero, J. Gómez-Herrero, and A. M. Baro, "WSXM: A software for scanning probe microscopy and a tool for nanotechnology," Rev. Sci. Instrum. **78** (2007).

[89] D. Nečas and P. Klapetek, "Gwyddion: an open-source software for SPM data analysis," Open Phys. **10** (2012).

[90] Y. Wang, Y. Zheng, X. Xu, E. Dubuisson, Q. Bao, J. Lu, and K. P. Loh, "Electrochemical delamination of CVD-grown graphene film: Toward the recyclable use of copper catalyst," ACS Nano **5**, 9927–9933 (2011).

[91] L. Gao, W. Ren, H. Xu, L. Jin, Z. Wang, T. Ma, L.-P. Ma, Z. Zhang, Q. Fu, L.-M. Peng, X. Bao, and H.-M. Cheng, "Repeated growth and bubbling transfer of graphene with millimetre-size single-crystal grains using platinum," Nat. Commun. **3**, 699 (2012).

[92] E. Koren, E. Sutter, S. Bliznakov, F. Ivars-Barcelo, and P. Sutter, "Isolation of high quality graphene from Ru by solution phase intercalation," Appl. Phys. Lett. **103** (2013).

[93] P. Gupta, P. D. Dongare, S. Grover, S. Dubey, H. Mamgain, A. Bhattacharya, and M. M. Deshmukh, "A facile process for soak-and-peel delamination of CVD graphene from substrates using water," Sci. Rep. , 1–6 (2013).

[94] C. T. Cherian, F. Giustiniano, I. Martin-Fernandez, H. Andersen, J. Balakrishnan, and B. Özyilmaz, "'Bubble-free' electrochemical delamination of CVD graphene films," Small **11**, 189–194 (2015).

[95] A. Castellanos-Gomez, M. Buscema, R. Molenaar, V. Singh, L. Janssen, H. S. J. van der Zant, and G. A. Steele, "Deterministic transfer of two-dimensional materials by all-dry viscoelastic stamping," 2D Mater. **1**, 011002 (2014).

[96] H. Li, J. Wu, X. Huang, Z. Yin, J. Liu, and H. Zhang, "A universal, rapid method for clean transfer of nanostructures onto various substrates," ACS Nano **8**, 6563–6570 (2014).

[97] A. Gurarslan, Y. Yu, L. Su, Y. Yu, F. Suarez, S. Yao, Y. Zhu, M. Ozturk, Y. Zhang, and L. Cao, "Surface-Energy-Assisted Perfect Transfer of Centimeter-Scale Monolayer and Few-Layer MoS2 Films onto Arbitrary Substrates," ACS Nano , 11522–11528 (2014).

[98] R. P. Goodman, R. M. Berry, and A. J. Turberfield, "The single-step synthesis of a DNA tetrahedron." Chem. Commun. (Camb). **44**, 1372–1373 (2004).

[99] N. Mitchell, R. Schlapak, M. Kastner, D. Armitage, W. Chrzanowski, J. Riener, P. Hinterdorfer, A. Ebner, and S. Howorka, "A DNA nanostructure for the functional assembly of chemical groups with tunable stoichiometry and defined nanoscale geometry." Angew. Chem. Int. Ed. Engl. **48**, 525–7 (2009).

[100] M. Leitner, N. Mitchell, M. Kastner, R. Schlapak, H. J. Gruber, P. Hinterdorfer, S. Howorka, and A. Ebner, "Single-Molecule AFM Characterization of Individual Chemically Tagged DNA Tetrahedra," ACS Nano **5**, 7048–7054 (2011).

[101] G. Binnig, C. Quate, and C. Gerber, "Atomic force microscope," Phys. Rev. Lett. **56**, 930–933 (1986).

[102] F. Giessibl, "Advances in atomic force microscopy," Rev. Mod. Phys. **75** (2003).

[103] Á. S. Paulo and R. García, "Unifying theory of tapping-mode atomic-force microscopy," Phys. Rev. B **66**, 41406 (2002).

[104] Á. Paulo and R. García, "Tip-surface forces, amplitude, and energy dissipation in amplitude-modulation (tapping mode) force microscopy," Phys. Rev. B **64**, 193411 (2001).

[105] I. Casuso, F. Rico, and S. Scheuring, "Biological AFM: where we come from–where we are–where we may go." J. Mol. Recognit. **24**, 406–13 (2011).

[106] C. Barth, A. S. Foster, C. R. Henry, and A. L. Shluger, "Recent trends in surface characterization and chemistry with high-resolution scanning force methods." Adv. Mater. **23**, 477–501 (2011).

[107] M. Rodahl, F. Höök, A. Krozer, P. Brzezinski, and B. Kasemo, "Quartz crystal microbalance setup for frequency and Q-factor measurements in gaseous and liquid environments," Rev. Sci. Instrum. **66**, 3924–3930 (1995).

[108] F. Hook, B. Kasemo, T. Nylander, C. Fant, K. Sott, and H. Elwing, "Variations in coupled water, viscoelastic properties, and film thickness of a Mefp-1 protein film during adsorption and cross-linking: A quartz crystal microbalance with dissipation monitoring, ellipsometry, and surface plasmon resonance study," Anal. Chem. **73**, 5796–5804 (2001).

[109] G. Sauerbrey, "Verwendung von Schwingquarzen zur Wägung dünner Schichten und zur Mikrowägung," Z. Phys. , 206–222.

[110] M. Griebel, S. Knapek, and G. Zumbusch, "Numerical Simulation in Molecular Dynamics: Numerics, Algorithms, Parallelization, Applications (Texts in Computational Science and Engineering)," Springer, September **2**, 1–3 (2007).

[111] J. Schneider, J. Hamaekers, S. T. Chill, S. Smidstrup, J. Bulin, R. Thesen, A. Blom, and K. Stokbro, "ATK-ForceField: A New Generation Molecular Dynamics Software Package," ArXiv e-prints (2017).

[112] M. P. Allen and D. J. Tildesley, *Computer simulation of liquids* (Oxford university press, 1989).

[113] G. Kresse and J. Hafner, "Ab initio molecular dynamics for liquid metals," Phys. Rev. B **47**, 558–561 (1993).

[114] G. Kresse and J. Furthmüller, "Efficient iterative schemes for ab initio total-energy calculations using a plane-wave basis set," Phys. Rev. B **54**, 11169–11186 (1996).

[115] G. Kresse and D. Joubert, "From ultrasoft pseudopotentials to the projector augmented-wave method," Phys. Rev. B **59**, 1758–1775 (1999).

[116] J. c. v. Klimeš, D. R. Bowler, and A. Michaelides, "Van der Waals density functionals applied to solids," Phys. Rev. B **83**, 195131 (2011).

90

[117] M. Dion, H. Rydberg, E. Schröder, D. C. Langreth, and B. I. Lundqvist, "Van der Waals density functional for general geometries," Phys. Rev. Lett. **92**, 246401–1 (2004).

[118] G. Román-Pérez and J. M. Soler, "Efficient Implementation of a van der Waals Density Functional: Application to Double-Wall Carbon Nanotubes," Phys. Rev. Lett. **103**, 096102 (2009).

[119] J. Klimeš, D. R. Bowler, and A. Michaelides, "Chemical accuracy for the van der Waals density functional," Journal of Physics: Condensed Matter **22**, 022201 (2010).

[120] H. Li, Q. Zhang, C. C. R. Yap, B. K. Tay, T. H. T. Edwin, A. Olivier, and D. Baillargeat, "From bulk to monolayer MoS 2: Evolution of Raman scattering," Adv. Funct. Mater. **22**, 1385–1390 (2012).

[121] A. Kumar and P. K. Ahluwalia, "Electronic structure of transition metal dichalcogenides monolayers 1H-MX2 (M = Mo, W; X = S, Se, Te) from ab-initio theory: new direct band gap semiconductors," The European Physical Journal B **85**, 186 (2012).

[122] P. Johari and V. B. Shenoy, "Tuning the Electronic Properties of Semiconducting Transition Metal Dichalcogenides by Applying Mechanical Strains," ACS Nano **6**, 5449–5456 (2012), pMID: 22591011.

[123] E. S. Kadantsev and P. Hawrylak, "Electronic structure of a single MoS2 monolayer," Solid State Communications **152**, 909 – 913 (2012).

[124] J.-Y. Noh, H. Kim, and Y.-S. Kim, "Stability and electronic structures of native defects in single-layer MoS_2," Phys. Rev. B **89**, 205417 (2014).

[125] H.-P. Komsa and A. V. Krasheninnikov, "Native defects in bulk and monolayer MoS_2 from first principles," Phys. Rev. B **91**, 125304 (2015).

[126] P. Eckerlin and H. e. Kandler, *Group III: Condensed Matter (Landolt-Brönstein: Numerical Data and Functional Relationships in Science and Technology - New Series)*, Vol. 6 (Berlin: Springer, 1971).

[127] I. Pletikosić, M. Kralj, D. Sokčević, R. Brako, P. Lazić, and P. Pervan, "Photoemission and density functional theory study of Ir(111); energy band gap mapping." J. Phys. Condens. Matter **22**, 135006 (2010).

[128] W. Chen, E. J. G. Santos, W. Zhu, E. Kaxiras, and Z. Zhang, "Tuning the Electronic and Chemical Properties of Monolayer MoS2 Adsorbed on Transition Metal Substrates," Nano Letters **13**, 509–514 (2013), pMID: 23320793.

[129] C. Gong, L. Colombo, R. M. Wallace, and K. Cho, "The Unusual Mechanism of Partial Fermi Level Pinning at Metal–MoS2 Interfaces," Nano Letters **14**, 1714–1720 (2014), pMID: 24660782.

[130] M. Hegner, P. Wagner, and G. Semenza, "Ultralarge atomically flat template-stripped Au surfaces for scanning probe microscopy," Surf. Sci. **291**, 39–46 (1993).

[131] P. Hansma, V. Elings, O. Marti, and C. Bracker, "Scanning tunneling microscopy and atomic force microscopy: application to biology and technology," Science (80-.). **242**, 209–216 (1988).

[132] A. Martinez-Galera, I. Brihuega, J. M. Gomez-Rodriguez, A. J. Martínez-Galera, I. Brihuega, and J. M. Gómez-Rodríguez, "Influence of the Rotational Domain in the Growth of Transition Metal Clusters on Graphene," J. Phys. Chem. C **119**, 3572–3578 (2015).

[133] M. Petrović, J. T. Sadowski, A. Šiber, and M. Kralj, "Wrinkles of graphene on Ir(1 1 1): Macroscopic network ordering and internal multi-lobed structure," Carbon N. Y. **94**, 856–863 (2015).

[134] A. P. Sutton and J. Chen, "Long-range Finnis–Sinclair potentials," Philos. Mag. Lett. **61**, 139–146 (1990).

[135] H. Rafii-Tabar and A. P. Sulton, "Long-range Finnis-Sinclair potentials for f.c.c. metallic alloys," Philos. Mag. Lett. **63**, 217–224 (1991).

[136] Y. Kimura, Y. Qi, T. Cagin, and W. Goddard III, "The quantum Sutton-Chen many-body potential for properties of fcc metals," Phys. Rev., (1998).

[137] J. P. K. Doye and D. J. Wales, "Global minima for transition metal clusters described by Sutton-Chen potentials," New J. Chem. **22**, 733–744 (1998).

[138] I. Delač Marion, D. Čapeta, P. Lazić, I. Lončarić, R. K. Trivedi, M. Buljan, T. Vuletić, and M. Kralj, "Exploring 2D materials based nanotemplates for biomolecular arrays," in preparation. ().

[139] A. J. Martínez-Galera, I. Brihuega, A. Gutiérrez-Rubio, T. Stauber, and J. M. Gómez-Rodríguez, "Towards scalable nano-engineering of graphene," Sci. Rep. 4, 7314 (2015).

[140] T. Gerber, E. Grånäs, U. A. Schröder, P. Stratmann, K. Schulte, J. N. Andersen, J. Knudsen, and T. Michely, "Stability and Reactivity of Graphene-templated Nanoclusters," J. Phys. Chem. C , acs.jpcc.6b07828 (2016).

[141] M. Petrovic, I. S. Rakic, S. Runte, C. Busse, J. T. Sadowski, P. Lazic, I. Pletikosic, Z. H. Pan, M. Milun, P. Pervan, N. Atodiresei, R. Brako, D. Sokcevic, T. Valla, T. Michely, and M. Kralj, "The mechanism of caesium intercalation of graphene," Nat. Commun. 4, 2772 (2013).

[142] M. Buljan, private communication.

[143] I. Delač Marion, D. Čapeta, B. Pielić, F. Faraguna, A. Gallardo, P. Pou, B. Biel, N. Vujičić, and M. Kralj, "Characterization of atomic-scale defects and electronic properties of chemically grown MoS2 monolayer," in preparation. ().

[144] A. Hashimoto, K. Suenaga, A. Gloter, K. Urita, and S. Iijima, "Direct evidence for atomic defects in graphene layers." Nature 430, 870–3 (2004).

[145] J. C. Meyer, C. Kisielowski, R. Erni, M. D. Rossell, M. F. Crommie, and A. Zettl, "Direct imaging of lattice atoms and topological defects in graphene membranes," Nano Lett. 8, 3582–3586 (2008).

[146] J. Hong, Z. Hu, M. Probert, K. Li, D. Lv, X. Yang, L. Gu, N. Mao, Q. Feng, L. Xie, J. Zhang, D. Wu, Z. Zhang, C. Jin, W. Ji, X. Zhang, J. Yuan, and Z. Zhang, "Exploring atomic defects in molybdenum disulphide monolayers." Nat. Commun. 6, 6293 (2015).

[147] H. P. Komsa, J. Kotakoski, S. Kurasch, O. Lehtinen, U. Kaiser, and A. V. Krasheninnikov, "Two-dimensional transition metal dichalcogenides under electron irradiation: Defect production and doping," Phys. Rev. Lett. 109, 1–5 (2012).

[148] E. Stolyarova, K. T. Rim, S. Ryu, J. Maultzsch, P. Kim, L. E. Brus, T. F. Heinz, M. S. Hybertsen, and G. W. Flynn, "High-resolution scanning tunneling microscopy imaging of mesoscopic graphene sheets on an insulating surface," Proc. Natl. Acad. Sci. 104, 9209–9212 (2007).

[149] M. Ishigami, J. Chen, W. Cullen, M. Fuhrer, and E. Williams, "Atomic Structure of Graphene on SiO2," Nano Lett. **7**, 1–13 (2007).

[150] X. Liu, I. Balla, H. Bergeron, and M. C. Hersam, "Point Defects and Grain Boundaries in Rotationally Commensurate MoS2 on Epitaxial Graphene," J. Phys. Chem. C **120**, 20798–20805 (2016).

[151] G. Z. Magda, J. Pető, G. Dobrik, C. Hwang, L. P. Biró, and L. Tapasztó, "Exfoliation of large-area transition metal chalcogenide single layers," Sci. Rep. **5**, 14714 (2015).

[152] K. Kobayashi and J. Yamauchi, "Electronic structure and scanning-tunneling-microscopy image of molybdenum dichalcogenide surfaces," Phys. Rev. B **51**, 17085–17095 (1995).

[153] P. Vancso, G. Z. Magda, J. Peto, J. Y. Noh, Y. S. Kim, C. Hwang, L. P. Biro, and L. Tapaszto, "The intrinsic defect structure of exfoliated MoS2 single layers revealed by Scanning Tunneling Microscopy," Sci. Rep. **6**, 7 (2016).

[154] Y. Yu, Y. Yu, C. Xu, Y. Q. Cai, L. Su, Y. Zhang, Y. W. Zhang, K. Gundogdu, and L. Cao, "Engineering Substrate Interactions for High Luminescence Efficiency of Transition-Metal Dichalcogenide Monolayers," Adv. Funct. Mater. , 1–7 (2016).

[155] Z. Liu, M. Amani, S. Najmaei, Q. Xu, X. Zou, W. Zhou, T. Yu, C. Qiu, A. G. Birdwell, F. J. Crowne, R. Vajtai, B. I. Yakobson, Z. Xia, M. Dubey, P. M. Ajayan, and J. Lou, "Strain and structure heterogeneity in MoS2 atomic layers grown by chemical vapour deposition," Nat. Commun. **5**, 5246 (2014).

[156] A. Castellanos-gomez, R. Roldán, and E. Cappelluti, "Local strain engineering in atomically thin MoS 2," Nano Lett. **13**, 5361–5366 (2013).

[157] A. Castellanos-Gomez, J. Quereda, H. P. van der Meulen, N. Agrait, and G. Rubio-Bollinger, "Spatially resolved optical absorption spectroscopy of single- and few-layer MoS2 by hyperspectral imaging," Nanotechnology **27**, 5 (2016).

[158] J. Kim, L. J. Cote, F. Kim, and J. Huang, "Visualizing graphene based sheets by fluorescence quenching microscopy," J. Am. Chem. Soc. **132**, 260–267 (2010).

[159] L. Gaudreau, K. J. Tielrooij, G. E. D. K. Prawiroatmodjo, J. Osmond, F. J. G. De Abajo, and F. H. L. Koppens, "Universal distance-scaling of nonradiative energy transfer to graphene," Nano Lett. **13**, 2030–2035 (2013).

[160] A. Sagar, K. Kern, and K. Balasubramanian, "Marker-free on-the-fly fabrication of graphene devices based on fluorescence quenching." Nanotechnology **21**, 015303 (2010).

[161] Chen Z, Berciaud S, Nuckolls C, Heinz T F, "Energy Transfer from Individual Semiconductor Nanocrystals to Graphene.pdf," ACS Nano **4**, 1–5.

[162] C. Rice, R. J. Young, R. Zan, U. Bangert, D. Wolverson, T. Georgiou, R. Jalil, and K. S. Novoselov, "Raman-scattering measurements and first-principles calculations of strain-induced phonon shifts in monolayer MoS2," Phys. Rev. B - Condens. Matter Mater. Phys. **87**, 1–5 (2013).

[163] B. Chakraborty, A. Bera, D. V. S. Muthu, S. Bhowmick, U. V. Waghmare, and A. K. Sood, "Symmetry-dependent phonon renormalization in monolayer MoS 2 transistor," Phys. Rev. B - Condens. Matter Mater. Phys. **85**, 2–5 (2012).

[164] Y. Y. Hui, X. Liu, W. Jie, N. Y. Chan, J. Hao, Y.-T. Hsu, L.-J. Li, W. Guo, and S. P. Lau, "Exceptional Tunability of Band Energy in a Compressively Strained Trilayer MoS2 Sheet," ACS Nano **7**, 7126–7131 (2013).

[165] E. Starodub, A. Bostwick, L. Moreschini, S. Nie, F. El Gabaly, K. F. McCarty, and E. Rotenberg, "In-plane orientation effects on the electronic structure, stability, and Raman scattering of monolayer graphene on Ir(111)," Phys. Rev. B **83**, 125428 (2011).

[166] R. Brako, D. Šokčević, P. Lazić, and N. Atodiresei, "Graphene on the Ir(111) surface: From van der Waals to strong bonding," New J. Phys. **12** (2010).

[167] Y. Murata, E. Starodub, B. B. Kappes, C. V. Ciobanu, N. C. Bartelt, K. F. McCarty, and S. Kodambaka, "Orientation-dependent work function of graphene on Pd(111)," Appl. Phys. Lett. **97**, 21–24 (2010).

[168] Q. Zhou, S. Coh, M. L. Cohen, S. G. Louie, and A. Zettl, "Imprint of transition metal d orbitals on a graphene Dirac cone," Phys. Rev. B - Condens. Matter Mater. Phys. **88**, 1–5 (2013).

[169] R. Feenstra, J. a. Stroscio, and A. Fein, "Tunneling spectroscopy of the Si(111)2x1 surface," Surf. Sci. **181**, 295–306 (1987).

[170] H. M. Hill, A. F. Rigosi, C. Roquelet, A. Chernikov, T. C. Berkelbach, D. R. Reichman, M. S. Hybertsen, L. E. Brus, and T. F. Heinz, "Observation of excitonic Rydberg states in monolayer MoS2 and WS2 by photoluminescence excitation spectroscopy," Nano Lett. **15**, 2992–2997 (2015).

[171] Z. Yu, Y. Pan, Y. Shen, Z. Wang, Z.-Y. Ong, T. Xu, R. Xin, L. Pan, B. Wang, L. Sun, J. Wang, G. Zhang, Y. W. Zhang, Y. Shi, and X. Wang, "Towards intrinsic charge transport in monolayer molybdenum disulfide by defect and interface engineering," Nat. Commun. **5**, 5290 (2014).

[172] H. Nan, Z. Wang, W. Wang, Z. Liang, Y. Lu, Q. Chen, D. He, P. Tan, F. Miao, X. Wang, J. Wang, and Z. Ni, "Strong photoluminescence enhancement of MoS2 through defect engineering and oxygen bonding," ACS Nano **8**, 5738–5745 (2014).

Curriculum vitae

Ida Delač Marion was born on November 15, 1986 in Zagreb, Croatia. In 2010 she obtained her Master's degree in Physics from the Department of Physics, Faculty of Science of the University of Zagreb in Croatia. Since 2011 she has been employed as a research assistant at the Institute of Physics in Zagreb, Croatia.

List of publications:

1. I. Kavre Piltaver, R. Peter, I. Šarić, K. Salamon, I. Jelovica Badovinac, K. Koshmak, S. Nannarone, I. Delač Marion, and M. Petravić, "Controlling the grain size of polycrystalline TiO_2 films grown by atomic layer deposition," *Applied Surface Science* **419**, 564 – 572 (2017).

2. T. Car, N. Nekić, M. Jerčinović, K Salamon, I. Bogdanović-Radović, I. Delač Marion, J. Dasović, G. Dražić, M. Ivanda, S. Bernstorff, B. Pivac, M. Kralj, N. Radić, and M. Buljan, "Closely packed Ge quantum dots in ITO matrix: influence of Ge crystallization on optical and electrical properties," *Materials Research Express* **3**, 065003 (2016).

3. I. Delač Marion, D. Grgičin, K. Salamon, S. Bernstorff, and T. Vuletić, "Polyelectrolyte Composite: Hyaluronic Acid Mixture with DNA," *Macromolecules* **48**, 2686–2696 (2015).

4. A. Selmani, M. Špadina, M. Plodinec, I. Delač Marion, M. C. Willinger, J. Lützenkirchen, H. D. Gafney, and E. Redel, "An Experimental and Theoretical Approach to Understanding the Surface Properties of One-Dimensional TiO_2 Nanomaterials," *The Journal of Physical Chemistry C* **119**, 19729–19742 (2015).

5. M. Buljan, S. Facsko, I. Delač Marion, V. Mikšić Trontl, M. Kralj, M. Jerčinović, C. Baehtz, A. Muecklich, V. Holỳ, N. Radić, and J. Grenzer,

"Self-assembly of Ge quantum dots on periodically corrugated Si surfaces," *Applied Physics Letters* **107**, 203101 (2015).

6. M. Jerčinović, N. Radić, M. Buljan, J. Grenzer, I. Delač Marion, M. Kralj, I. Bogdanović-Radović, R. Hübner, P. Dubček, K. Salamon, and S. Bernstorff, "Self-assembled growth of Ni nanoparticles in amorphous alumina matrix," *Journal of nanoparticle research* **16**, 2296 (2014).

7. M. Buljan, M. Jerčinović, Z. Siketić, I. Bogdanović-Radović, I. Delač Marion, M. Kralj, M. Ivanda, A. Turković, G. Dražić, S. Bernstorff, and N. Radić, "Tuning the growth properties of Ge quantum dot lattices in amorphous oxides by matrix type," *Journal of Applied Crystallography* **46**, 1490–1500 (2013).